University of California
Santa Barbara

Robotic RF Sensing with Off-the-Shelf Devices

A dissertation submitted in partial satisfaction
of the requirements for the degree

Doctor of Philosophy
in
Electrical and Computer Engineering

by

Chitra Karanam Ravindranath

Committee in charge:

Professor Yasamin Mostofi, Chair
Professor Jerry Gibson
Professor Upamanyu Madhow
Professor Pradeep Sen

December 2020

The Dissertation of Chitra Karanam Ravindranath is approved.

Professor Jerry Gibson

Professor Upamanyu Madhow

Professor Pradeep Sen

Professor Yasamin Mostofi, Committee Chair

December 2020

Robotic RF Sensing with Off-the-Shelf Devices

by

Chitra Karanam Ravindranath

To Mom and Dad

Acknowledgements

First and foremost, I would like to express my sincere gratitude to my advisor Professor Yasamin Mostofi, whose guidance has been invaluable throughout my research and my time in the lab. I am grateful for the opportunity to have worked in the lab on exciting and interesting topics. Her continued support over the last six years has helped me immensely in all aspects of my research life.

I would also like to thank Professor Jerry Gibson, Professor Upamanyu Madhow, and Professor Pradeep Sen for being a part of my committee and giving me valuable feedback on my research. I would like to acknowledge various faculty members from the Electrical Engineering department at UCSB for offering interesting courses that I was glad to attend.

I would like to thank all our lab members, past and present, for all their help over the years. Specifically, I would like to thank Belal, Herbert, Saandeep, Arjun, and Anurag for their help with experiments, discussions and for making the lab a fun and exciting environment. I would also like to thank my friends outside the lab - Apoorva, Ekta, Srinidhi, Badki, Kartik, Mrinal, Anant, Soorya, Archith, Puneeth, and Bharat for making this journey at UCSB memorable.

Finally, I would like to thank my parents, whose continued support has helped me grow over the years. Last but not least, I would like to thank Nihar for being a pillar of strength and helping me finish this journey.

Curriculum Vitæ

Chitra Karanam Ravindranath

Education

2020	Ph.D. in Electrical and Computer Engineering (Expected), University of California, Santa Barbara.
2016	M.S. in Electrical and Computer Engineering, University of California, Santa Barbara.
2014	Dual Degree B.Tech in Electrical Engineering with M.Tech in Communication Systems, Indian Institute of Technology Madras.

Publications

- H. Cai*, B. Korany*, **C. R. Karanam***, and Y. Mostofi, "Teaching RF to Sense without RF Training Measurements," to appear, in proceedings of the *ACM on Interactive, Mobile, Wearable and Ubiquitous Technologies (IMWUT)*, Dec. 2020.
- B. Korany*, **C. R. Karanam***, H. Cai*, and Y. Mostofi, "XModal-ID: Using WiFi for Through-Wall Person Identification from Candidate Video Footage," in proceedings of the*25th Annual International Conference on Mobile Computing and Networking (MobiCom)*, Oct. 2019.
- **C. R. Karanam**, B. Korany, and Y. Mostofi, "Tracking from One Side – Multi-Person Passive Tracking with WiFi Magnitude Measurements," in proceedings of the*18th ACM/IEEE International Conference on Information Processing in Sensor Networks (IPSN)*, April 2019.
- B. Korany*, **C. R. Karanam***, and Y. Mostofi, "Adaptive Near-Field Imaging with Robotic Arrays,"*10th IEEE Sensor Array and Multichannel Signal Processing Workshop*, July 2018.
- **C. R. Karanam***, B. Korany*, and Y. Mostofi, "Magnitude-Based Angle-of-Arrival Estimation, Localization, and Target Tracking," in proceedings of the*17th ACM/IEEE International Conference on Information Processing in Sensor Networks (IPSN),* April 2018.
- S. Depatla, **C. R. Karanam**, and Y. Mostofi, "Robotic Through-Wall Imaging: Radio-Frequency Imaging Possibilities with Unmanned Vehicles," *IEEE Antennas and Propagation Magazine, Special Issue on Electromagnetic Inverse Problems for Sensing and Imaging,* Oct. 2017.
- **C. R. Karanam** and Y. Mostofi, "3D Through-Wall Imaging with Unmanned Aerial Vehicles Using WiFi," in proceedings of the*16th ACM/IEEE International Conference on Information Processing in Sensor Networks (IPSN),* April 2017.

** equal contribution*

Abstract

Robotic RF Sensing with Off-the-Shelf Devices

by

Chitra Karanam Ravindranath

Radio Frequency (RF) signals, like WiFi, are ubiquitous in our surroundings. These signals interact with the objects as well as people, on their path from the transmitter to the receiver, and can thus carry implicit information about the area that they pass through. Sensing and extracting such information from off-the-shelf devices in our surroundings, is a problem of considerable interest. Additionally, robots are becoming an integral part of our lives. Utilizing the mobility of robots, along with the ubiquity of off-the-shelf devices, opens up new possibilities for RF sensing with robots. In this dissertation, we show how we can use readily available off-the-shelf devices to deduce information about our surroundings, and discuss various possibilities for utilizing the mobility of robots for RF sensing.

First, we discuss how we can use WiFi RSSI measurements and drones to achieve 3D through-wall imaging of completely unknown areas behind brick walls. This is possible through our proposed approach involving signal propagation modeling, sparsity and spatial correlation exploitation, and path planning optimization. We then validate our proposed approach through experimental results obtained using our extensive testbed that includes drones and off-the-shelf WiFi devices.

In the second part, we propose a new approach to the traditional angle-of-arrival (AoA) estimation problem, which enables AoA estimation with only the signal magnitude at an antenna array, and without the need for signal phase measurements. We estimate the AoA of various signal paths by utilizing the spatial correlation of the signal

magnitude. We then discuss the fundamental ambiguities that can arise in such a framework and propose methods to address them. We finally show how this new framework allows for predicting the ray makeup, and the resulting channel quality, at unvisited locations in the workspace.

Finally, we discuss our proposed approach for multi-target tracking using WiFi. We have enabled passive tracking of multiple people walking in an area, with a small number of transceivers located on one side of the area, and without the need for people to carry any device. Our approach builds on the magnitude-based AoA framework, and utilizes multi-dimensional parameter extraction and particle filtering in order to track multiple targets. We then discuss our extensive experimental results for passively tracking up to three simultaneously walking people, using a small number of WiFi transceivers on one side of the area.

Contents

List of Figures

List of Tables

Chapter 1

Introduction

Radio Frequency (RF) signals are ubiquitous in our everyday lives. Most of our devices have the capability of transmitting and receiving such signals. As these signals go through and interact with objects/people in the environment, the surroundings leave their signature on the transmitted signals. Thus, in addition to transmitting information from one device to another, these signals can also be used to sense and deduce information about our physical surroundings. Furthermore, signals like WiFi can easily pass through walls, facilitating sensing through obstacles as well. As such, RF sensing has become a topic of interest to the research community in recent years. In RF sensing, it is of interest to sense and learn about the environment with everyday communication signals.

RF sensing with WiFi signals is the main topic of this thesis. In particular, since WiFi signals are ubiquitous, it is of interest to sense and learn about the environment using WiFi transceivers of off-the-shelf devices, such as laptops, routers, and mobile phones. This dissertation focuses on RF sensing with signal power measurements, which can easily and reliably be measured on off-the-shelf devices and WiFi cards.

Robots are predicted to become an integral part of our society in the near future. We currently use them for a variety of tasks including home cleaning, construction, warehouse

packing, and goods delivery. Using robots to aid our RF sensing tasks then opens up new sensing paradigms. For instance, we can utilize the mobility of the robots to optimally sense our surroundings and extract the necessary information from the RF signals. More specifically, using robots allows for autonomous and optimized antenna positioning in the area of interest. Thus, robotic RF sensing is a particularly interesting and valuable conjunction that we explore in this dissertation.

There are a variety of RF sensing applications that have been of interest to the research community in the recent years, including through-wall imaging, localization, tracking, occupancy estimation, person identification, and gesture recognition. In this dissertation, we investigate a few of these applications, delving specifically into through-wall imaging, angle-of-arrival estimation, and multi-target passive tracking. The main thrust of this dissertation is then to achieve solutions to these problems using only information that is easily extractable from off-the-shelf wireless devices, and without the need for extensive resources like ultra wideband signals and synchronized phase measurements across antennas.

More specifically, in this dissertation, we focus on three aspects of RF sensing, as described below:

- **3D Through-Wall Imaging**: We equip two drones with WiFi transceivers in order to move around outside a completely unknown area and image the area in 3D, through walls, using only on-board WiFi RSSI measurements. Our proposed approach is a novel combination of wave modeling, spatial correlation exploitation, and path planning. We extensively test our proposed approach with our experimental test-bed.

- **Magnitude-Based Angle-of-Arrival Estimation and Channel Prediction**: We show that it is possible to estimate the angles-of-arrival at an antenna array

using only the magnitude of the signals received at the array, without the need for signal phase information. We extensively discuss the ambiguities that can arise in such a framework and show ways to resolve them. We then show the implication of this framework in the context of robotic channel prediction, with only signal magnitude. More specifically, we show how we can predict the fundamental makeup of the rays and subsequently predict the channel at unvisited locations in the space.

- **Multi-Person Passive Tracking**: We show how to extend the previous magnitude-based framework to the dual problem of using stationary transceivers to track moving targets. We experimentally validate our proposed approach using WiFi devices located on one side of the area, and track up to 3 moving people passively, without the need for them to carry any device.

We next introduce the aforementioned topics in more detail, place them in the context of the state-of-the-art by reviewing the literature in the respective domains, and summarize our contributions in each of these areas.

1.1 3D Through-Wall Imaging

Consider a completely unknown area that is occluded from view by a wall or other obstacles. RF signals such as WiFi can pass through walls and carry relevant information about the objects on the other side of the wall. This naturally brings up the following question,"Can WiFi signals image details of stationary objects through walls?" Through-wall imaging is of particular interest due to its benefits for scenarios like disaster management, surveillance, and search and rescue, where assessing the situation prior to entering an area can be very crucial. However, the general problem of through-wall imaging using RF signals is a very challenging problem, and has hence been a topic of

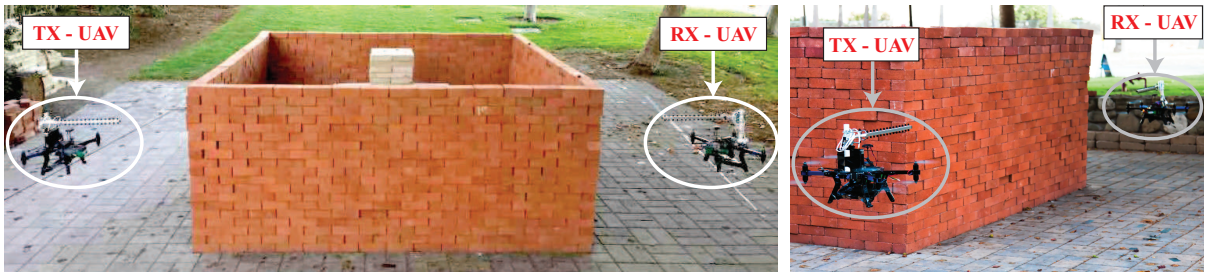

Figure 1.1: Two examples of our considered scenario where two UAVs fly outside an unknown area to collect WiFi RSSI measurements for the purpose of 3D through-wall imaging.

research in a number of communities such as electromagnetics, signal processing, and networking [2, 3, 4, 5, 1].

In Chapter 2, we are interested in the 3D through-wall imaging of a completely unknown area using Unmanned Aerial Vehicles (UAVs) and WiFi RSSI measurements. More specifically, we consider the scenario where two UAVs move outside of an unknown area, and collect wireless received power measurements to reconstruct a 3D image of the unknown area, an example of which is shown in Fig. 1.1. We then show how to solve this problem using a novel combination of Markov random field (MRF) modeling, loopy belief propagation, sparse signal processing, and proper 3D robotic path planning. We further develop an extensive experimental testbed and validate the proposed framework.

1.1.1 Related Work

In the electromagnetics literature, inverse scattering problems have long been explored in the context of imaging [6, 7, 8]. Ultra wideband signals have also been heavily utilized for the purpose of through-wall imaging [9, 10, 2, 11]. Phase information has also been used for beam forming, time-reversal based imaging, or in the context of synthetic aperture radar [12, 2, 13]. However, most past work rely on utilizing a large bandwidth, phase information, or motion of the target for imaging. Validation in a simulation envi-

ronment is also common due to the difficulty of hardware setup for through-wall imaging. In [5, 1, 3, 14, 15], the authors use WiFi RSSI measurements to image through walls in 2D. They show that by utilizing unmanned ground vehicles and proper path planning, 2D imaging with only WiFi RSSI is possible. This has created new possibilities for utilizing unmanned vehicles for RF sensing, which allows for optimizing the location of the transmitter/receiver antennas in an autonomous way. However, 3D through-wall imaging with only WiFi RSSI measurements, which becomes considerably more challenging than the corresponding 2D problem, has not been explored, which is the main motivation for this chapter. It is noteworthy that directly applying the aforementioned 2D imaging framework to the 3D case can result in a poor performance (as we see later in the chapter), mainly because the 3D problem is considerably more under-determined. This necessitates a novel and holistic 3D imaging framework that addresses the new challenges, as we propose in this chapter.

1.1.2 Contributions

The main contributions of this chapter are as follows:

1. We show how to design efficient robotic paths in 3D for our through-wall imaging problem. In effect, our paths aim at capturing the most spatial changes of the area while considering quality and time constraints of operation.

2. We propose a new framework for 3D through-wall imaging of unknown areas based on MRF modeling and loopy belief propagation. In the vision literature, MRF modeling has been utilized in order to incorporate the spatial dependencies among the pixels of an image [16, 17]. Furthermore, various methods based on loopy belief propagation [18, 17], iterative conditional modes [16], and graph cuts [19] have been proposed for image denoising, segmentation, and texture labeling. In this chapter,

we borrow from such literature to solve our 3D through-wall imaging problem, based on sparse signal processing, MRF modeling and loopy belief propagation.

3. We design and implement a complete experimental testbed that enables two octocopters to properly localize, navigate, and collect wireless measurements. We then present 3D through-wall imaging of unknown areas using our testbed. Our results confirm that high-quality through-wall imaging of challenging areas, such as behind thick brick walls, is possible with only WiFi RSSI measurements and UAVs. To the best of our knowledge, our 3D imaging results showcase high-quality imaging of more complex areas than what has been reported in the literature with even phase and/or UWB signals.

1.2 Magnitude-Based Angle-of-Arrival Estimation

In addition to imaging, there has been an increasing interest in using RF signals for localization and tracking. These are crucial techniques that can be useful in many scenarios such as emergency response, radio navigation, security, surveillance, and smart homes. Angle of Arrival (AoA) estimation, on the other hand, is an important problem that can be used towards localization and tracking. However, most AoA estimation approaches require synchronized signal phase information, which can not be obtained on all off-the-shelf devices, or on a synthesized array using robots.

In Chapter 3, we show how to estimate the AoA of the signal paths arriving at a receiver array, using only the received signal magnitude measurements (or, equivalently, the received power measurements). We discuss the loss in information arising due to using only signal magnitude, instead of the classical phase-based approaches, and how this leads to ambiguity in AoA estimation. We then show how we can overcome these ambiguities and uniquely estimate AoA using only WiFi received signal magnitude. We

then show how to use this magnitude-based AoA estimation framework to predict the ray makeup at unvisited locations in the workspace and subsequently predict the channel quality and channel variations.

1.2.1 Related Work

AoA estimation is a classical problem that has gained considerable attention in the field of array signal processing. Many solutions have been proposed in the literature, including traditional beamforming [20], MUSIC [21], and ESPRIT [22]. All of these techniques assume that the received signal phase measurements are available and synchronized across the elements of a measurement array. However, many of the commercial off-the-shelf (COTS) wireless devices do not provide stable absolute phase measurements [23], making the synthesis of a long array not possible due to synchronization issues. There have been attempts to stabilize the phase measurements in COTS devices (e.g., Intel 5300 WLAN card), but these approaches do not result in synchronized phase measurements required for array signal processing [23]. Few works have investigated the problem of AoA estimation using only the signal power (or equivalently, magnitude) measurements at the array elements. For instance, in [24], mechanical steering of a directional antenna is utilized, whereas in [25], special type of antennas that have multiple radiation patterns are used. Such work, however, require custom-made hardware. As for array processing techniques using magnitude-only measurements, [26] proposes a sparsity-based optimization problem which assumes the knowledge of the number of sources, and [27] proposes an algorithm that can only find a function of the AoAs, but not the AoAs themselves. Furthermore, the aforementioned papers are only validated in a simulation environment, and with only active transmitters. In this chapter, we propose and experimentally validate a framework for estimating the AoAs of active transmitters

as well as passive objects, using only the received signal magnitude.

Channel prediction is also a well known problem and a variety of solutions have been proposed for prediction, including ray tracing and probabilistic channel prediction [28, 29]. More recently, there have been ray-tracing based approaches proposed for using RF signals and robots to estimate the reflectivity of objects and thereby predict the channel at unvisited locations [30, 31]. These approaches, however, need precise location and shape of the objects in the area, they assume that each object in the workspace reflects uniformly in all the directions, and further use mmwave signals which reduces the number of effective reflections. Such assumptions hinder the prediction of small scale variations in general scenarios. For instance, each object does not necessarily reflect with the same coefficient in all the directions, especially in near-field cases, due to the varying radar cross sections of the object in different directions [32]. Also, precise information of objects in the area may not be available. Finally, they fail in cases where there are non-homogeneous objects, or when the rays in the area undergo other propagation phenomena like diffraction or propagation through objects. Hence, in this chapter, we propose a new framework that estimates the fundamental parameters of the rays and predicts the channel at unvisited locations.

1.2.2 Contributions

The main contributions of this chapter are as follows:

- We propose a new approach to estimate the AoA of signal paths arriving at a receiver array using only the magnitude of the corresponding received signal measurements. Our approach shows that the auto-correlation function (and therefore the power spectrum) of the received signal magnitude at the receiver array carries vital information on the AoA, an analysis which will then be the foundation for our proposed method-

ologies throughout the chapter. For instance, we propose a framework for the case of angular localization of static objects/humans, based on this foundation.

- We then extend this framework to estimate and predict the fundamental makeup of the rays at unvisited locations in an area, in order to predict the overall channel strength and channel variations at any unvisited location in the workspace.

- We validate our magnitude-based AoA estimation framework with extensive experiments in various areas and show that our approach can achieve high-quality angular localization. More specifically, we utilize a robot to emulate an antenna array and estimate the AoA of active and passive objects, using only WiFi magnitude measurements. Our angular localization has an overall Mean Absolute Error (MAE) of 2.56°, and only takes an average of 0.45 seconds to localize up to three objects. Overall, our results show that AoA can be estimated, with a high accuracy, and with only the received signal magnitude measurements. We then experimentally validate our channel prediction framework and show its performance.

1.3 Multi-Person Passive Tracking

In the previous section, we introduced the idea of using signal magnitude to achieve AoA estimation at an antenna array. As mentioned, AoA can be further used to achieve localization and target tracking. In particular, passively tracking multiple people that are walking in an area, without relying on them to carry any device, is a challenging problem of considerable interest, due to its importance in many applications such as elderly monitoring, intrusion detection, and retail analytics.

In Chapter 4, we consider the problem of passively tracking multiple people walking in an area, using minimal WiFi resources on only one side. In particular, we are interested

in multi-person tracking using only the magnitude of WiFi Channel State Information (CSI) measurements, measured using one WiFi transmitter and a small number of WiFi receiver Network Interface Cards (NICs) located on only one side of the area. We next review the state-of-the-art in multi-person tracking.

1.3.1 Related Work

Device-free localization and tracking (DFLT) is a challenging problem that has gained a considerable attention in the recent years. The efforts exerted in DFLT can be broadly categorized into two categories: (a) machine learning and fingerprinting-based approaches, and (b) model-based approaches. Machine learning and fingerprinting approaches (e.g. [33, 34, 35]) require extensive prior calibration and training, which is both time consuming and environment-specific. Model-based approaches, on the other hand, build a model/relationship between the location (or track) of the target and the wireless measurements at the receiver. They then estimate the location and track of the target based on that model. Earlier work in this category assumes the availability of extensive amount of resources. For instance, [36] tracks multiple targets using a link-crossing model based on RSSI, but with a large number of wireless sensors (total of 32) distributed on all sides of the tracking area. Other attempts track multiple targets using specialized hardware and signals with very large bandwidth [37, 38].

More recently, WiFi CSI has been made available on Commercial Off-The-Shelf (COTS) WiFi devices, such as Intel 5300 and Atheros AR9580 WiFi cards. The availability of CSI on COTS WiFi cards has opened the door for DFLT techniques that require fewer resources than before. Several works then utilized WiFi CSI to track a *single* moving target by estimating different parameters of the wireless signal, e.g. Angle-of-Arrival (AoA), Time of Flight (ToF), and Doppler spread [39, 40]. Two common threads exist

among the aforementioned CSI-based device-free tracking approaches. First, all these approaches are designed for single target tracking, and fail to track multiple targets that are moving simultaneously. Second, these approaches rely on the CSI phase information, which can be hard to measure accurately or may be unavailable on other COTS devices. Furthermore, relying on the phase information limits the flexibility of adding more antennas to the receiver, since different WiFi cards need to be synchronized for obtaining meaningful phase information. This will add a considerable synchronization overhead to the system. These two problems motivate the need for a device-free tracking framework, that is able to track *multiple* targets, using only the WiFi *magnitude* measurements.

Our proposed framework in this chapter is then the first to enable multiple target tracking with comparable accuracy to the state-of-the-art, without requiring extra resources. We show that multiple target tracking is possible using only magnitude measurements on one receiver array located on the same side of the tracking area as the transmitter. We provide tracking results of up to 3 people, with a mean absolute error of 47 cm across 40 experiments in six different tracking areas.

1.3.2 Contributions

In this chapter, we propose a framework for passively tracking *multiple* people walking in an area, without requiring a prohibitive amount of resources (e.g. bandwidth or number of transceivers), which were used previously for such purposes. Our framework uses only the magnitude of WiFi CSI measurements, measured from one side of the area, on a small receiver array. More specifically,

- We propose a new magnitude-based framework to track multiple people walking in an area, using one transmitter and a very small receiver array (for instance, from a couple of laptops), without the need to make any prior measurements in the area of

interest. By modeling the tracking problem in terms of only the signal magnitude, our proposed framework can be implemented on any off-the-shelf platform where phase measurements are not reliable or are not easily available. Furthermore, additional Rx NICs can be added to the receiver setup if required, without any need for phase synchronization or calibration. On the other hand, such a receiver antenna extension in the case of relying on phase measurements would have required an antenna port on each NIC to be used up for the purpose of synchronization, after which the phase is still only accurate to within a median error of 20° [41]. Our proposed framework does not lose any antenna ports in the process of combining multiple NICs, and is not sensitive to phase errors that can affect the receptions on off-the-shelf devices.

- We propose a two-dimensional signal model for the estimation of various AoA parameters that are functions of the targets' locations and motion directions. By posing our problem as a joint parameter estimation problem in this manner, we show how the ambiguity in individual dimensions can be overcome. We then extend the multi-dimensional MUSIC algorithm to our magnitude-based modeling framework in order to estimate the 2D AoA parameters. Finally, we track multiple targets in the area by using a Particle Filter (PF) with a Joint Probabilistic Data Association Filter (JPDAF).

- We extensively validate our proposed multi-person tracking framework through a total of 40 experiments in 6 different environments, with 1, 2, and 3 people walking on different paths, on different days. We use only one transmit and 3 WiFi receiver NICs on one side of the area to measure WiFi CSI magnitude. Our results show highly accurate tracking with a mean error of 38 cm in outdoor areas/parking lots, and 55 cm in indoor areas.

Chapter 2

3D Through-Wall Imaging With UAVs Using WiFi

In this chapter, we are interested in the 3D through-wall imaging of completely unknown areas, using Unmanned Aerial Vehicles (UAVs) and WiFi RSSI. Imaging stationary objects in 3D using only WiFi is a challenging problem due to several propagation phenomena as well as the vast number of unknowns and limited number of measurements that can feasibly be obtained. Thus, in this chapter, we show how to properly design 3D robotic paths that can be utilized for efficient and autonomous antenna positioning for the imaging through wall problem. We further propose an approach that properly models the signal propagation through objects and solves for the 3D image of the area using Markov random field modeling, spatial correlation exploitation, and sparse signal processing. Finally, we describe our extensive experimental testbed that enables us to successfully validate our approach in real areas.

The rest of this chapter is organized as follows. In Section 2.1, we formulate our 3D through-wall imaging problem and summarize the measurement model. In Section 2.2, we show how to solve the 3D imaging problem using Markov random field modeling,

loopy belief propagation, and sparse signal processing. We then discuss how to design efficient 3D UAV paths in Section 2.3. Finally, we present our experimental testbed in Section 2.4 and our experimental results for 3D through-wall imaging of unknown areas in Section 2.5.

2.1 Problem Formulation

Consider a completely unknown area $\mathcal{D} \subset \mathbb{R}^3$, which may contain several occluded objects that are not directly visible, due to the presence of walls and other objects in $\mathcal{D}$.[1] We are interested in imaging $\mathcal{D}$ using two Unmanned Aerial Vehicles (UAVs) and only WiFi RSSI measurements. Fig. 1.1 shows two example scenarios, where two UAVs fly outside of the area of interest, with one transmitting a WiFi signal (TX UAV) and the other one receiving it (RX UAV). In this example, the domain $\mathcal{D}$ would correspond to the walls as well as the region behind the walls.

When the TX UAV transmits a WiFi signal, the objects in $\mathcal{D}$ affect the transmission, leaving their signatures on the collected measurements. Therefore, we first model the impact of objects on the wireless transmissions in this section, and then show how to do 3D imaging and design UAV paths in the subsequent sections. Consider a wireless transmission from the transmitting UAV to the receiving one. Since our goal is to perform 3D imaging based on only RSSI measurements, we are interested in modeling the power of the received signal as a function of the objects in the area. To fully model the receptions, one needs to write the volume-integral wave equations [42], which will result in a non-linear set of equations with a prohibitive computational complexity for our 3D imaging problem. Alternatively, there are simpler linear approximations that model the interaction of the transmitted wave with the area of interest. Wentzel-Kramers-Brillouin

[1] In this chapter, we will interchangeably use the terms "domain", "area" and "region" to refer to the 3D region that is being imaged.

(WKB) and Rytov are two examples of such linear approximations [42]. WKB approximation, for instance, only considers the impact of the objects along the line connecting the transmitter (TX) and the receiver (RX). This model is a very good approximation at very high frequencies, such as x-ray, since a wave then primarily propagates along a straight line path, with negligible reflections or diffractions [42]. Rytov approximation, on the other hand, considers the impact of some of the objects that are not along the direct path that connects the TX and RX, at the cost of an increase in computational complexity, and is a good approximation under certain conditions [42].

In this chapter, we use a WKB-based approximation to model the interaction of the transmitted wave with the area of interest. While this model is more valid at very high frequencies, several work in the literature have shown its effectiveness when sensing with signals that operate at much lower frequencies such as WiFi [3, 4]. WKB approximation can be interpreted in the context of the shadowing component of the wireless channel, as we shall summarize next.

Consider the received power for the i^{th} signal transmitted from the TX UAV to the RX one. We can express the received power as follows [43, 44]:

$$P_{\text{R}}(\mathbf{p}_i, \mathbf{q}_i) = \; P_{\text{PL}}(\mathbf{p}_i, \mathbf{q}_i) + \gamma \sum_j d_{ij}\eta_{ij} + \zeta(\mathbf{p}_i, \mathbf{q}_i), \tag{2.1}$$

where $P_{\text{R}}(\mathbf{p}_i, \mathbf{q}_i)$ denotes the received signal power (in dB) for the i^{th} measurement, when the TX and RX are located at $\mathbf{p}_i \in \mathbb{R}^3$ and $\mathbf{q}_i \in \mathbb{R}^3$ respectively. Furthermore, $P_{\text{PL}}(\mathbf{p}_i, \mathbf{q}_i) = 10 \log_{10} \frac{\beta P_{\text{T}}}{(\|\mathbf{p}_i - \mathbf{q}_i\|_2)^\alpha}$ is the path loss power (in dB), where P_{T} is the transmit power, β is a constant that depends on the system parameters and α is the path loss exponent.[2] The term $\gamma \sum_j d_{ij}\eta_{ij}$ is the shadowing (shadow fading) term in the dB domain,

[2]In practice, the two parameters of the path loss component can be estimated by using a few line-of-sight transmissions between the two UAVs, near the area of interest when there are no objects in between them.

which captures the impact of the attenuations of the objects on the line connecting the TX and RX UAVs. More specifically, d_{ij} is the distance traveled by the signal within the j^{th} object along the line connecting the TX and the RX for the i^{th} measurement, η_{ij} is the decay rate of the signal in the j^{th} object along this line, and $\gamma = 10 \log_{10} e$ is a constant. Finally, $\zeta(\mathbf{p}_i, \mathbf{q}_i)$ represents the modeling error in this formulation, which includes the impact of multipath fading and scattering off of objects not directly along the line connecting the TX and RX, as well as other un-modeled propagation phenomena and noise. In summary, Eq. 2.1, which we shall refer to as LOS-based modeling, additively adds the attenuations caused by the objects on the direct line connecting the TX and the RX.

The shadowing term can then be re-written as

$$\sum_j d_{ij}\eta_{ij} = \int\limits_{\mathbb{L}_{\mathbf{p}_i \to \mathbf{q}_i}} \eta(\mathbf{r}')\, \mathrm{d}\mathbf{r}', \tag{2.2}$$

where $\int_{\mathbb{L}_{\mathbf{p}_i \to \mathbf{q}_i}}$ denotes the line integral along the line connecting the TX and the RX, and $\eta(\mathbf{r})$ denotes the decay rate of the wireless signal at $\mathbf{r} \in \mathcal{D}$. Furthermore, $\eta(\mathbf{r}) < 0$ when there is an object at position $\mathbf{r}$ and $\eta(\mathbf{r}) = 0$ otherwise. η then implicitly carries information about the area we are interested in imaging.

In order to solve for η, we discretize $\mathcal{D}$ into N cubic cells of equal volume. Each cell is denoted by its center $\mathbf{r}_n$, where $n \in \{1, \ldots, N\}$. By discretizing Eq. 2.2, we have,

$$\int\limits_{\mathbb{L}_{\mathbf{p}_i \to \mathbf{q}_i}} \eta(\mathbf{r}')\, \mathrm{d}\mathbf{r}' \approxeq \sum_{j \in \mathcal{L}(\mathbf{p}_i, \mathbf{q}_i)} \eta(\mathbf{r}_j) \Delta d, \tag{2.3}$$

where $\mathcal{L}(\mathbf{p}_i, \mathbf{q}_i)$ denotes the set of cells along the line connecting the TX and the RX for the i^{th} measurement, and Δd is the dimension of a side of the cubic cell. Therefore, we

can approximate Eq. 2.1 as

$$P_i = \frac{P_{\mathrm{R}}(\mathbf{p}_i, \mathbf{q}_i) - P_{\mathrm{PL}}(\mathbf{p}_i, \mathbf{q}_i)}{\gamma \Delta d} \approxeq \sum_{j \in \mathcal{L}(\mathbf{p}_i, \mathbf{q}_i)} \eta(\mathbf{r}_j), \tag{2.4}$$

with P_i denoting the normalized received power of the i^{th} measurement. By stacking the measurements P_i as a column vector, we have,

$$\mathbf{P} \approxeq \mathbf{A}\mathbf{O}, \tag{2.5}$$

where $\mathbf{P} = [P_1, P_2, \ldots, P_M]^T$ and M is the number of measurements. $\mathbf{A}$ is a matrix of size $M \times N$ such that its entry $A_{i,j} = 1$ if the j^{th} cell is along the line connecting the TX and the RX for the i^{th} measurement, and $A_{i,j} = 0$ otherwise. Furthermore, $\mathbf{O} = [\eta(\mathbf{r}_1), \eta(\mathbf{r}_2), \ldots, \eta(\mathbf{r}_N)]^T$ represents the property of objects in the area of interest $\mathcal{D}$, which we shall refer to as the object map.

So far, we have described the system model that relates the wireless measurements to the object map, which contains the material properties of the objects in the area of interest. In this chapter, we are interested in imaging the geometry and locations of all the objects in $\mathcal{D}$, as opposed to characterizing their material properties. More specifically, we are interested in obtaining a binary object map $\mathbf{O}_b$ of the domain $\mathcal{D}$, where $\mathbf{O}_b$ is a vector whose i^{th} element is defined as follows:

$$O_{b_i} = \begin{cases} 1 & \text{if the } i^{\text{th}} \text{ cell contains an object} \\ 0 & \text{otherwise} \end{cases}. \tag{2.6}$$

In the next sections, we propose to estimate $\mathbf{O}_b$ by first solving for $\mathbf{O}$ and then making a decision about the presence or absence of an object at each cell, based on the estimated $\mathbf{O}$, using loopy belief propagation.

2.2 Solving the 3D Imaging Problem

In the previous section, we formulated the problem of reconstructing the object map as a system of linear equations, with the final goal of imaging a binary object map of the domain $\mathcal{D}$. In this section, we propose a two-step approach for 3D imaging of $\mathbf{O}_b$. In the first part, we utilize techniques from the sparse signal processing and regularization literature to solve Eq. 2.5, and thereby estimate $\mathbf{O}$. In the second part, we use loopy belief propagation in order to image a binary object map $\mathbf{O}_b$ based on the estimated $\mathbf{O}$. We note that in some of the past literature on 2D imaging [45, 3], either the estimated object map is directly thresholded to form a binary image, or the grayscale image is considered as the final image. Since 3D imaging with only WiFi signals becomes a considerably more challenging problem, such approaches do not suffice anymore. Instead, we propose to use loopy belief propagation in order to obtain the final 3D image, as we shall see later in this chapter.

2.2.1 Sparse Signal Processing

In this part, we aim to solve for $\mathbf{O}$ in Eq. 2.5. In typical practical cases, however, $N \gg M$, i.e., the number of wireless measurements is typically much smaller than the number of unknowns, which results in a severely under-determined underlying system. Then, if no additional condition is imposed, there will be a considerable ambiguity in the solution. We thus utilize the fact that several common spaces are sparse in their spatial variations, which allows us to borrow from the literature on sparse signal processing. Sparse signal processing techniques aim at solving an under-determined system of equations when there is an inherent sparsity in the signal of interest, and under certain conditions on how the signal is sampled [46, 47]. They have been heavily utilized in many different areas and have also proven useful in the area of sensing with radio frequency signals (e.g.,

2D imaging, tracking) [48, 49, 1]. Thus, we utilize tools from sparse signal processing to estimate $\mathbf{O}$, the map of the material properties. This estimated map will then be the base for our 3D imaging approach in the next section.

More specifically, we utilize the fact that most areas are sparse in their spatial variations and seek a solution that minimizes the Total Variation (TV) of the object map $\mathbf{O}$. We next briefly summarize our 3D TV minimization problem, following the notation in [50].

As previously defined, $\mathbf{O}$ is a vector representing the map of the objects in the domain $\mathcal{D}$. Let $\mathbf{I}$ be the 3D matrix that corresponds to $\mathbf{O}$. $\mathbf{I}$ is of dimensions $n_1 \times n_2 \times n_3$, where $N = n_1 \times n_2 \times n_3$. We seek to minimize the spatial variations of $\mathbf{I}$, i.e., for every element $I_{i,j,k}$ in $\mathbf{I}$, the variations across the three dimensions need to be minimized. Let $D_m \in \mathbb{R}^{3\times N}$ denote a matrix such that $D_m\mathbf{O}$ is a 3×1 vector of the spatial variations of the m^{th} element in $\mathbf{O}$, with m corresponding to the $(i, j, k)^{\text{th}}$ element in $\mathbf{I}$. The structure of D_m is such that $D_m\mathbf{O} = [I_{i+1,j,k} - I_{i,j,k}, I_{i,j+1,k} - I_{i,j,k}, I_{i,j,k+1} - I_{i,j,k},]^T$. Then, the TV function is given by

$$\text{TV}(\mathbf{O}) = \sum_{i=1}^{N} \|D_i\mathbf{O}\|_2, \tag{2.7}$$

where $\|.\|_2$ denotes the l_2 norm of the argument. We then have the following TV minimization problem:

$$\text{minimize } \text{TV}(\mathbf{O}), \text{ subject to } \mathbf{P} = \mathbf{AO}, \tag{2.8}$$

where $\mathbf{P}, \mathbf{A}$ and $\mathbf{O}$ are as defined in Eq. 2.5.

In order to solve the 3D TV minimization problem of Eq. 2.8, an efficient practical implementation using Nesterov's algorithm, TVReg has been proposed in [50]. TVReg is a MATLAB-based solver that efficiently computes the 3D TV minimization solution.

We use TVReg for solving the optimization problem of Eq. 2.8 in all the results of the chapter.

The solution obtained from solving Eq. 2.8 is an approximation to the object map $\mathbf{O}$. As previously mentioned in Section 2.1, the elements of $\mathbf{O}$ are all non-positive real numbers. We then flip the sign and normalize the values to the range $[0, 1]$, so that they represent the grayscale intensities at the corresponding cells, which we denote by $\mathbf{y}_s$. However, this solution is not a perfect representation of the object map, due to modeling errors and the under-determined nature of the linear system model, requiring further processing. Furthermore, we are only interested in estimating the presence or absence of an object at any location, as opposed to learning the material properties in this chapter. Therefore, we next describe our approach for estimating the binary object map $\mathbf{O}_b$ of the domain $\mathcal{D}$, given the observed intensities $\mathbf{y}_s$.

2.2.2 3D Imaging Using Loopy Belief Propagation

In this section, we consider the problem of estimating the 3D binary image of the unknown domain $\mathcal{D}$, based on the solution $\mathbf{y}_s$ of the previous section. As discussed earlier, $\mathbf{y}_s$ can be interpreted as the estimate of the gray-scale intensities at the cells in the 3D space. We are then interested in estimating the 3D binary image, which boils down to finding the best labels (occupied/not occupied) for each cell in the area of interest, while minimizing the impact of modeling errors/noise and preserving the inherent spatial continuity of the area.

To this end, we model the 3D binary image as a Markov Random Field (MRF) [51] in order to capture the spatial dependencies among local neighbors. Using the MRF model, we can then use the Hammersley-Clifford Theorem to express the probability distribution of the labels in terms of locally-defined dependencies. We then show how

to estimate the binary occupancy state of each cell in the 3D domain, by using loopy belief propagation [51] on the defined MRF. Utilizing loopy belief propagation provides a computationally-efficient way of solving the underlying optimization problem, as we shall see. We next describe the details of our approach.

Consider a random vector $\mathbf{X}$ that corresponds to the binary object map $\mathbf{O}_b$. Each element $X_i \in \{0, 1\}$ is a random variable that denotes the label of the i^{th} cell. Further, let $\mathbf{Y}$ denote a random vector representing the observed grayscale intensities. In general, there exists a spatial continuity among neighboring cells of an area. An MRF model accounts for such spatial contextual information, and is thus widely used in the image processing and vision literature for image denoising, image segmentation, and texture labeling [18, 16], as we discussed earlier. We next formally define an MRF.

Definition 1 *A random field* $\mathbf{U}$ *on a graph is defined as a Markov Random Field (MRF) if it satisfies the following condition:* $P(U_i = u_i | U_j = u_j, \forall j \neq i) = P(U_i = u_i | U_j = u_j, \forall j \in \mathcal{N}_i)$*, where* $\mathcal{N}_i$ *is the set of the neighboring nodes of* i*.*

In summary, every node is independent of the rest of the graph in an MRF, when conditioned on its neighbors. This is a good assumption for the 3D areas of interest to this dissertation. We thus next model our underlying system as an MRF. Consider the graph $\mathcal{G} = (\mathcal{V}, \mathcal{E})$ corresponding to a 3D discrete grid formed from the cells in the domain, where $\mathcal{V} = \{1, 2, \ldots, N\}$ is the set of nodes in the graph. Each node i is associated with a random variable X_i, that specifies the label assigned to that node. Furthermore, the edges of the graph $\mathcal{E}$ define the neighborhood structure of our MRF. In this work, we assume that each node in the interior of the graph is connected via an edge to its 6 nearest neighbors in the 3D graph, as is shown in Fig. 2.1. Additionally, since $\mathbf{X}$ is unobserved and needs to be estimated, all the nodes associated with $\mathbf{X}$ are referred to as hidden nodes [51]. Furthermore, Y_i is the observation of the hidden node i. These observations

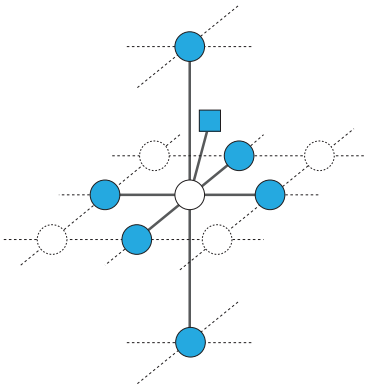

Figure 2.1: A depiction of the six-connected neighborhood structure of the underlying graph that corresponds to the Markov Random Field modeling of our 3D area of interest – Each node in the interior of the graph has six hidden nodes and one observed node as neighbors. The shaded circular nodes denote the neighbors that correspond to the hidden nodes, and the shaded square represents the observed node.

are typically modeled as being independent when conditioned on the hidden variables [51]. More specifically, the observations are assumed to satisfy the following property: $P(\mathbf{Y} = \mathbf{y}|\mathbf{X} = \mathbf{x}) = \prod_i P(Y_i = y_i|X_i = x_i)$. This is a widely-used assumption in the image processing and computer vision literature [51], where the observations correspond to the observed intensities at the pixels. We adopt this model for our scenario by adding a new set of nodes called the observed nodes to our graph $\mathcal{G}$. Each observed node Y_i is then connected by an edge to the hidden node X_i. Fig. 2.1 shows our described graph structure, where all the 6 hidden neighbors and an additional observed neighbor are shown for a node in the interior of the graph. For the nodes at the edge of the graph, the number of hidden node neighbors will be either 3, 4 or 5, depending on their position.

The advantage of modeling the 3D image as an MRF is that the joint probability distribution of the labels over the graph can be solely expressed in terms of the neighborhood cost functions. This result follows from the Hammersley-Clifford theorem [52], which we summarize next.

Theorem 1 *Suppose that* $\mathbf{U}$ *is a random field defined over a graph, with a joint probability distribution* $P(\mathbf{U} = \mathbf{u}) > 0$. *Then,* $\mathbf{U}$ *is a Markov Random Field if and only if*

its joint probability distribution is given by $P(\mathbf{U} = \mathbf{u}) = \frac{1}{Z}\exp(-E(\mathbf{u}))$*, where* $E(\mathbf{u}) = \sum_{c\in\mathcal{C}} H_c(u_c)$ *is the energy or cost associated with the label* $\mathbf{u}$ *and* $Z = \sum_{\mathbf{u}} \exp(-E(\mathbf{u}))$ *is a normalization constant. Further,* $\mathcal{C}$ *is the set of all the cliques in the graph,* $H_c(u_c)$ *is the cost associated with the clique* c*, and* u_c *is the realization (labels) associated with the nodes in* c*.*[3]

Proof: See [52] for details. ■

We next establish that our defined graph of hidden and observed nodes is an MRF and thus satisfies the joint distribution of Theorem 1. More specifically, based on our defined neighborhood system, every hidden node X_i in the interior of the graph has a neighborhood of six hidden nodes and one observed node. Furthermore, every observed node Y_i has one neighbor, the corresponding hidden node X_i, as we established. Let U_i denote any node in this graph, which can correspond to a hidden or an observed node. Such a node U_i is independent of the rest of the graph, when conditioned on its neighbors. Therefore, the overall graph consisting of hidden and observed nodes is an MRF. Then, by using the Hammersley-Clifford Theorem (Theorem 1), we get the following joint probability distribution for the nodes,

$$P(\mathbf{X} = \mathbf{x}, \mathbf{Y} = \mathbf{y}) = \frac{1}{Z}\exp(-E(\mathbf{x}, \mathbf{y})), \tag{2.9}$$

where $Z = \sum_{\mathbf{x},\mathbf{y}} \exp(-E(\mathbf{x}, \mathbf{y}))$ is a normalization constant, and $E(\mathbf{x}, \mathbf{y})$ is defined over the cliques of the graph. In our case, the graph has cliques of size 2. Furthermore, there are two kinds of cliques in the graph: cliques associated with two hidden nodes and cliques associated with one hidden and one observed node. Therefore, $E(\mathbf{x}, \mathbf{y})$ can be

[3] A clique in a graph is defined as a set of nodes that are completely connected.

expressed as follows:

$$E(\mathbf{x}, \mathbf{y}) = \sum_{i=1}^{N} H_i(x_i, y_i) + \sum_{(i,j)\in\mathcal{E}} H_{ij}(x_i, x_j). \tag{2.10}$$

In the above equation, $H_i(x_i, y_i)$ is the cost of associating a label x_i to a hidden node that has a corresponding observation y_i. Furthermore, $H_{ij}(x_i, x_j)$ is the cost of associating label (x_i, x_j) to a neighboring pair of hidden nodes (i, j).

Given a set of observations $\mathbf{y}_s$, we then consider finding the $\mathbf{x}$ (labels) that maximizes the posterior probability (MAP), i.e., $P(\mathbf{X} = \mathbf{x}|\mathbf{Y} = \mathbf{y}_s)$. From Eq. 2.9, we have,

$$P(\mathbf{X} = \mathbf{x}|\mathbf{Y} = \mathbf{y}_s) = \frac{1}{Z_y} \exp(-E(\mathbf{x}, \mathbf{y}_s)), \tag{2.11}$$

where $Z_y = \sum_{\mathbf{x}} \exp(-E(\mathbf{x}, \mathbf{y}_s))$ is a normalization constant. It then follows from Theorem 1 and Eq. 2.11 that $\mathbf{X}$ given $\mathbf{Y} = \mathbf{y}_s$ is also an MRF over the graph $\mathcal{G}$ of the hidden variables defined earlier.

However, directly solving for $\mathbf{x}$ that maximizes Eq. 2.11 is combinatorial and thus computationally prohibitive. Several distributed and iterative algorithms have thus been proposed in the literature to efficiently solve this classical problem of inference over a graph [53]. Belief propagation is one such algorithm, which has been extensively used in the vision and channel coding literature [51, 54]. In our work, we then utilize belief propagation to efficiently solve the problem of estimating the best labels over the graph, given the observations $\mathbf{y}_s$.

Utilizing Loopy Belief Propagation

Belief propagation based algorithms can find the optimum solution for graphs without loops, but provide an approximation for graphs with loops.[4] In our case, the graph representing our inference problem of interest has loops, which is a common trend for graphs representing vision and image processing applications. Even though belief propagation is an approximation for graphs with loops, it is shown to provide good results in the literature [54].

There are two versions of the belief propagation algorithm: the sum-product and the max-product. The sum-product computes the marginal distribution at each node, and estimates a label that maximizes the corresponding marginal. Thus, this approach finds the best possible label for each node individually. On the other hand, the max-product approach computes the labels that maximize the posterior probability (MAP) over the entire graph. Thus, if the graph has no loops, the max-product approach converges to the solution of Eq. 2.11, which is the optimum solution.

Loopy belief propagation refers to applying the belief propagation algorithms to the graphs with loops. In such cases, there is no guarantee of convergence to the optimum solution for the max-product or sum-product methods. However, several work in the literature have used these two methods with graphs with loops and have shown good results [18, 17, 56]. Here, we thus utilize the sum-product version, which has better convergence guarantees [54], to estimate the labels of the hidden nodes. We next describe the sum-product loopy belief propagation algorithm [57].

The sum-product loopy belief propagation is a message passing algorithm that computes the marginal of the nodes in a distributed manner. Let $m_{ij}^{(t)}(x_j)$ denote the message that node i passes to node j, where t denotes the iteration number. The update rule for

[4] In a graph with loops, solving for the optimal set of labels is an NP-hard problem [55].

the messages is given by

$$m_{ij}^{(t)}(x_j) = z_m \sum_{x_i} \Sigma_i(x_i, y_i)\Sigma_{ij}(x_i, x_j) \prod_{k \in \mathcal{N}_i \setminus j} m_{ki}^{(t-1)}(x_i), \tag{2.12}$$

where $\Sigma_i(x_i, y_i) = \exp(-H_i(x_i, y_i))$ corresponds to the observation dependency, $\Sigma_{ij}(x_i, x_j) = \exp(-H_{ij}(x_i, x_j))$ corresponds to the spatial dependency, $\mathcal{N}_i$ denotes the set of neighbors of node i in $\mathcal{G}$ and z_m is a normalization constant. The belief (marginal) at each node is then calculated by

$$b_i^{(t)}(x_i) = z_b \Sigma_i(x_i, y_i) \prod_{k \in \mathcal{N}_i} m_{ki}^{(t)}(x_i), \tag{2.13}$$

where z_b is a normalization constant. Finally, after the algorithm converges, the final solution (labels) $\hat{\mathbf{x}}$ is calculated at each node as follows:

$$\hat{x}_i = \arg\max_{x_i} b_i(x_i). \tag{2.14}$$

The algorithm starts with the messages initialized at one. A stopping criteria is then imposed by setting a threshold on the average changes in the belief of the nodes, and a threshold on the maximum number of iterations. The final solution is then the estimated $\mathbf{O}_b$, i.e., the 3D binary image of the area of interest.

Defining the Cost Functions

We next define the H_i and H_{ij} that we shall utilize as part of our loopy belief propagation algorithm of Eq. 2.10 and 2.12. Based on the cost functions chosen in the image restoration literature [18], we choose $H_{ij}(x_i, x_j) = (x_i - x_j)^2$ and $H_i(x_i, y_i) = (x_i - y_i)^2$. In several cases, the outer edge of the area of interest, e.g., the pixels corresponding to the outer most layer of the boundary wall, can be sensed with other sensors such as a camera or a laser scanner. In such cases, we can then modify $H_i(x_i, y_i)$ as follows to

enforce this information: $H_i(x_i, y_i) = \begin{cases} (1 - x_i) & \text{if } i \in \Omega_B \\ (x_i - y_i)^2 & \text{otherwise} \end{cases}$, where Ω_B denotes the set of graph nodes that constitute the outer boundary of the domain.

In summary, the solution $\hat{\mathbf{x}}$ that we obtain from the loopy belief propagation algorithm is the estimate of $\mathbf{O}_b$, which is our 3D binary image of the area of interest.

2.3 UAV Path Planning

So far, we have described the system model and the proposed approach for solving the 3D through-wall imaging problem, given a set of wireless measurements. The TX/RX locations where the measurements are collected can play a key role in the 3D imaging quality. By using unmanned aerial vehicles, we can properly design and control their paths, i.e., optimize the locations of the TX/RX, in order to autonomously and efficiently collect the measurements that are the most informative for 3D imaging, something that would be prohibitive with fixed sensors. In this section, we discuss our approach for planning efficient and informative paths for 3D imaging with the UAVs. We start by summarizing the state-of-the-art in path planning for 2D imaging with ground vehicles [58]. We then see why the 2D approach can not be fully extended to 3D, which is the main motivation for designing paths that are efficient and informative for 3D imaging with UAVs.

In [58], the authors have shown the impact of the choice of measurement routes on the imaging quality for the case of 2D imaging with ground vehicles. Let the spatial variations along a given direction be defined as the variations of the line integral described in Eq. 2.2, when the TX and RX move in parallel along that direction outside of the area of interest [58, 3]. Fig. 2.4, for example, marks the 0° and 45° directions for a 2D scenario. We then say that the two vehicles make parallel measurements along the 45° route if the

Figure 2.2: An example scenario with an L-shaped structure located behind the walls.

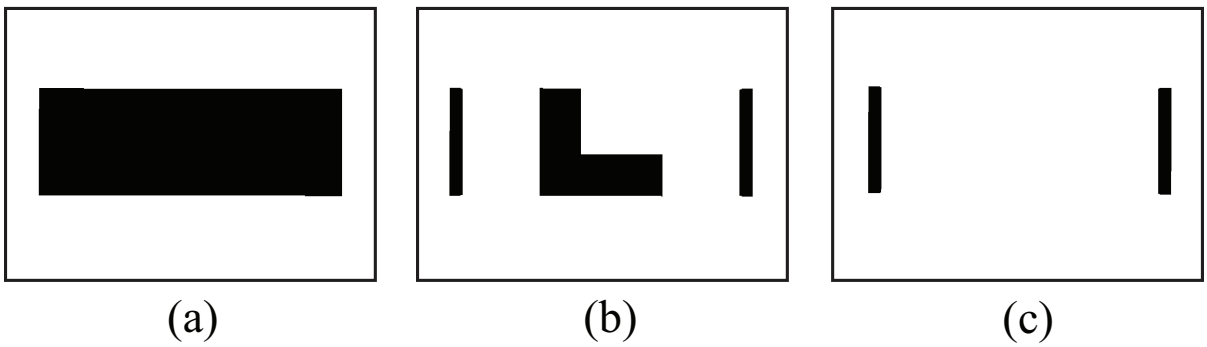

Figure 2.3: 2D cross sections corresponding to three x-z planes at different y coordinates for the area of Fig. 2.2. As can be seen, the information about the variations in the z direction is only observable in (b).

line that connects the positions of the TX and RX stays orthogonal to the 45° line that passes through the origin.[5] Then, for every TX/RX position pair along this route, we evaluate the line integral of Eq. 2.2 and define the spatial variations along this direction as the variations of the corresponding line integral. Furthermore, let the jump directions be defined as those directions of measurement routes along which there exist most abrupt spatial variations.

For the case of 2D imaging using unmanned ground vehicles, the authors in [58] have shown that one can obtain good imaging results by using parallel measurement routes

[5]We note that such routes are sometimes referred to as semi-parallel routes in the literature, as opposed to parallel routes, since the two vehicles do not have to go in parallel. Rather, the line connecting the two needs to stay orthogonal to the line at the angle of interest. For the sake of simplicity, we refer to these routes as parallel routes here.

at diverse enough angles to capture most of the jumps. Since in a horizontal 2D plane, there are typically only a few major jump directions, then measurements along a few parallel routes that are diverse enough in their angles can suffice for 2D imaging. For instance, as a toy example, consider the area of interest of Fig. 2.2. For the 2D imaging of a horizontal cut of this area, we only need to choose a few diverse angles for the parallel routes in a constant z plane.

Next, consider the whole 3D area of Fig. 2.2. The measurements that are collected on parallel routes along the jump directions would still be optimal in terms of imaging quality. However, collecting such measurements can become prohibitive, as it requires additional parallel routes in many x-z or y-z planes. This is due to the fact that the added dimension can result in significant spatial variations along all three directions in 3D. For instance, in order to obtain information about the jumps in the z direction in Fig. 2.2, one would need to design additional parallel routes in various x-z or y-z planes. However, there exist many such planes that will not provide any useful information about the unknown domain. For instance, Fig. 2.3 shows three x-z plane cross-sections for the area of Fig. 2.2. As can be seen, only the plane corresponding to Fig. 2.3 (b) would provide valuable information about the jumps in the z direction. Therefore, a large number of parallel measurements along x-y, x-z, or y-z planes are required to capture useful information for 3D imaging.

In summary, since the jump directions are now distributed over various planes, it can become more challenging to collect informative measurements unless prohibitive parallel measurements in many x-y, x-z, or y-z planes are made. We then propose a path planning framework that would efficiently sample the unknown domain, so that we obtain information about the variations in the z direction as well as the variations in x-y planes, without directly making several parallel routes in x-z or y-z planes. More specifically, in order to efficiently capture the changes in all the three dimensions, we use two sets of

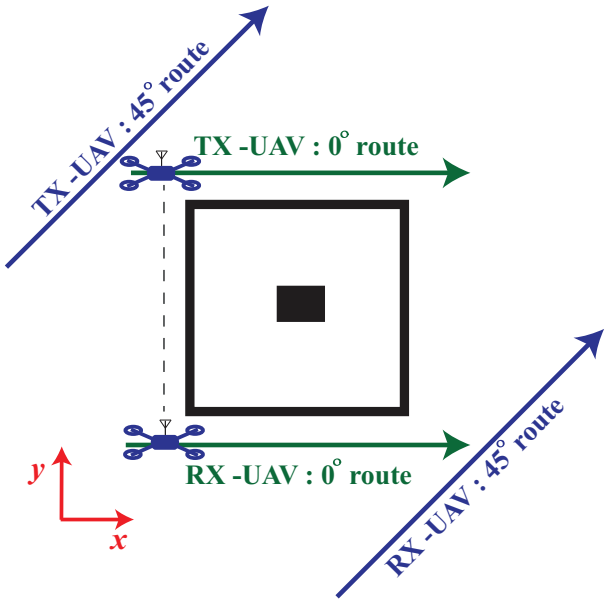

Figure 2.4: An illustration showing the projection of the proposed routes onto the x-y plane. The routes corresponding to 0° and 45° are shown as examples.

parallel routes, as described below:

1. In order to capture the variations in the x-y directions, we choose a number of constant z planes and make a diverse set of parallel measurements, as is done in 2D. Fig. 2.4 shows sample such directions at 0° and 45°.

2. In order to capture the variations in the z direction, we then use sloped routes in a number of planes, two examples of which are shown in Fig. 2.5. More specifically, for a pair of parallel routes designed in the previous item for 2D, consider a similar pair of parallel routes with the same x and y coordinates for the TX and RX, but with the z coordinate defined as $z = a\delta + b$, where δ is the distance traveled along the route when projected to a 2D x-y plane, and a and b are constants defining the corresponding line in 3D. We refer to such a route as a sloped route, and the corresponding plane (that contains two such parallel routes traveled in parallel by two UAVs) as a sloped plane. Fig. 2.4 can then also represent the projection of the

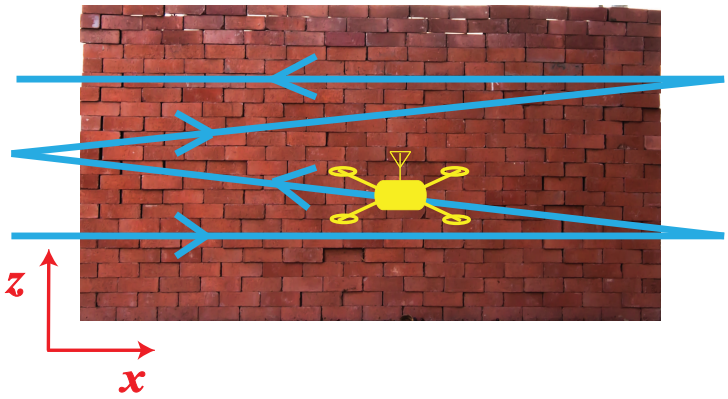

Figure 2.5: Example routes corresponding to two horizontal and two sloped routes for one UAV. The other UAV is on the other side of the domain at the corresponding parallel locations.

parallel routes of the sloped planes onto the x-y plane as well.

Fig. 2.5 shows an example of these two types of routes, for one UAV, along two horizontal and two sloped routes. For each route, the other UAV will traverse the corresponding parallel route on the other side of the structure. When projected to the $z = 0$ plane, all the depicted routes will correspond to $\theta = 0°$ route of Fig. 2.4 in this example.

In summary, while designing parallel routes along x-z or y-z planes can directly capture the changes in the z direction, the sloped routes can also be informative for capturing the variations in the z direction while reducing the burden of navigation and sampling considerably.

2.4 Experimental Testbed

In this section, we describe our experimental testbed that enables 3D through-wall imaging using only WiFi RSSI and UAVs that collect wireless measurements along their paths. Many challenges arise when designing such an experimental setup for imaging through-walls with UAVs. Examples include the need for accurate localization, commu-

nication between UAVs, coordination and autonomous route control. We next describe our setup and show how we address the underlying challenges.

Component	Model/specifications
UAV	3DR X8 octo-copter [59]
WiFi router	D-Link WBR 1310
WLAN card	TP-LINK TL-WN722N
Localization device	Google Tango Tablet [60]
Directional antenna	16dBi gain Yagi antenna 23° vertical beamwidth 26° horizontal beamwidth
Raspberry Pi	Raspberry Pi 2 Model B

Table 2.1: List of the components of our experimental setup and their corresponding specifications.

Table 2.1 shows the specifications of the components that we use in our experiments. The details of how each component is used will be described in the following sections. Fig. 2.6 shows the overall block diagram of all the components and their interactions. We next describe the details of the experimental components.

2.4.1 Basic UAV Setup

We use two 3DR X8 octo-copters [59] in our experiments. Fig. 2.7 shows one of our octo-copters. Each UAV has an on-board Pixhawk module, which controls the flight of the UAV. The Pixhawk board receives information about the flight from a controller (e.g., manual controller, auto-pilot or other connected devices), and regulates the motors to control the flight based on the received information. We have further added various components to this basic setup, as described next.

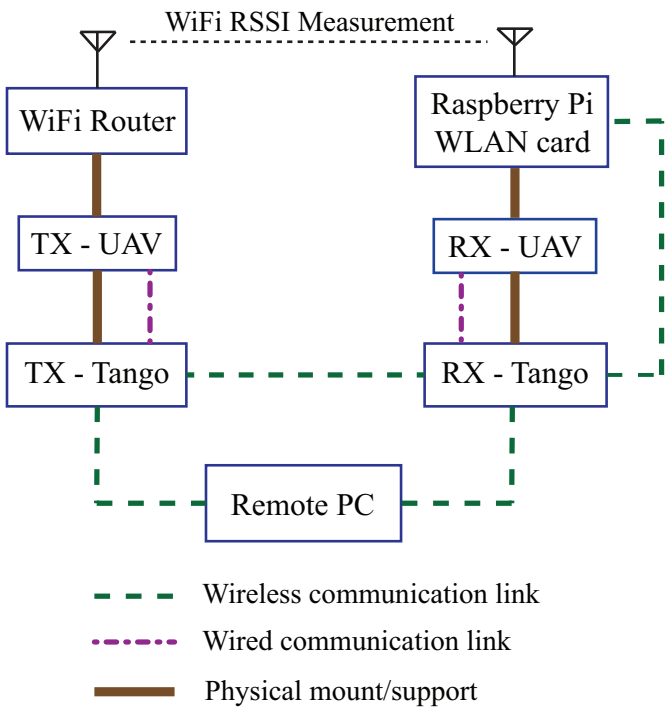

Figure 2.6: A high-level block diagram of the experimental components and their interactions.

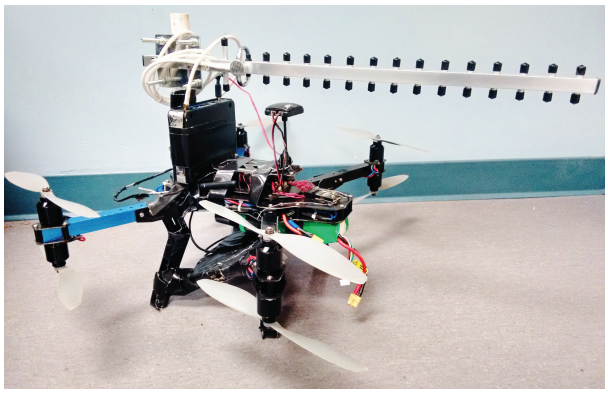

Figure 2.7: A 3DR X8 octo-copter used in our experiments.

(a) (b)

Figure 2.8: The two areas of interest for 3D through-wall imaging. (a) shows the two-cube scenario and (b) shows the L-shape scenario. For better clarity, two views are shown for each area.

2.4.2 Localization

Localization is a crucial aspect of our experimental testbed. In order to image the unknown region, the UAVs need to put a position stamp on the TX/RX locations where each wireless measurement is collected. Furthermore, the UAVs need to have a good estimate of their position for the purpose of path planning. However, UAVs typically use GPS for localization, the accuracy of which is not adequate for high quality imaging. Therefore, we utilize Google Tango Tablets [60] to obtain localization information along the routes. The Tangos use various on-board cameras and sensors to localize themselves with a high precision in 3D, and hence have been utilized for robotic navigation purposes [61]. In our setup, one Tango is mounted on each UAV. It then streams its localization information to the Pixhawk through a USB port that connects to the serial link of the Pixhawk. The Tango sends information to the Pixhawk using an android application that we modified based on open source C++ and Java code repositories [62, 63]. The Pixhawk then controls the flight of the UAVs based on the location estimates. Based on several tests, we have measured the MSE of the localization error (in meters) of the Tango tablets to be 0.0045.

2.4.3 Route Control and Coordination

The UAVs are completely autonomous in their flight along a route. Each Tango initially receives the route information and way-points (short-term position goals) from the remote PC at the beginning of the route. These way-points are equally-spaced position goals located along the route. In our experiments, the projections of these way-points onto the x-y plane are spaced 5 cm apart. During the flight, each Tango uses its localization information to check if it has reached the current way-point along its route (within a desired margin of accuracy). If it has reached its own way-point, it then checks if the other Tango has reached the corresponding way-point along its route. If the other Tango indicates that it has not reached its current way-point, then the first Tango waits until the other Tango reaches its desired way-point. Once the Tangos are coordinated, each Tango sends information about the next way-point to its corresponding Pixhawk. The Pixhawk then controls the flight of the UAV so that it moves towards the next way-point. As a result, both the UAVs are coordinated with each other while moving along their respective routes.

2.4.4 WiFi RSSI Measurements

We next describe our setup for collecting WiFi RSSI measurements. A WiFi router is mounted on the TX UAV, and a WLAN card is connected to a Raspberry Pi, which is mounted on the RX UAV. The WLAN card enables WiFi RSSI measurements, and the Raspberry Pi stores this information during the route, which is then sent to the RX Tango upon the completion of the route. In our experiments, the RX UAV measures the RSSI every 2 cm. More specifically, the RX Tango periodically checks if it has traveled 2 cm along the route from the previous measurement location, when projected onto the x-y plane. If the RX Tango indicates that it has traveled 2 cm, then it records the current

localization information of both the Tangos, and communicates with the Raspberry Pi to record an RSSI measurement. At the end of the route, we then have the desired RSSI measurements along with the corresponding positions of the TX and RX UAVs. Finally, in order to mitigate the effect of multipath, directional antennas are mounted on both the TX and RX UAVs for WiFi signal transmission and reception. The specifications of the directional antennas are described in Table 2.1.

2.5 Experimental Results

In this section, we first show the results of our proposed framework for 3D through-wall imaging, and then compare our proposed approach with the state-of-the-art in robotic 2D through-wall imaging using WiFi. We use our experimental testbed of Section 2.4 in order to collect WiFi RSSI measurements outside an unknown area. The area is then reconstructed in 3D based on the approach described in Section 2.2. In this section, we consider the two areas shown in Fig. 2.8. We refer to the areas of Fig. 2.8 (a) and Fig. 2.8 (b) as the two-cube and L-shape respectively, in reference to the shapes of the structures behind the walls. For both areas, the unknown domain that we image consists of both the outer walls and the enclosed region.

Implementation Details

We first discuss the specific details of our experiments. The dimensions of the unknown areas to be imaged are 2.96 m $\times$ 2.96 m $\times$ 0.4 m for the two-cube scenario, and 2.96 m $\times$ 2.96 m $\times$ 0.5 m for the L-shape scenario.[6] Each WiFi RSSI measurement recorded by

[6]The area to be imaged does not start at the ground, but at a height of 0.65 m above the ground. This is because the Tangos need to be at least 0.35 m above the ground for a proper operation and the antenna mounted on the UAV is at a height of 0.3 m above the Tango. Also, note that the UAVs fly well below the top edge of the walls, and therefore do not have any visual information about the area inside.

the RX-UAV is an average of 10 samples collected at the same position. A median filter is used on the RSSI measurements to remove spurious impulse noises in the measured data. The routes are chosen according to the design described in Section 2.3. For capturing the variations in the x-y directions, two horizontal planes are chosen. The first horizontal plane is at a height of 5 cm above the lower boundary of the area to be imaged, while the second horizontal plane is at a height of 5 cm below the upper boundary of the area to be imaged. In each of these planes, parallel routes are taken with their directions corresponding to $\{0°, 45°, 90°, 135°\}$ (see Fig. 2.4 for examples of $0°$ and $45°$). Additionally, for every pair of such parallel routes, there are two corresponding pairs of sloped routes as defined in Section 2.3 (z coordinate varying as $z = a\delta + b$), with $0.2/D$ representing the slope of each sloped route, where D is the total distance of the route when projected to the x-y plane, 0.2 corresponds to the total change in height along one sloped route, and the offset b is such that the intersection of the sloped routes shown in Fig. 2.5 corresponds to the height of the mid-point of the area to be imaged. This amounts to the total of eight sloped routes and eight horizontal routes, four of which are shown in Fig. 2.5.

We initially discretize the domain into small cells of dimensions 2 cm $\times$ 2 cm $\times$ 2 cm. The image obtained from TV minimization is then resized to cells of dimensions 4 cm $\times$ 4 cm $\times$ 4 cm in order to reduce the computation time of the loopy belief propagation algorithm. The intensity values of the image obtained from TV are normalized to lie in the range from 0 to 1. Furthermore, those values in the top 1% and bottom 1% are directly mapped to 1 and 0 respectively, since they are inferred so close to 1/0, with a very high confidence. The stopping criteria for the belief propagation algorithm is 10^{-4} for the mean change in beliefs, with a maximum of 100 iterations. The information about the outer boundary of the area may be known using cameras or laser scanners. However, only the cells on the boundary (i.e., the last layer of cells on the outer edge) would be

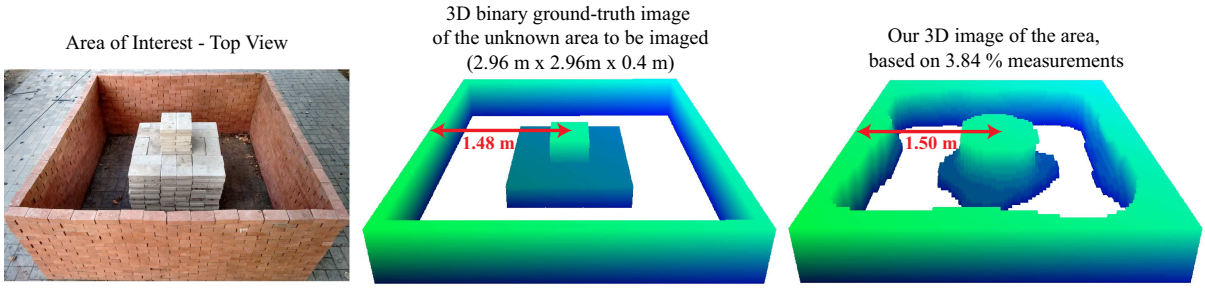

Figure 2.9: (left) The area of interest for the two-cube scenario, (middle) 3D binary ground-truth image of the unknown area to be imaged, which has the dimensions of 2.96 m $\times$ 2.96 m $\times$ 0.4 m, and (right) the reconstructed 3D binary image using our proposed framework.

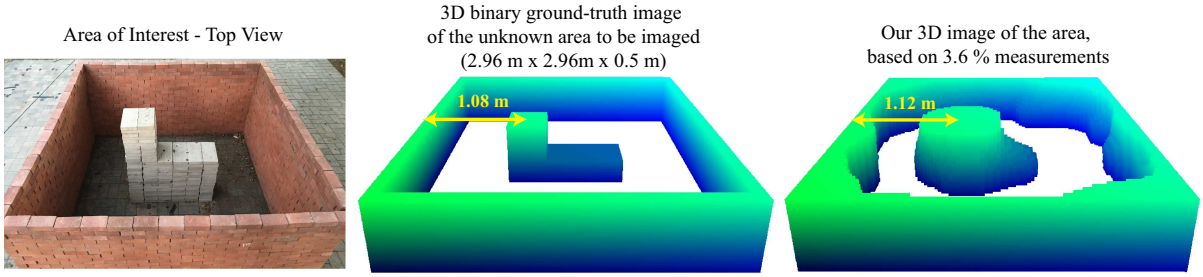

Figure 2.10: (left) The area of interest for the L-shape scenario, (middle) 3D binary ground-truth image of the unknown area to be imaged, which has the dimensions of 2.96 m $\times$ 2.96 m $\times$ 0.5 m, and (right) the reconstructed 3D binary image using our proposed framework.

known to be occupied by a wall in such a case, and the rest of the outer walls need to be imaged, as we shall show next. We next discuss the imaging results for the two scenarios.

3D Imaging Results

Here, we show the experimental 3D imaging results for the two areas shown in Fig. 2.8. Fig. 2.9 (left) shows the region of interest for the two-cube scenario and Fig. 2.9 (middle) shows the 3D binary ground-truth image of the area. Fig. 2.9 (right) then shows the 3D reconstructed image from our proposed approach, using only 3.84% measurements. The percentage measurements refers to the ratio of the total number of measurements

to the total number of unknowns in the discretized space (corresponding to the cells of dimensions 4 cm $\times$ 4 cm $\times$ 4 cm), expressed as a percentage. As can be seen, the inner structure and the outer walls are imaged well, and the variations in the structure along the z direction are clearly visible. For instance, as the figure shows, the distance to the wall from the center of the top part is imaged at 1.50 m, which is very close to the real value of 1.48 m.

We next consider imaging the L-shape area. Note that we are imaging a larger area as compared to the two-cube scenario in this case. Fig. 2.10 (left) shows the region of interest for the L-shape area while Fig. 2.10 (middle) shows the 3D binary ground-truth image of the area. Fig. 2.10 (right) then shows the 3D image obtained from our proposed approach using only 3.6% measurements. As can be seen, the area is imaged well and the L shape of the structure is observable in the reconstruction. Furthermore, the distance to the wall from the center of the top part is imaged at 1.12 m, which is very close to the real value of 1.08 m. It is noteworthy that the inner two-cube structure is imaged at the center, while the inner L-shape structure is imaged towards the left, capturing the true trends of the original structures. Overall, the results confirm that our proposed framework can achieve 3D through-wall imaging with a good accuracy.

We next show a few sample 2D cross sections of the binary 3D images of Fig. 2.9 and 2.10. Fig. 2.11 (a) and (d) show two horizontal cross sections of the 3D binary ground-truth image of the two-cube area of Fig. 2.8 (a), while Fig. 2.11 (b) and (e) show the corresponding cross-sections in our reconstructed 3D image. Similarly, Fig. 2.12 (a) and (d) show two horizontal cross sections for the L-shape area of Fig. 2.8 (b), while Fig. 2.12 (b) and (e) show the corresponding images reconstructed from our proposed framework. In both cases, the different shapes and sizes of the inner structures at the two imaged cross sections are clearly observable.

Comparison with the State-of-the-art

In this section, we compare the proposed 3D imaging approach with the state-of-the-art for through-wall imaging with WiFi RSSI. More specifically, in the current literature [3, 1], robotic through-wall imaging with WiFi power measurements is shown in 2D, with an approach that comprises of the measurement model described in Section 2.1, and sparse signal processing based on Total Variation minimization. However, directly extending the 2D approach for 3D imaging results in a poor performance. This is due to the fact that 3D imaging is a considerably more challenging problem, due to the severely under-determined nature of the linear model described in Section 2.1. Furthermore, by utilizing four measurement routes in the 2D case, every cell in the unknown domain (i.e., a plane in the case of 2D) appears multiple times in the linear system formulation. However, in the case of 3D imaging, there are many cells in the unknown domain that do not lie along the line connecting the TX and RX for any of the measurement routes, thereby never appearing in the linear system formulation. Thus, there is a higher degree of ambiguity about the unknown area in 3D, as compared to the 2D counterpart, which could have only been avoided by collecting a prohibitive number of measurements. Therefore, the contributions of this dissertation along the lines of MRF modeling, loopy belief propagation, and 3D efficient path planning are crucial to enable 3D imaging.

In order to see the performance when directly extending the prior approach to 3D, we next compare the two approaches for the imaging scenarios considered in this chapter. Consider the two-cube area of Fig. 2.8 (a). Fig. 2.11 (c) and (f) show the corresponding 2D cross sections of the 3D image obtained by utilizing the prior imaging approach [1] for our 3D problem. Similarly, for the L-shape area of Fig. 2.8 (b), Fig. 2.12 (c) and (f) show the corresponding 2D cross sections of the 3D image obtained by utilizing the prior imaging approach [1] for our 3D problem.

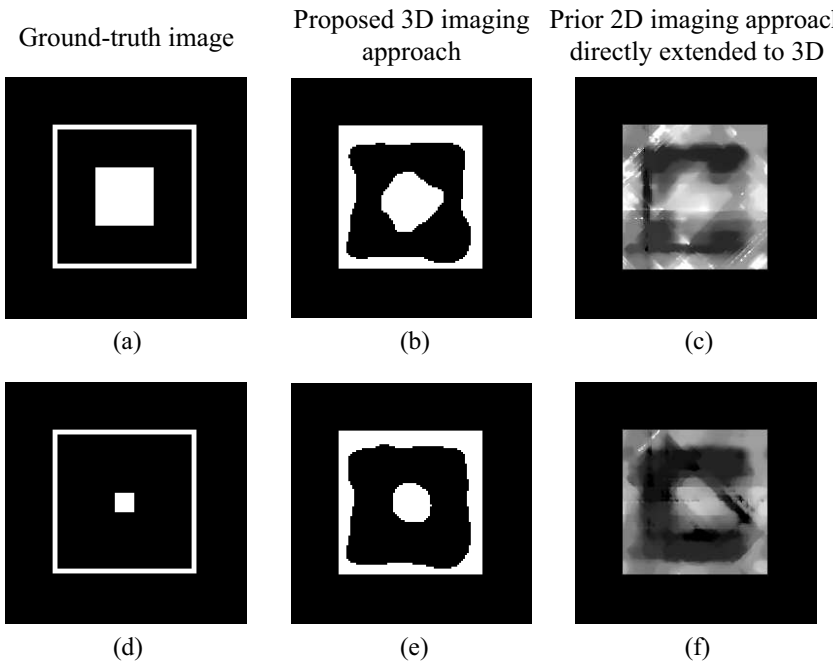

Figure 2.11: Sample 2D cross-sections of the 3D imaging results for the two-cube scenario. (a) and (d) show two 2D cross sections of the ground-truth image, (b) and (e) show the corresponding cross sections of the imaging results obtained from the 3D imaging approach proposed in this chapter, and (c) and (f) show the corresponding 2D cross sections of the 3D image obtained by directly extending the state-of-the-art imaging approach [1] to 3D.

As can be seen, it is challenging to obtain a good 3D reconstruction when directly utilizing the prior approach that was successful for imaging in 2D. There exists significant noise in the image due to the under-determined nature of the system and modeling errors. On the other hand, by incorporating Markov Random Field modeling and solving for the occupancy of each cell via utilizing loopy belief propagation, as we have done in this chapter, we can see that the shapes and locations of the objects are reconstructed considerably more clearly.

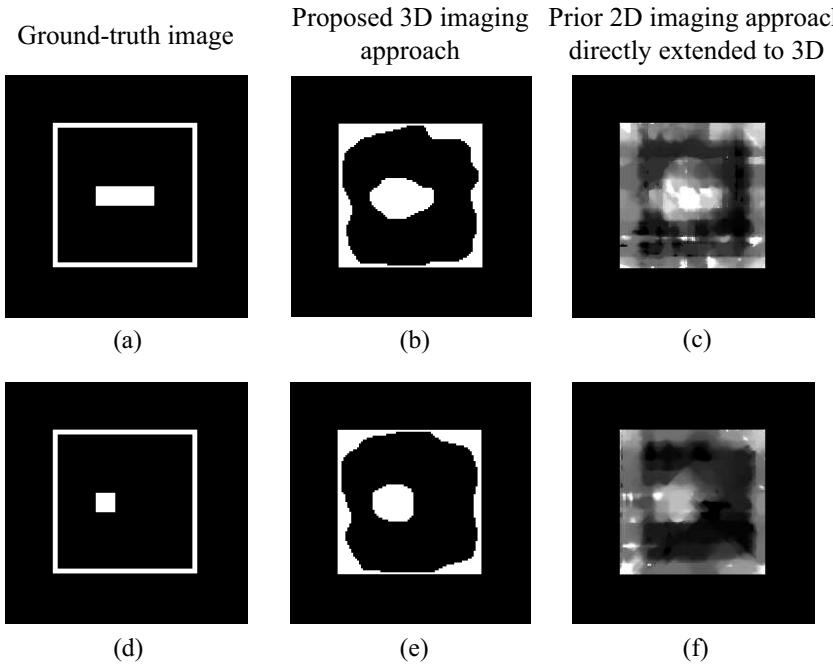

Figure 2.12: Sample 2D cross-sections of the 3D imaging results for the L-shape scenario. (a) and (d) show two 2D cross sections of the ground-truth image, (b) and (e) show the corresponding cross sections of the imaging results obtained from the 3D imaging approach proposed in this chapter, and (c) and (f) show the corresponding 2D cross sections of the 3D image obtained by directly extending the state-of-the-art imaging approach [1] to 3D.

Chapter 3

Magnitude-Based AoA Estimation and Channel Prediction

In this chapter, we are interested in the problem of angle-of-arrival (AoA) estimation, by using only the signal magnitude at an antenna array, without the need for signal phase measurements. Such a framework then opens up new possibilities for implementing RF sensing applications on commercially available off-the-shelf devices, where only the signal magnitude/power can be reliably measured. Thus, in this chapter, we first propose a new framework for AoA estimation using only the signal magnitude measurements at an antenna array. We discuss the ambiguities that can arise in such a magnitude-only AoA estimation problem and show how we can resolve these ambiguities. We then show how to use this magnitude-based AoA estimation framework to predict the ray makeup at unvisited locations in the workspace and subsequently predict the channel quality.

The rest of this chapter is organized as follows. In Sec. 3.1, we show our problem formulation for a general setting of signal paths arriving at an array. In Sec. 3.2, we propose a framework for AoA estimation of signals arriving from fixed sources, and the corresponding angular localization of objects, and show its performance through extensive

experiments. In Sec. 3.3, we show how we can extend our magnitude-based framework in order to fundamentally understand and predict the makeup of the rays and subsequently the channel quality at unvisited locations.

3.1 Our AoA Estimation Foundation

Consider N signal paths arriving at a linear receiver array at various angles, as shown in Fig. 3.1. These signal paths can be caused by active transmitting sources or by passive objects that got illuminated through a transmission in the area. We are then interested in estimating the AoA of these paths, corresponding to all the N sources/objects, using only the magnitude of the received signal at each antenna of the receiver array.[1] Note that for the case of passive objects, AoA estimation results in the angular localization of the objects. In this section, we show that the magnitude of the received signal at the array contains information about the AoA of all the signal paths. This foundation will then be the base for our proposed framework of Sec. 3.2 to estimate the AoA of all the sources.

Consider the receiver array of Fig. 3.1. Let d denote the distance from the first antenna, as denoted on the figure. The baseband received signal, due to the N arriving paths, can be written as a function of distance d as follows [43],

$$c(d) = \sum_{n=1}^{N} \alpha_n e^{j\left(\mu_n - \frac{2\pi}{\lambda} d\cos(\phi_n)\right)} + \eta(d), \tag{3.1}$$

where α_n is the amplitude of the n^{th} signal path, λ is the wavelength of the signal, ϕ_n is the AoA of the n^{th} path (measured with respect to the x-axis), μ_n is the phase of the n^{th} signal at the first antenna of the array, and $\eta(d)$ is the receiver noise. Let $A_{\text{corr}}(\xi)$ denote

[1] We use the term "source" for both active transmitters and passive objects in this chapter.

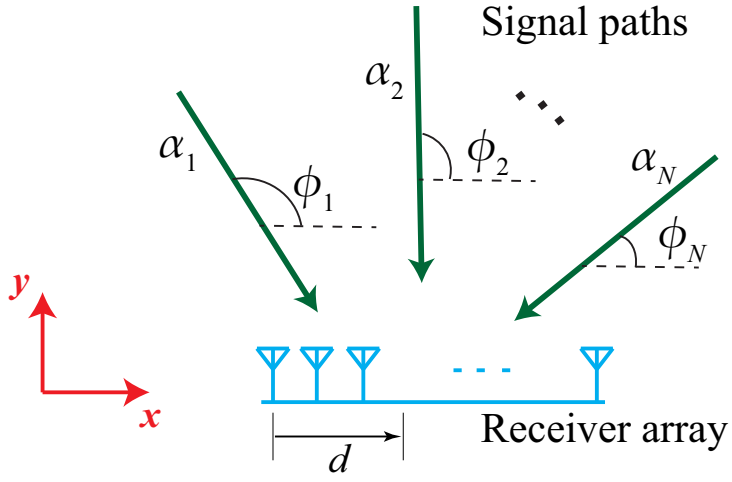

Figure 3.1: N Signal paths arriving at a receiver array.

the auto-correlation function of the baseband received signal magnitude, $|c(d)|$, at lag ξ.

Lemma 2 *$A_{corr}(\xi)$ can be written as follows [43],*

$$A_{corr}(\xi) = C_A + C_{\sigma_\eta}\delta(\xi) + \sum_{n=1}^{N-1}\sum_{m=n+1}^{N} C_{m,n}\cos\left(2\pi\frac{\xi}{\lambda}(\psi_n - \psi_m)\right), \tag{3.2}$$

where C_A is a constant that depends on the total signal power, C_{σ_η} is a constant that depends on the noise variance σ_η^2 and the signal power, $C_{m,n} = \frac{\pi\alpha_m^2\alpha_n^2}{16P}$, $\psi_n = \cos(\phi_n)$, $P = \sum_{n=1}^{N}\alpha_n^2$ is the total power of the received signal, and $\delta(.)$ is the Dirac Delta function.

Proof: See Appendix A.1. ■

Then, by taking the Fourier transform of $A_{\text{corr}}(\xi)$, we get,

$$\mathcal{A}(f) = C_A\delta(f) + C_{\sigma_\eta} + \sum_{n=1}^{N-1}\sum_{m=n+1}^{N}\frac{C_{m,n}}{2}\left(\delta[f - \frac{\psi_n - \psi_m}{\lambda}] + \delta[f + \frac{\psi_n - \psi_m}{\lambda}]\right). \tag{3.3}$$

Eq. 3.3 shows that $|\mathcal{A}(f)|$ has peaks at the frequencies $\pm(|\psi_n - \psi_m|)/\lambda$, for $1 \leq n <$

$m \leq N$.[2] For the sake of simplicity, we normalize the frequency with respect to $\frac{1}{\lambda}$, so that the peaks in the spectrum occur at $\pm|\psi_n - \psi_m|, 1 \leq n < m \leq N$. It can be seen from Eq. 3.3 that the locations of the peaks of $|\mathcal{A}(f)|$ contain information about the AoA of the N signal paths. In the next section, we then propose a framework to use this information and estimate all the AoAs.

3.2 AoA Estimation for Fixed Sources/Objects

In this section, we consider the scenario where there are unknown fixed active or passive signal sources located in an area. We are then interested in estimating the AoAs of the signals from these sources at the receiver array, thus localizing the direction of these sources/objects, using only the magnitude of the corresponding received signal measurements. The signal measurements can be obtained by using an array of fixed antennas, or by using an unmanned vehicle that utilizes its motion to collect measurements along a route, thus synthesizing an antenna array. We next propose a framework to estimate the AoAs of signals from fixed sources. We present extensive experimental results for estimating the AoAs for both active and passive cases.

3.2.1 AoA Estimation Methodology

Consider N signal sources present on one side of a receiver array, i.e., sources whose AoAs $\{\phi_n, 1 \leq n \leq N\}$ satisfy $0^\circ \leq \phi_n < 180^\circ$ (see Fig. 3.1). Let $\Psi = \{\psi_1, \psi_2, \ldots, \psi_N\}$, where $\psi_n = \cos(\phi_n)$. Define the function $D(U)$ on a set of real numbers U as the set of all the unique pairwise distances between the elements of U, i.e. $D(U) = \{|u_i - u_j| : u_i, u_j \in U, i \neq j\}$. Let Q be the set of the absolute values of the pairwise differences of

[2]Note that the Fourier transform of $|c(d)|^2$ also has a similar frequency content. However, the spectrum of $|c(d)|^2$ is considerably more noisy, as compared to $\mathcal{A}(f)$, since the effect of noise is minimized in the auto-correlation, due to the uncorrelated nature of the noise.

the cosines of AoAs, i.e. $Q = D(\Psi)$. Without loss of generality, we assume that Q is ordered: $Q = \{q_1, q_2, \ldots, q_M\}, q_1 > q_2 > \cdots > q_M$. We are then interested in estimating Ψ, and hence the AoAs, using the set of pairwise distances Q, obtained using Eq. 3.3.

The problem of estimating a set of N real numbers, B, given the multiset of absolute differences (distances) between every pair of numbers, ΔB, is called the Turnpike problem [64]. This problem has been explored extensively in the literature and solvers have been proposed for finding its solution [64]. However, it is not possible to obtain a unique solution set using just the set ΔB. For instance, for a solution B, the sets obtained through translation $B + \{e\} = \{b + e : b \in B\}$, mirroring $-B = \{-b : b \in B\}$, or a combination of both $-B + \{e\}$, would also result in the same set of distances ΔB, for any constant e. Furthermore, when the number of points $N \geq 6$, there exist other possible solutions that do not arise from the above construction [64].

The existing solvers for the Turnpike problem require that the set of distances should contain all the $\binom{N}{2}$ pairwise distances (or that we know the multiplicity of the non-distinct distances, if any), and they suffer from the translation and mirroring ambiguities as well as other ambiguities. In our AoA estimation problem though, we will not know the multiplicity of the possible non-distinct distances. Furthermore, we also have to resolve the aforementioned translation and mirroring ambiguity. Thus, we cannot utilize the solvers proposed for the Turnpike problem in our setting. Therefore, in this section we propose our approach to estimate the AoAs from the pairwise cosine distances.

In order to overcome the ambiguity arising due to the translation and mirroring of Ψ, we can place a reference signal source (i.e., a transmitter) at one extreme of the span of angles, say $\phi_{\text{ref}} = 0°$, so that $\psi_{\text{ref}} = 1$. This also implies that any valid solution set would only contain ψs that are less than or equal to ψ_{ref}, a condition we then utilize in our proposed methodology. However, there still exist multiple solutions for a set Q.

We next describe our proposed algorithm to first find all the valid sets of solutions

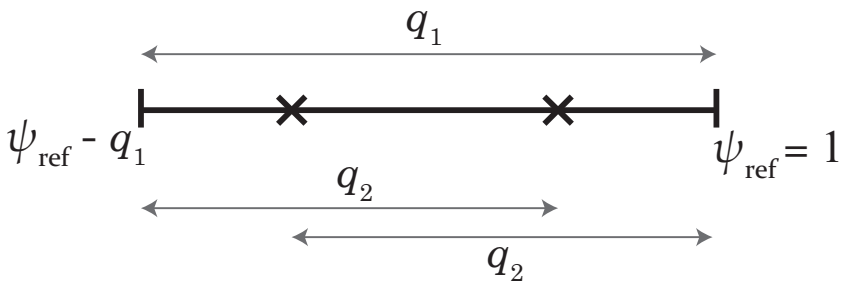

Figure 3.2: Illustration of the reference point, the positioning of the first point corresponding to q_1, and the two possible valid position choices for ψ_2, in our proposed approach.

$\{\psi_n : 1 \leq n \leq N\}$, for a given distance set Q. Then, we show how we can reduce the number of valid solutions (and possibly obtain a unique solution) by utilizing measurements from two arrays in different configurations.

Proposed Approach for Finding All Possible Angle Solutions

We next describe how we can obtain all the valid solution sets corresponding to Ψ, given the ordered set of distances Q, the AoA corresponding to the reference source at $\phi_{\text{ref}} = 0°$, and the estimated number of sources (denoted by $\hat{N}$). We show how to estimate the number of sources in Sec. 3.2.1. Without loss of generality, we take the sets Ψ and Q to include the impact of the new added reference source at ϕ_{ref}, i.e., $\Psi = \{\psi_{\text{ref}}, \psi_1, \ldots, \psi_{N-1}\}$. Then, we are interested in estimating the angles of the rest $N - 1$ unknown sources.

The rightmost and leftmost extreme points of the set Ψ are defined by $\psi_{\text{ref}} = 1$ and $\psi_1 = \psi_{\text{ref}} - q_1$, respectively, as shown in Fig. 3.2. Consider the positioning of the next point ψ_2, corresponding to q_2. Fig. 3.2 shows the two possible valid position choices for it. Both these will result in a valid solution set. Similarly, for each of the remaining distances $q_i, 3 \leq i \leq M$, there exist a pair of positions on the line in Fig. 3.2, whose distance to the two extreme points correspond to that q_i. It is easy to confirm that these

two positions are the only possible positions given the monotonicity of the set Q. This observation is the base of our proposed approach, which we detail next. Let the set $\hat{\mathcal{S}}$ denote the set of all the sets of valid solutions. We start with a valid partial solution, where a Valid Partial Solution (VPS) is a set S such that $D(S) \subseteq Q$. We then find all the valid solutions, as follows:

Initialization: We initialize the set of VPSs with $\mathcal{S}^{(1)} = \{\{\psi_{\text{ref}} - q_1, \psi_{\text{ref}}\}\}$, which is the smallest VPS, containing only the two extreme points of Ψ.

Iteration Update: In iteration i, we place a point at a distance q_i from either of the extremes in the existing VPSs. More specifically, for each set $S \in \mathcal{S}^{(i-1)}$, we generate one test set by adding a point at a distance q_i from the rightmost extreme, and another test set by adding a point at a distance q_i from the leftmost extreme. If the pairwise distances of the new sets are a subset of Q, we then add these test sets to $\mathcal{S}^{(i-1)}$ to generate $\mathcal{S}^{(i)}$.

Algorithm Termination: The algorithm is terminated after $M - 1$ iterations, which corresponds to exhausting all the elements of Q. A set $S \in \mathcal{S}^{(M)}$ is a possible solution for Ψ if the cardinality of S is $\hat{N}$ and $D(S) = Q$. We then use all such sets S to generate $\hat{\mathcal{S}}$, the final set of all the possible solutions. Algorithm 1 shows the pseudo-code for this algorithm.

Remark 1 *It can be easily confirmed that the aforementioned algorithm captures all the possible valid solution sets, even when there are distance multiplicities.*

Remark 2 *Note that ϕ_{ref} does not have to be necessarily $0°$. As long as it is the smallest possible angle (i.e., all the other angles are greater than it), then the previous algorithm works.*

While we have removed the ambiguity due to translation and mirroring, the previous algorithm can still result in a number of valid solutions. If there is no distance multiplicity,

then we can prove that there will only be two solutions by using ψ_{ref}, when the number of unknown sources is less than 5 (see the Turnpike literature [64]). In general, however, there may be more than two possible solution sets. Next, we show how we can further reduce the number of possible solutions.

Algorithm 1 Finding all possible angle solutions

function findAllPossibleAngles($Q,\ \psi_{\text{ref}},\ \hat{N}$)

Initialize $\mathcal{S}^{(1)} \leftarrow \{\psi_{\text{ref}} - q_1, \psi_{\text{ref}}\}$
for all $2 \leq i \leq M$ **do**
  $\mathcal{S}^{(i)} \leftarrow \mathcal{S}^{(i-1)}$
  for all sets $S \in \mathcal{S}^{(i-1)}$ **do**
    $S_1^{\text{test}} \leftarrow S \cup \{\psi_{\text{ref}} - q_i\}$, and $S_2^{\text{test}} \leftarrow S \cup \{\psi_{\text{ref}} - q_1 + q_i\}$
    for all $k \in \{1, 2\}$ **do**
      if $D(S_k^{\text{test}}) \subseteq Q$ **then**
        $\mathcal{S}^{(i)} \leftarrow \mathcal{S}^{(i)} \cup S_k^{\text{test}}$
      end if
    end for
  end for
end for
$\hat{\mathcal{S}} \leftarrow \{S : S \in \mathcal{S}^{(M)}, \text{cardinality}(S) = \hat{N}, D(S) = Q\}$

return $\hat{\Phi}_{\text{all}} = \cos^{-1} \hat{\mathcal{S}}$

AoA Estimation with Multiple Routes

In order to reduce the ambiguity due to multiple possible solutions obtained using Algorithm 1, we propose to use another set of measurements collected by a receiver array with a different orientation. This new magnitude measurement can be obtained either by another fixed receiver array or by an unmanned vehicle that moves along a route with a different orientation. This solution is thus particularly suitable for the case of an unmanned vehicle emulating a receiver array, since traversing two straight routes is a trivial task for an unmanned vehicle. Fig. 3.3 shows an example of this scenario. Suppose

that the AoAs of the signal sources for the first array configuration are $\{\phi_n : 1 \leq n \leq N\}$. For the second array that is tilted by an angle Ω in the clockwise direction, the AoAs are now $\{\phi_n + \Omega \ : 1 \leq n \leq N\}$ and the reference source has an angle of arrival Ω or equivalently, $\psi_{\text{ref}} = \cos(\Omega)$.

Since cosine is not a linear function of its argument, utilizing two sets of array measurements results in different sets of pairwise distances Q and Q'. Therefore, we can obtain the set of all possible angle solutions individually for Q and Q' (using Algorithm 1), and then take the intersection of the two sets to find the common valid solution(s). More specifically, let $\Phi_{\text{all},1}$ and $\Phi_{\text{all},2}$ indicate the AoA solution sets for Q and Q' respectively. The intersection of the two sets $\Phi_{\text{all},1}$ and $\Phi_{\text{all},2} - \{\Omega\}$ is then our final estimated AoAs.[3] Intuitively, the chance that the two routes have more than one possible common set is considerably small. However, it is challenging to theoretically prove the uniqueness, or derive the conditions for the uniqueness of the final solution set. Thus, we leave any such proof to future work. However, we have observed through extensive simulations for up to 8 signal sources that our algorithm results in a unique solution for the AoA estimation problem. Furthermore, if there is more than one solution set in the common set, we can collect measurements along another array route to obtain a unique solution. This online strategy is in particular suitable for the case of an unmanned vehicle emulating an array. We note that our proposed strategy is computationally very efficient. We report on sample times in the next section. We next discuss some aspects of the proposed approach.

Criteria for Choosing Ω*:* The orientation of the second array, Ω, determines the extent of dissimilarity between the sets Q and Q', where a larger Ω is likely to result in a higher dissimilarity. Therefore, it is preferable to use as large an Ω as possible. However, we

[3]Note that in practice, the angles from the two sets $\Phi_{\text{all},1}$ and $\Phi_{\text{all},2}$ (after subtracting Ω from $\Phi_{\text{all},2}$) may never be equal, owing to noise or rounding errors. Therefore, we need to compare the sets within a tolerance level.

require all the sources in the area to lie on one side of the receiver array (i.e., upper half plane) in the second configuration as well. Therefore, we can use the first set of distances Q, to estimate the largest AoA at the first receiver array as $\phi_{\max} = \cos^{-1}(1 - q_1)$. This implies that the possible range of values for Ω is $0 < \Omega < 180° - \phi_{\max}$. Note that if ϕ_{ref} for the first route was $\phi_{\min} > 0$ instead of 0, where $\phi_{\min}$ is smaller than all source angles, then the condition for Ω becomes $-\phi_{\min} < \Omega < 180° - \phi_{\max}$, where $\phi_{\max} = \cos^{-1}(\cos(\phi_{\min}) - q_1)$.

Choice of Number of Sources: Given a set of unique distances Q and Q', we are interested in estimating the AoAs corresponding to the smallest number of sources that can result in the two sets of distances. For N sources, the maximum number of possible pairwise distances is $\binom{N}{2}$. Suppose that the cardinality of sets Q and Q' are M and M'. Therefore, the estimated number of sources $\hat{N}$ should satisfy $M \leq \binom{\hat{N}}{2}$ and $M' \leq \binom{\hat{N}}{2}$, which translate to the conditions: $\hat{N} \geq \frac{1+\sqrt{1+8M}}{2}$ and $\hat{N} \geq \frac{1+\sqrt{1+8M'}}{2}$. Hence, we set $\hat{N}_{\min}$ as the smallest integer satisfying the previous two inequalities.

We start by assuming that we have $\hat{N} = \hat{N}_{\min}$ sources. We then solve for the AoAs for the sets Q and Q' separately, using the approach of Sec. 3.2.1 (Algorithm 1). If the intersection of $\Phi_{\text{all},1}$ and $\Phi_{\text{all},2} - \{\Omega\}$ is an empty set, we then need to increase $\hat{N}$ by 1, until we get a non-empty intersection set of solutions.

Remark 3 *It is highly unlikely that adding an element ψ_{new} to the true set $\mathbf{\Psi}$ or taking out one element of it will produce the same Q and Q' respectively for both the routes. Hence, it is highly unlikely that using any $\hat{N}$ other than the true N will produce non-empty intersection set of solutions.*

Remark 4 *For the case where we are interested in finding all the valid solutions with only one measurement array, $\hat{N}$ can be chosen as $\hat{N}_{min} = \left\lceil \frac{1+\sqrt{1+8M}}{2} \right\rceil$, which corresponds to the smallest number of sources that could have resulted in a cardinality of M for Q. If the current $\hat{N}$ does not result in a valid solution, we then keep increasing $\hat{N}$ by 1 until*

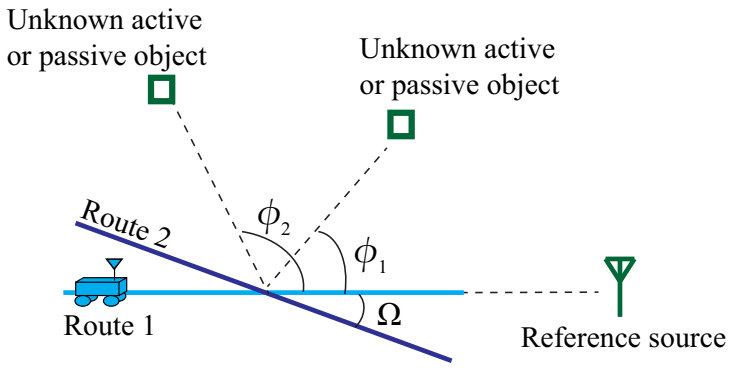

Figure 3.3: Framework for AoA estimation using two routes. Received signal magnitude measurements are collected along two arrays in order to reduce the ambiguity due to multiple sets of possible solutions to the AoA estimation problem.

we get a non-empty solution set.

3.2.2 Static Scene AoA Estimation with Dominant Tx Path

Consider the case that the signals from the unknown signal sources are of lower transmission power as compared to the reference source at ϕ_{ref}. *This case is in particular relevant when we are interested in estimating the direction of passive objects.* Then, the transmitted reference signal will bounce off of these objects and reach the receiver array with a considerably smaller power than that of the path from our reference transmitting source. In such a case, the AoA estimation problem is slightly different, as we show next.

Consider N unknown sources where the paths arriving from them at the receiver array have a lower power as compared to the reference source. This can happen for both the cases of active and passive sources. In the active case, this can happen when the active transmitters have a lower power as compared to our reference source. On the other hand, the passive case results in a dominant reference source almost all the time. Then, from Eq. 3.3, we can see that the pairwise coefficients $C_{m,n}$ that correspond to the pair of the reference source and an unknown source would be the only significant peaks in the spectrum. More specifically, if the dominant reference source with a higher power is at

$0°$, and the unknown sources are at angles $\{\phi_1, \ldots, \phi_N\}$, then the estimated differences from the spectrum are $Q = \{1 - \cos(\phi_1), \ldots, 1 - \cos(\phi_N)\}$ since the rest of differences will have negligible peaks. Therefore, we can directly estimate the AoAs corresponding to the unknown sources as $\{\cos^{-1}(1 - q) : q \in Q\}$.

However, if the dominant reference source is not located at any one extreme of the angular workspace (i.e., if there are sources on either side of the reference source), then we can no longer directly estimate the unknown AoAs from a single array. More specifically, any measurement q that we obtain from the spectrum can now correspond to $\pm(\psi_{\text{ref}} - \psi_n)$. As a result, there now exists an ambiguity regarding the location of the unknown source, where the AoA corresponding to the unknown source can be less than or greater than ϕ_{ref}. More specifically, this ambiguity results in two possible solutions for the AoA of the unknown source, with one solution corresponding to the unknown source being on one side of the line connecting the Tx to the receiver array, and the other solution corresponding to the other side of the aforementioned line. In addition to this ambiguity, the general phased-array AoA estimation problem contains an inherent ambiguity regarding the array halfspace in which the objects are located. More specifically, one antenna array of measurements cannot distinguish between paths arriving from angles ϕ and $-\phi$, since both result in the same measurement of $\cos\phi$. Since in the most general scenario, the objects and the reference Tx can be located anywhere in the workspace, then there is a need for a magnitude-based framework that can resolve all such ambiguities and estimate the AoA of all the paths arriving at the array.

Similar to the problem framework in Sec. 3.2.1, we can resolve these ambiguities by using robotic route diversity. More specifically, since the cosine function is not linear in its argument, we can obtain a different set of pairwise difference measurements in every robotic route, and can use the same algorithm to resolve the ambiguity and estimate the unknown AoAs. However, as the number of sources in the area increases, we would need

more diverse routes in order to resolve the different kinds of ambiguities and subsequently estimate all the AoAs.

In scenarios where it is not possible to use robotic route diversity to resolve these ambiguities, there is a need to estimate the unambiguous AoAs from one antenna array or one robotic route of measurements. We next discuss our proposed magnitude-based approaches to resolve the aforementioned ambiguities and estimate AoAs in general scenarios.

Tx Side Ambiguity Resolution

In this section, we first discuss our proposed approach to resolve the ambiguity regarding which side of the Tx any path is arriving from. Consider Eq. 3.1 again, where we now explicitly describe what constitutes the phase term, as follows:

$$c(d) = \sum_{n=1}^{N} \alpha_n e^{j\left(\frac{2\pi}{\lambda} l_n - \frac{2\pi}{\lambda} d\cos(\phi_n)\right)} + \eta(d), \tag{3.4}$$

where l_n is the total length of the n^{th} path arriving at the first antenna in the array. Then, $|c(d)|^2$, for the case of a dominant reference source (or equivalently, a Tx that illuminates the passive objects in the area) can be written as,

$$|c(d)|^2 \approx \alpha_{\text{ref}}^2 + \sum_{n=1}^{N} \alpha_n^2 + \sum_{n=1}^{N} \alpha_{\text{ref}}\alpha_n \left\{ e^{j\frac{2\pi}{\lambda}(l_{\text{ref}} - l_n)} e^{-j\frac{2\pi}{\lambda} d(\psi_{\text{ref}} - \psi_n)} + e^{-j\frac{2\pi}{\lambda}(l_{\text{ref}} - l_n)} e^{j\frac{2\pi}{\lambda} d(\psi_{\text{ref}} - \psi_n)} \right\}. \tag{3.5}$$

The Fourier transform of $|c(d)|^2$ can then be written as,

$$\begin{aligned} \mathcal{C}(f_d) = (\alpha_{\text{ref}}^2 + \sum_{n=1}^{N} \alpha_n^2)\delta(f_d) + \sum_{n=1}^{N} \alpha_{\text{ref}}\alpha_n \Bigg\{ & e^{j\frac{2\pi}{\lambda}(l_{\text{ref}} - l_n)} \delta(f_d - \frac{(\psi_{\text{ref}} - \psi_n)}{\lambda}) \\ & + e^{-j\frac{2\pi}{\lambda}(l_{\text{ref}} - l_n)} \delta(f_d + \frac{(\psi_{\text{ref}} - \psi_n)}{\lambda}) \Bigg\}. \end{aligned} \tag{3.6}$$

This is similar to the power spectral density that we considered in Sec. 3.1, where there exist two peaks in the spectrum, corresponding to $\pm|\psi_{\text{ref}} - \psi_n|$. In order to resolve the Tx halfspace ambiguity, we then need to estimate the value of $(\psi_{\text{ref}} - \psi_n)$ without any ambiguity regarding its sign.

In order to estimate $(\psi_{\text{ref}} - \psi_n)$, we propose to utilize signal magnitude measurements along a second dimension of frequency. More specifically, we measure the two-dimensional signal magnitude, where we collect WiFi signal magnitude measurements as a function of distance d along the array, and as a function of different subcarrier frequencies at every antenna location on the array. Such a 2D signal measurement framework is easy and practical in real scenarios, since typical WiFi cards already measure WiFi signal magnitude reliably on various subcarrier frequencies. Hence, suppose that the frequency of the measured signal is $f_c + \rho$, where f_c is the center frequency, $\rho \in [-\frac{B}{2}, \frac{B}{2}]$ corresponds to the subcarrier offset frequency that we measure the data on, and B is the total bandwidth of the signal. Rewriting Eq. 3.5 in terms of the measurements along the frequency dimension, we get,

$$|c(d,\rho)|^2 \approx \alpha_{\text{ref}}^2 + \sum_{n=1}^{N} \alpha_n^2 + \sum_{n=1}^{N} \alpha_{\text{ref}}\alpha_n \left\{ e^{j\frac{2\pi}{c}(f_c+\rho)(l_{\text{ref}}-l_n)} e^{-j\frac{2\pi}{c}(f_c+\rho)d(\psi_{\text{ref}}-\psi_n)} + e^{-j\frac{2\pi}{c}(f_c+\rho)(l_{\text{ref}}-l_n)} e^{j\frac{2\pi}{c}(f_c+\rho)d(\psi_{\text{ref}}-\psi_n)} \right\}. \tag{3.7}$$

Since $\frac{2\pi\rho d(\psi_{\text{ref}}-\psi_n)}{c}$ is typically a small quantity compared to the other phase terms, we can neglect it in the expansion. Then, by taking the Fourier transform of $|c(d,\rho)|^2$ along the d dimension and inverse Fourier transform along the ρ dimension, we get,

$$\mathcal{C}_s(f_d,\tau) \approx A\delta(f_d,\tau) + \sum_{n=1}^{N} \alpha_{\text{ref}}\alpha_n \left\{ e^{j\frac{2\pi}{c}f_c L_n} \delta\left(f_d - \frac{\psi_{\text{ref}}-\psi_n}{\lambda_c}, \tau - \frac{L_n}{c}\right) + e^{-j\frac{2\pi}{c}f_c L_n} \delta\left(f_d + \frac{\psi_{\text{ref}}-\psi_n}{\lambda_c}, \tau + \frac{L_n}{c}\right) \right\}, \tag{3.8}$$

where $L_n = l_{\text{ref}} - l_n$, and $A = \alpha_{\text{ref}}^2 + \sum_{n=1}^{N} \alpha_n^2$. Since the path length of the ray from the reference Tx to the receiver array is always less than the path length of the ray from the reference Tx that reflects off of an object and then arrives at the receiver, then $L_n < 0$. Hence, we then propose to utilize this property in the 2D spectrum in Eq. 3.8, in order to eliminate the Tx halfspace ambiguity. More specifically, since $L_n < 0$, by restricting our search space in the 2D spectrum to only negative τ, we would then be able to unambiguously estimate the desired value $(\psi_{\text{ref}} - \psi_n)$. However, in practice, the total bandwidth of the signal determines the resolution of the peak in the τ dimension. For instance, in typical WiFi card measurements, we can only obtain subcarriers corresponding to typical WiFi bandwidth of 20 MHz. While this bandwidth significantly blurs the peak in the τ dimension, it is still informative and can be used to make a binary decision to determine the sign of $\psi_{\text{ref}} - \psi_n$, as we show next. Consider a peak in the 2D spectrum located at $q = |\psi_{\text{ref}} - \psi_n|$ along the f_d dimension. Then, we can determine the sign of $(\psi_{\text{ref}} - \psi_n)$ as follows:

$$\frac{\int_{-\infty}^{0} |\mathcal{C}_s(\frac{q}{\lambda_c}, \tau)|^2 d\tau}{\int_{0}^{\infty} |\mathcal{C}_s(\frac{q}{\lambda_c}, \tau)|^2 d\tau} \underset{\psi_{\text{ref}} - \psi_n = \frac{q}{\lambda_c}}{\overset{\psi_{\text{ref}} - \psi_n = -\frac{q}{\lambda_c}}{\lessgtr}} 1. \tag{3.9}$$

Thus, we can then accurately estimate the AoA of the signal path, and resolve the Tx halfspace ambiguity. Next, we discuss our proposed approach to resolve the array halfspace ambiguity.

Array Halfspace Ambiguity Resolution

As discussed in the previous section, the array halfspace ambiguity is inherent to all linear phased-array AoA estimation problems. A few approaches based on two-dimensional array geometries have been proposed to resolve this ambiguity. For instance, [65] proposes to resolve AoA in 2D by using a circular antenna array. Such a solution

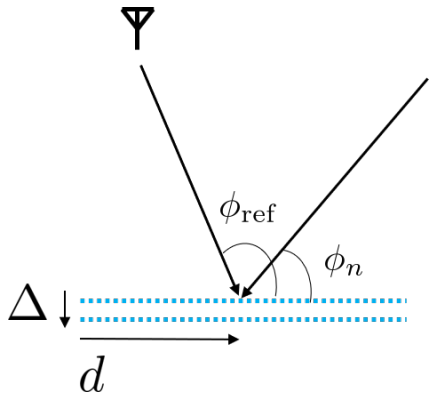

Figure 3.4: Proposed array configuration in order to resolve the halfspace ambiguity of the AoA of paths arriving at an antenna array.

might not always be feasible, especially when a robot needs to measure AoA as it moves along its path and measure AoA at various locations on its path. Forming circular routes at each such location of interest requires significant additional motion energy for the robot. In this section, we then propose an approach that uses the resources already available on a typical WiFi card in order to resolve the array halfspace ambiguity along a linear array or a linear route of the robot.

Consider the scenario shown in Fig. 3.4. We propose to collect signal magnitude measurements in this setting, using a second antenna along the array, which is mounted on the same robot (e.g., placed $\frac{\lambda}{4}$ away from the first antenna). The second dimension, Δ, of the array, is considered to be small as compared to the first dimension. We thus measure the two-dimensional signal magnitude on such an antenna array along the two physical dimensions d and Δ. Note that most off-the-shelf WiFi cards already have the capability to measure the signal magnitude on at least two antennas. We thus propose to utilize this available resource and create a very small antenna array in an orthogonal dimension to resolve the array halfspace ambiguity, as we show next. We can derive the

signal magnitude squared as a function of these two dimensions as follows:

$$|c(d,\Delta)|^2 \approx \alpha_{\text{ref}}^2 + \sum_{n=1}^{N} \alpha_n^2 + \sum_{n=1}^{N} \alpha_{\text{ref}}\alpha_n \Big\{ e^{j\frac{2\pi}{\lambda}(l_{\text{ref}}-l_n)} e^{-j\frac{2\pi}{\lambda}d(\cos\phi_{\text{ref}}-\cos\phi_n)} e^{j\frac{2\pi}{\lambda}\Delta(\sin\phi_{\text{ref}}-\sin\phi_n)} + e^{-j\frac{2\pi}{\lambda}(l_{\text{ref}}-l_n)} e^{j\frac{2\pi}{\lambda}d(\cos\phi_{\text{ref}}-\cos\phi_n)} e^{-j\frac{2\pi}{\lambda}\Delta(\sin\phi_{\text{ref}}-\sin\phi_n)} \Big\}. \quad (3.10)$$

As can be seen from Eq. 3.10, we can theoretically estimate AoAs in two dimensions. We then derive the corresponding spectrum $\mathcal{C}_a(f_d, f_\Delta)$ by taking a 2D Fourier transform along the two dimensions d and Δ, as follows:

$$\mathcal{C}_a(f_d, f_\Delta) = A\delta(f_d, f_\Delta) + \sum_{n=1}^{N} \alpha_{\text{ref}}\alpha_n \Big\{ e^{j\frac{2\pi}{\lambda}(l_{\text{ref}}-l_n)} \delta\left(f_d - \frac{\cos\phi_{\text{ref}} - \cos\phi_n}{\lambda}, f_\Delta + \frac{\sin\phi_{\text{ref}} - \sin\phi_n}{\lambda}\right) + e^{-j\frac{2\pi}{\lambda}(l_{\text{ref}}-l_n)} \delta\left(f_d + \frac{\cos\phi_{\text{ref}} - \cos\phi_n}{\lambda}, f_\Delta - \frac{\sin\phi_{\text{ref}} - \sin\phi_n}{\lambda}\right) \Big\}. \quad (3.11)$$

As a result, there exist two peaks in the 2D spectrum. Utilizing a similar idea as discussed in the previous section to resolve the Tx halfspace ambiguity, we can restrict our current 2D spectrum and estimate the AoA in the full $[0, 2\pi)$ range. More specifically, in the previous section, we already estimated the value of $\cos\phi_{\text{ref}} - \cos\phi_n$ without any ambiguity in its sign. Thus, we can restrict our current 2D spectrum and consider the spectrum values at $f_d = \frac{\cos\phi_{\text{ref}} - \cos\phi_n}{\lambda}$. As a result, denote the location of the peak in the f_Δ dimension as q, where $q = -(\sin\phi_{\text{ref}} - \sin\phi_n)$, as can be seen from Eq. 3.11. Since we know the location of the reference Tx, we can rewrite this expression as $q + \sin\phi_{\text{ref}} = \sin\phi_n$. Thus, we can now estimate the sign of ϕ_n by estimating the sign of $q + \sin\phi_{\text{ref}}$. Note that since the Δ dimension of the 2D array is very small, we would not be able to accurately localize the peak in that dimension due to poor resolution in that dimension. However, we can still make a binary decision regarding the sign of ϕ_n by calculating the

ratio of energies in the spectrum at $f_d = (\cos\phi_{\text{ref}} - \cos\phi_n)/\lambda$. More specifically, we can estimate the sign of ϕ_n as,

$$\frac{\int_{(-\sin\phi_{\text{ref}})/\lambda}^{(-\sin\phi_{\text{ref}}+1)/\lambda} |\mathcal{C}_a(\frac{\psi_{\text{ref}}-\psi_n}{\lambda}, f_\Delta)|^2 df_\Delta}{\int_{(-\sin\phi_{\text{ref}}-1)/\lambda}^{(-\sin\phi_{\text{ref}})/\lambda} |\mathcal{C}_a(\frac{\psi_{\text{ref}}-\psi_n}{\lambda}, f_\Delta))|^2 df_\Delta} \underset{\phi_n \geq 0}{\overset{\phi_n<0}{\lessgtr}} 1. \tag{3.12}$$

In summary, using our proposed magnitude-based framework, we can estimate the AoA of unknown sources arriving at an antenna array, for the general scenario of objects located anywhere in the 2D area, on either side of the reference Tx or array halfspace. We next experimentally validate our proposed framework with several experiments for estimating the AoAs of both the active and passive signal sources.

3.2.3 Experimental Results for AoA Estimation

In this section, we present our experimental results and show the performance of our proposed framework for estimating the AoA in three scenarios: (a) fixed active (transmitting) sources, (b) fixed active sources with a dominant reference source, and (c) fixed passive objects. In the experiments, we use a TP-Link AC1750 WiFi router as a transmitter. The router operates in the 5 GHz band. The output signal of the router is split into N branches using a power divider, in order to create N signal sources for the fixed active source scenario. We use a laptop with Intel 5300 NIC WLAN card as the receiver. The laptop measures the magnitude of the WiFi Channel State Information (CSI) using Csitool [66].[4] The laptop is mounted on a Pioneer 3-AT mobile robot [67], and the robot moves along a linear route. The motion of the robot enables signal measurements at several locations along the route, thus emulating an antenna array. We utilize a spatial sampling frequency of 10 samples/cm, which is well above the Nyquist sampling rate. It

[4]Note that the CSI magnitude captures the channel gain, which can be used as an alternative to the received signal magnitude, without affecting our framework.

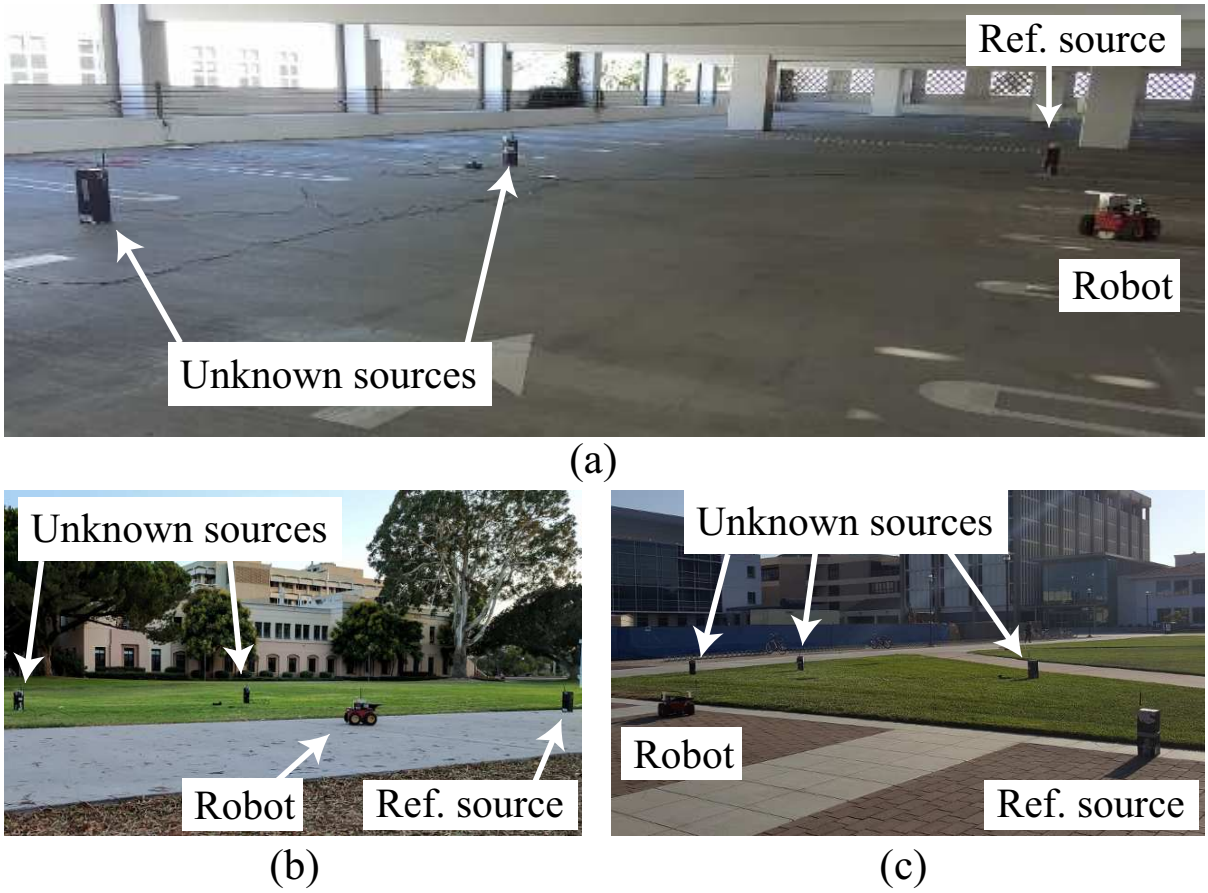

Figure 3.5: Experimental setup for the problem of AoA estimation of active sources in various areas on campus: (a) a closed area in a parking structure, and (b) and (c) open areas.

should be noted that while the Intel 5300 card is capable of reporting a measurement for the phase of the signal, the phase measurement at different robot positions can not be properly related to each other due to frequency drift and other sources of random errors [23].

AoA Estimation of Active Sources

In this section, we present our experimental results for the AoA estimation of signals arriving from multiple active sources (transmitters) in both closed and open areas.

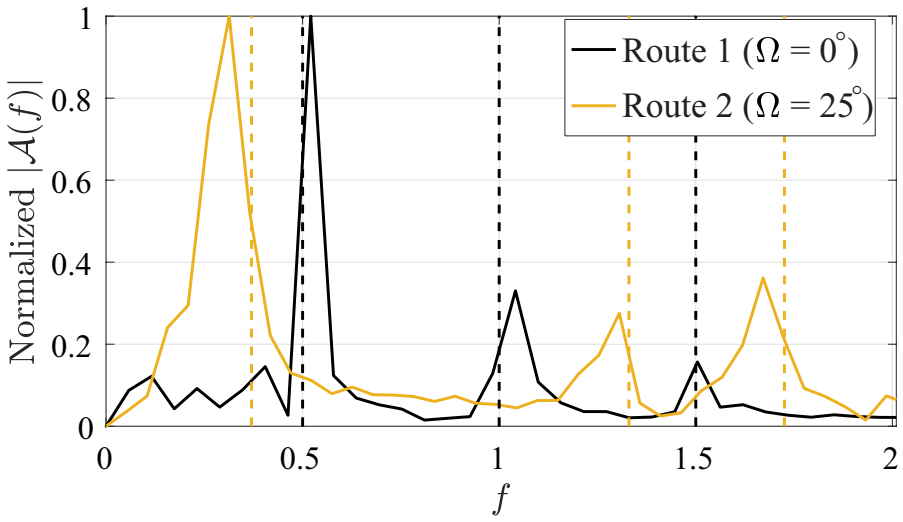

Figure 3.6: The normalized spectra of the auto-correlation of the magnitude measurements obtained for both routes of the robot, for the active-source AoA estimation experiment of the closed area of Fig. 3.5 (a). Dashed lines represent the true theoretical peak locations.

Consider the closed area shown in Fig. 3.5 (a). One reference source is located at an angle $\phi_{\text{ref}} = 0^{\circ}$ and 2 unknown sources are located such that their true AoAs are 90° and 120°. The robot then collects measurements along two routes of length 1 m each, with the orientations of the routes corresponding to $\Omega = 0^{\circ}$ and $\Omega = 25^{\circ}$. Fig. 3.6 then shows the normalized spectra of the auto-correlation functions $|\mathcal{A}(f)|$ across the arrays, for both routes of the robot. It can be seen that the second array configuration results in a different set of distances. We identify the peaks as those points with a minimum prominence value of 10% of the maximum peak (a point is a peak if it is higher than its neighbors by 10% of the max peak value). Then, using our proposed framework of Sec. 3.2.1, we obtain a unique final solution as $\{0, 90.43, 117.57\}$, resulting in a Mean Absolute Error (MAE) of 1.43°.

Additionally, we performed several other experiments in the open and closed areas of Fig. 3.5 (a-c) . Table 3.1 (top) summarizes the results of 4 different experiments carried out in these locations. We can see that our proposed framework can estimate the AoAs

True AoAs	Estimated AoAs	
{66.42, 120}	{67.74, 120.22}	(Top) *Two arrays*
{66.42, 120}	{66.14, 120.29}	
{66.42, 120, 143.13}	{65.99, 117.4, 140.72}	
{90, 120}	{90.43, 117.57}	
MAE	1.3°	
{66.42, 120}	{68.18, 121.27}	(Bottom) *Dominant reference source & one array*
{66.42, 120}	{64.88, 117.7}	
{66.42, 120, 143.13}	{64.59, 117.3, 140.9}	
{66.42, 120, 143.13}	{68.15, 121.1, 146.2}	
{66.42, 120, 143.13}	{61.52, 117.7, 146.2}	
MAE	2.79°	

Table 3.1: Summary of the experimental results for AoA estimation of active sources – (top) solved with proposed approach of Sec. 3.2.1 with two robotic arrays, and (bottom) solved with the proposed approach of Sec. 3.2.2, with a dominant reference source and one robotic array.

of multiple sources accurately, with an overall MAE of 1.3°.

AoA Estimation of Active Sources with a Dominant Reference Source

In the previous results, no assumptions were made regarding the power level of the active sources as compared to the reference source. Instead, two robotic routes were used to uniquely find the AoAs. As we proposed in Sec. 3.2.2, if the reference source is non-negligibly stronger than the unknown active sources, we can then solve for the unknown sources with only one robotic route and with a simpler approach. We next experimentally validate this case. A dominant reference source with a high power is located at an angle $\phi_{\text{ref}} = 0°$. For the dominant reference source, we use an antenna with a 12 dB higher gain than the antennas of the other unknown sources. Table 3.1 (bottom) then summarizes our results using our proposed approach of Sec. 3.2.2, for experiments in the three areas shown in Fig. 3.5. We can see that our proposed framework accurately estimates the AoA in this case as well, with an MAE of 2.79°.

AoA Estimation of Passive Objects

We next present our experimental results for the AoA estimation of passive objects. AoA estimation then refers to estimating the direction of these objects with respect to the antenna array. Consider the scenario shown in Fig. 3.7 (c), for instance. Our reference source is located at an angle of $\phi_{\text{ref}} = 0°$ and two humans are standing at angles $\phi_1 = 90°$ and $\phi_2 = 110°$. Since the reference source will be dominant in the passive case, we can use the framework of Sec. 3.2.2, and directly estimate the AoA, using one robotic array, and from the spectrum shown in Fig. 3.8. As can be seen, the peaks in the spectrum are located at angles 89.14° and 111.4°, which are very close to the true angles, resulting in an MAE of 1.13°. Table 3.2 summarizes the results of 6 different experiments for passive objects, carried out in the four locations shown in Fig. 3.7. This also includes one scenario in the most general setting (the last row of the table), with objects located on all sides of the array and transmitter. In order to estimate the AoAs in this scenario, we utilized the CSI magnitude measurements on the 30 subcarriers logged by the Intel 5300 WiFi card. Additionally, in order to resolve the array halfspace ambiguity, we utilized the CSI magnitude measurements on a second antenna that we placed $\frac{\lambda}{4}$ away from the first antenna, in a direction perpendicular to the robot route (both antennas mounted on one robot). As can be seen from Table 3.2, we are thus able to resolve the ambiguity and estimate the AoAs from all the directions in the 2D area. The overall MAE is 3.2° over all the passive experiments, indicating a very good accuracy.

Performance with Additional Phase Information

We next compare the performance of our magnitude-only approach with the case where phase can be additionally measured in the receiver. More specifically, we performed a set of 5 active-source experiments in the dominant reference source setting,

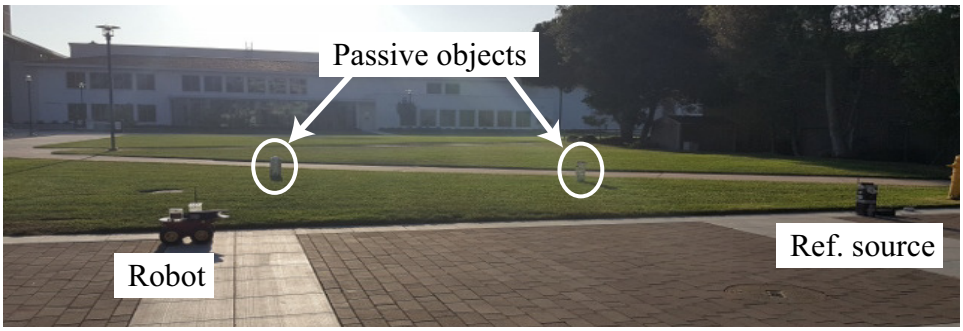

(a)

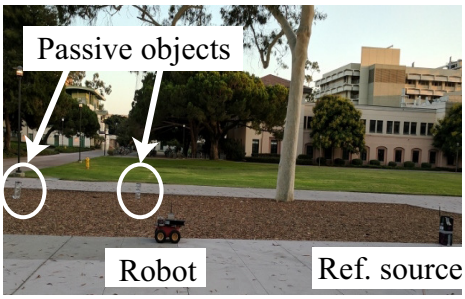

(b)

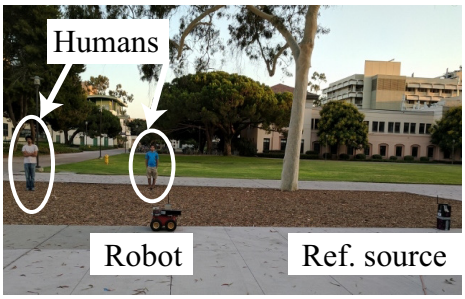

(c)

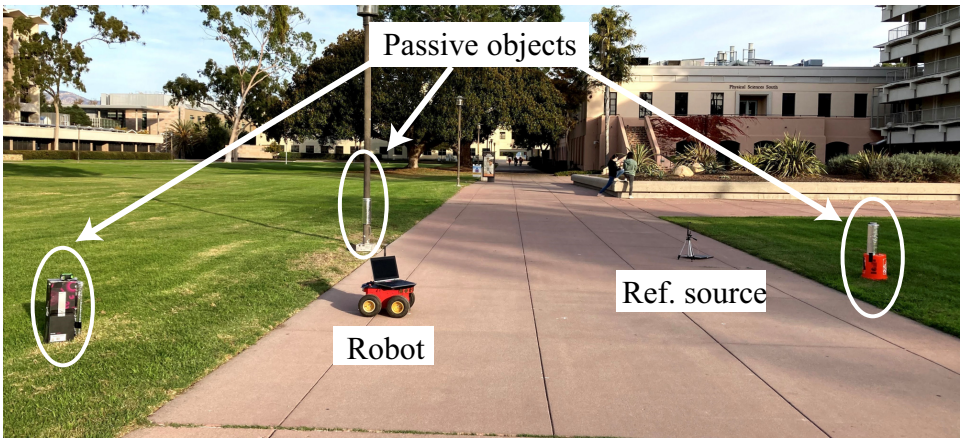

(d)

Figure 3.7: Experimental setup for the AoA estimation (estimation of the direction) of passive sources in various areas on our campus: (a)–(b) passive objects, (c) humans, and (d) general case with objects on both sides of the transmitter/reference source as well as array halfspace.

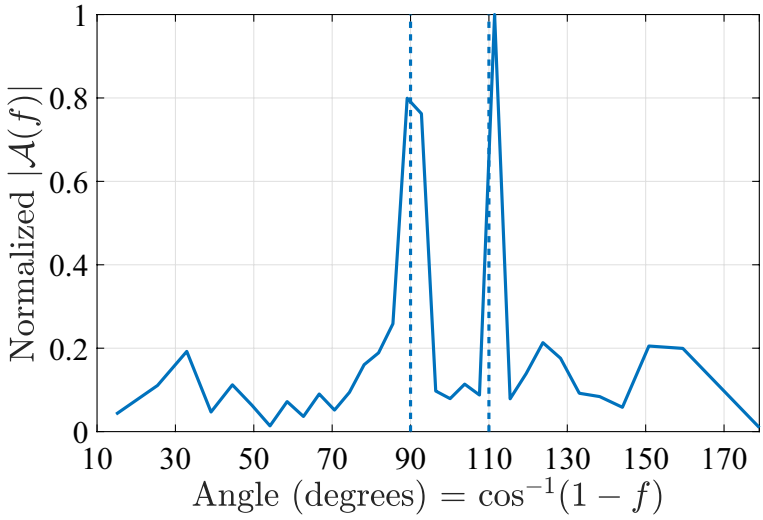

Figure 3.8: A sample normalized spectrum of the auto-correlation of magnitude measurements for the passive case of two humans in the area of Fig. 3.7 (c), using only one robotic array. Dashed lines represent the true AoAs.

True AoAs	Estimated AoAs	
{90, 120}	{92.38, 124.2}	} *2 objects*
{90, 110}	{89.14, 111.4}	
{45, 90}	{42.18, 80.14}	
{45, 69, 90}	{46.68, 64.88, 86.66}	} *3 objects*
{90, 110}	{89.14, 111.4}	} *2 humans*
{29, 117, -150}	{31.8, 119.34, -156.9}	} *3 objects on all sides*
MAE	3.2°	

Table 3.2: Summary of the AoA experimental results (angular localization) for the case of passive objects/humans, using one robotic array.

using USRP N210 Software Defined Radio (SDR) platforms [68], thus measuring both the received signal magnitude and phase. We then estimated the AoAs of signals arriving from the active sources by using the additional phase information and traditional beamforming. The resulting MAE of AoA estimation when additional phase information was available was 0.93°. On the other hand, the corresponding MAE, using our proposed AoA estimation framework and with only magnitude measurements, was 1.76°. This shows that our proposed approach that uses only signal magnitude has a performance comparable to the case where additional phase information is available.

Overall, our proposed framework can accurately estimate the AoA of fixed active sources as well as passive objects, using only magnitude of the received signal measurements. *Our approach is also computationally efficient.* For instance, it took an average of 0.45 seconds (averaged over all the presented results) to find the final solution in MATLAB.

3.3 Robotic Channel Prediction

In this section, we consider the problem of channel prediction, where we are interested in predicting the channel quality at unvisited locations by using a few prior wireless channel measurements collected in the area. We propose a new framework where we methodically design robotic routes such that we optimally collect the required prior channel measurements. We discuss the fundamental parameters that constitute the makeup of the rays in an area and propose a framework to predict these parameters, and subsequently the wireless channel at any unvisited location.

More specifically, we propose to use our magnitude-based AoA estimation framework, to first estimate the fundamental parameters of the rays at optimally designed routes. We then show how we can use those prior measurements to estimate the parameters

of the rays (and the resulting channel quality) at unvisited locations in the space. It is noteworthy that our approach does not depend on localizing the objects in the area. Such an approach is particularly attractive for any general prediction scenario, since the prediction focuses on the rays itself and not on the objects in the area. We next discuss the fundamental parameters constituting the makeup of signal rays propagating in an area.

3.3.1 Estimating the Fundamental Parameters of the Rays

In Sec. 3.2.1, we showed how to use the signal magnitude at an antenna array in order to estimate the angles of arrival of various paths reaching the array. Here, we consider the setup described in Sec. 3.2.2, where we have our own dominant transmitter that illuminates the area, and the rays reflect off of various objects before reaching the receiver antenna array. Consider Eq. 3.5 that characterizes the signal power across the antenna array for this case. In this section, we show how to explicitly estimate the key parameters that constitute the makeup of the rays, from power measurements across the array. In the next section, we then show how to utilize this estimation to predict the ray makeup at unvisited locations using optimally defined routes.

Following are the key parameters that constitute the makeup of the rays:

- $\psi_{\text{ref}} - \psi_n$: We estimate this parameter and the corresponding path AoA ϕ_n based on the location of the peaks in the spectrum, as discussed in Sec. 3.2.2. Note that while we can estimate ψ_n at the array, it is not straightforward to predict it at an unvisited location over the space, since we do not have the corresponding object location and reflection coefficient information. In the next section, we shall see how our proposed path planning problem addresses this challenge.

- α_{ref}: This parameter depends solely on the transmitter and the location of the receiver

antenna. More specifically, $\alpha_{\text{ref}} = \frac{G_t G_r}{4\pi d_{\text{tx}\rightarrow\text{array}}}$, where G_t and G_r are the gains of the Tx and Rx respectively, and $d_{\text{a}\rightarrow\text{b}}$ denotes the distance from a to b. In order to estimate the value of α_{ref} at any unvisited location, we need to estimate the value of the product $G_t G_r$, since $d_{\text{tx}\rightarrow\text{array}}$ is known. Note that the term α_{ref}^2 is the dominant term in the mean of the signal magnitude squared expression discussed in Eq. 3.5. Thus, we can estimate $G_t G_r$ by finding the gain value that minimizes the mean squared error between $\alpha_{\text{ref}}^2 = \frac{(G_t G_r)^2}{(4\pi d_{\text{tx}\rightarrow\text{array}})^2}$ and the spatial mean of all the prior signal magnitude squared measurements collected in the area (in the dB domain). In this manner, we then have an estimate of α_{ref} at any unvisited location in the workspace.

- α_n: We can estimate this parameter from the amplitude of the peaks in the spectrum shown in Eq. 3.6. More specifically, the absolute amplitude of the peaks in Eq. 3.6 corresponds to the quantity $\alpha_{\text{ref}}\alpha_n$. Using our proposed method from the previous item, we can estimate α_{ref} directly from the channel mean. Hence, we can easily estimate α_n from the amplitude we obtain in the spectrum.

  Note that, $\alpha_n = \frac{R_n G_t G_r}{(4\pi d_{\text{tx}\rightarrow\text{obj-n}})(4\pi d_{\text{obj-n}\rightarrow\text{array}})}$, where R_n is the reflection coefficient of the n^{th} object and $d_{\text{a}\rightarrow\text{b}}$ denotes the distance from a to b. Thus, while we can estimate it from the spectrum at the array, predicting it at unvisited locations is not straightforward since we do not have the exact object locations and the reflection coefficient of the object in different angles (i.e., R_n). In the next section, we show how our proposed robot paths enable this prediction.

- $e^{j\frac{2\pi}{\lambda}(l_{\text{ref}} - l_n)}$: We propose to estimate this parameter similar to the previous one, from the corresponding peak in the spectrum. More specifically, as shown in Eq. 3.6, we estimate this complex phase as the phase of the complex amplitude of the corresponding peak in the spectrum. Similar to the previous item, predicting this parameter at unvisited locations requires a new strategy, as we shall see in the next section.

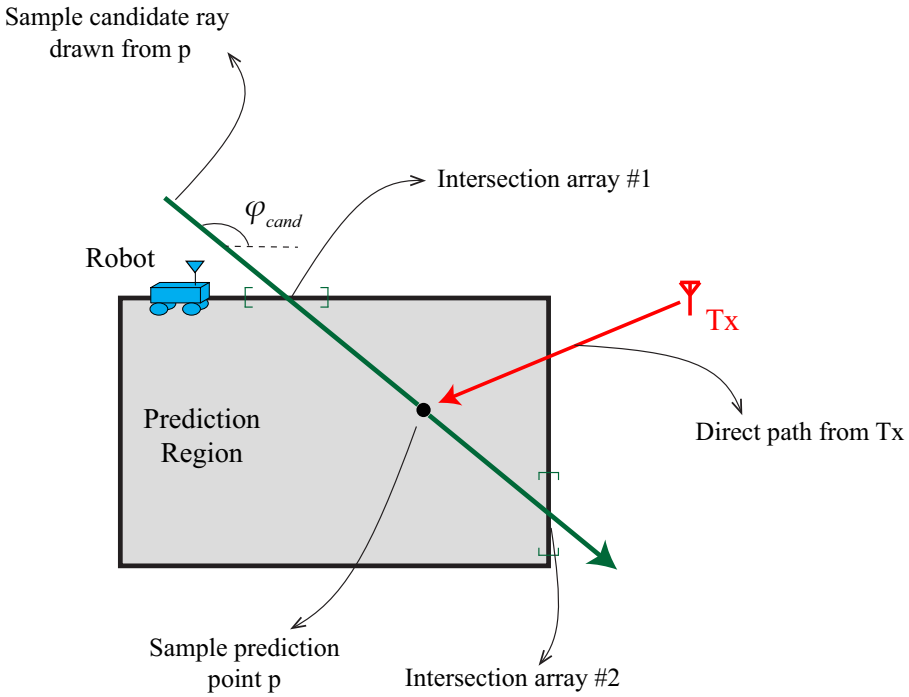

Figure 3.9: Our proposed framework for predicting the channel and its variations at unvisited locations. The robot moves on the boundary of the region of interest to collect measurements and estimate the parameters of the rays in the area.

In summary, predicting the aforementioned parameters at an unvisited location of interest is sufficient to reconstruct and predict the channel strength $|c(d)|^2$ at that location, as can be seen from Eq. 3.5. However, as explained, it is not straightforward to predict these due to lack of object location and full reflectivity information. Thus, we propose a new framework that allows us to address this challenging problem and extend the rays from prior measurement points, to the unvisited locations where we want to predict these parameters. We next describe our proposed framework to predict the parameters and subsequently the channel quality at the desired locations.

3.3.2 Proposed Enclosure-Based Prediction Framework

Consider the scenario shown in Fig. 3.9. We are interested in predicting the ray parameters and the corresponding signal strength in the unvisited shaded region. We

propose an enclosure-based robotic route design such that the robot moves along the boundary of the prediction region and collects signal magnitude measurements. Given these measurements along the boundary, we first form antenna arrays along the route by selecting a spatial moving window of measurements, and subsequently estimating the aforementioned signal parameters at that array (note that we would need all the measurements to estimate the product $G_t G_r$). Hence, at any array formed on the boundary, we can thus estimate the fundamental parameters of all the rays that intersect the boundary at that point. We henceforth refer to the routes on the boundary as measurement routes. Next, we discuss how this design addresses all our previous challenging concerns.

Consider a sample prediction point p in the prediction region, as shown in Fig. 3.9. Using our proposed method, we first estimate $\alpha^2_{\text{p, ref}}$ at the location of interest (we add p to the subscript to indicate the corresponding ray parameters at p). Next, we need to predict the aforementioned reflected ray parameters of all the rays arriving at this point. The key here is that we consider this prediction problem from the perspective of the point where we want to predict the parameters. More specifically, we draw rays passing through the point of interest, at angles ranging from 0 to 2π, in order to scan the angular space and check for valid rays that arrive at this point. As a result, every such ray then intersects the boundary measurement routes at two arrays (see Fig. 3.9). Consider one such sample candidate ray that passes through the prediction point, at angle ϕ_{cand}, as shown in the figure. This ray intersects the boundary at two points. We then form antenna arrays at the two intersections, as shown in the figure. In order to estimate the ray parameters at the point p, we first estimate the ray parameters at the two arrays, i.e., we first estimate the angles ϕ_n, amplitudes α_n, and complex phase of the rays arriving at these two arrays. Next, we check if there exists any ray at the two arrays that corresponds to the angle ϕ_{cand} of the ray that we drew through the prediction point. If this ray indeed originated due to a reflection from an object, we would then observe

the same ray at both the arrays at the corresponding angles. In such a case, we then estimate the corresponding α of this ray at both the arrays, using our proposed approach from the previous section.

Remark 5 *Recall that at any antenna array, there exists an ambiguity regarding the halfspace from which the rays are arriving at the array. We can resolve this ambiguity by using two antennas spaced $\frac{\lambda}{4}$ apart and orthogonal to the robot route, as discussed in Sec. 3.2.2. Alternatively, the robot can collect measurements on a single antenna as it moves along the boundary, and we implicitly resolve the halfspace ambiguity by checking that a particular ray at angle ϕ_{cand} exists at both the intersection arrays on the boundary. By geometrically exploring the problem, one can easily see that checking both intersecting arrays would not resolve the ambiguity only in very low probable cases.*

Remark 6 *Note that we resolve the Tx halfspace ambiguity (i.e., ambiguity regarding which side of the Tx the ray is arriving from) by using signal magnitude measurements along the frequency dimension, as discussed in our proposed framework in Sec. 3.2.2.*

We next show how to estimate the value of the parameter $\alpha_{p,\text{cand}}$ at the prediction point p. Recall that $\alpha_{p,\text{cand}} = G_t G_r \left(\frac{R_{\text{cand}}}{4\pi d_{\text{tx}\to\text{obj-cand}}}\right) \times \left(\frac{1}{4\pi d_{\text{obj-cand}\to p}}\right)$, where "obj-cand" refers to the location of the last reflecting object that results in the considered candidate ray. In the expression for $\alpha_{p,\text{cand}}$, note that we have already estimated the quantity $G_t G_r$ in order to predict α_{ref} at any unvisited location. Then, $\alpha_{p,\text{cand}}$ has two main unknowns: $\left(\frac{R_{\text{cand}}}{4\pi d_{\text{tx}\to\text{obj-cand}}}\right)$ and $d_{\text{obj-cand}\to p}$. The first term is constant along the candidate ray, since it only depends on the object reflection coefficient along that ray, and the distance between the object and the Tx. The second unknown is the distance between the object and the prediction point p. Suppose that the two α values that we estimate on the boundary arrays for this ray are $\alpha_{1,\text{cand}}$ and $\alpha_{2,\text{cand}}$ at points 1 and 2 respectively, where the ray intersects point 1 first. We can then solve for the two aforementioned unknowns at points

1 and 2 using the estimated $\alpha_{1,\text{cand}}$ and $\alpha_{2,\text{cand}}$. We can then easily derive the value of $\alpha_{p,\text{cand}}$ at the prediction point p as follows:

$$\alpha_{p,\text{cand}} = \frac{\alpha_{1,\text{cand}}\alpha_{2,\text{cand}}d_{1\to 2}}{\alpha_{1,\text{cand}}d_{1\to p} + \alpha_{2,\text{cand}}d_{2\to p}}, \tag{3.13}$$

where we have already estimated the quantity (G_tG_r) previously, $d_{1\to p}$ denotes the distance between the first intersection point on the boundary and the prediction point p, and $d_{2\to p}$ similarly denotes the distance between the second point on the boundary and the prediction point p.

Next, we can similarly predict the phase term at the prediction point. We first estimate the complex phase of this ray at the first array that it intersects on the boundary. Suppose we denote this complex phase by $e^{j\mu_{1,\text{cand}}}$. Recall that $\mu_{1,\text{cand}} = \frac{2\pi}{\lambda}(d_{\text{Tx}\to 1} - l_{1,\text{cand}})$, where $l_{1,\text{cand}}$ corresponds to the total length of the reflected ray from the Tx to point 1. We can then extend this phase to the prediction point by adjusting for the extra distance traveled by the ray from point 1 on the boundary to the prediction point, and compensating for the difference in path lengths to the Tx. More specifically, we calculate the new phase term to be $\mu_{p,\text{cand}} = \mu_{1,\text{cand}} - \frac{2\pi}{\lambda}d_{1\to p} - \frac{2\pi}{\lambda}d_{Tx\to 1} + \frac{2\pi}{\lambda}d_{Tx\to p}$. In this manner, we have predicted all the ray parameters for this valid candidate ray. By drawing candidate rays through p, at different angles, and repeating this procedure, we can then get the full makeup of the rays arriving at the prediction point p.

We next utilize this prediction framework to predict the value of the channel at this point by combining the contributions of all the rays, as follows:

$$|c(p)|^2 = \alpha_{p,\text{ref}}^2 + \sum_{\text{all cand. rays}} |c_{\text{cand}}(p)|^2, \tag{3.14}$$

where $|c(p)|^2$ is the predicted total channel power at the prediction point p, and

$|c_{\text{cand}}(p)|^2 = \alpha^2_{p,\text{cand}} + \alpha_{\text{p, ref}}\, \alpha_{p,\text{cand}} \{e^{j\mu_{p,\text{cand}}} + e^{-j\mu_{p,\text{cand}}}\}$, denoting the contribution of a candidate ray to the total power. Note that $c_{\text{cand}}(p) = 0$ for invalid candidate rays. We can thus estimate the channel at any point within the prediction region.

It is noteworthy that our proposed approach to channel prediction does not rely on the precise localization of the objects in the area. Furthermore, it also does not rely on any assumption regarding the reflectivity pattern/coefficient and radar cross sections of the objects in the area. Our framework can be applied to any generic scenario since it only depends on the rays that pass through the area, irrespective of how those rays were generated from the objects, i.e., these rays can be formed by reflection, secondary reflections, or other propagation phenomena such as diffraction and transmission through objects. Our proposed framework handles all these scenarios, since we only extend the rays that are already passing through the workspace.

Note that in our framework, the region where the robot intends to predict the channel needs to be empty, without any objects within the prediction region. Since most robots have on-board vision systems for obstacle avoidance, this assumption is easily satisfied by having the robot explore the desired area so that it does not contain any objects. Alternatively, the robot can also draw boundary regions in order to navigate around any potential objects in the area and exclude them from the prediction region. We note that the prediction area does not have to be convex. For a non-convex prediction region, a ray can intersect the boundary at more than 2 points. In such cases, we only consider the two points that are closest to the prediction point on either side of it, along the candidate ray. In this manner, there is a guarantee that there won't be any objects between these two points, for an empty prediction area.

Remark 7 *Note that the ground reflection can reach the receiver, depending on the receiver antenna height. In such cases, one can model the contributions using established*

models, such as the two-ray model [69], since the enclosure approach cannot properly capture the ground input.

3.3.3 Experimental Results for Channel Prediction

So far, we have discussed our proposed framework for estimating the ray parameters and subsequently predicting the channel variations at any point in the prediction region. In this section, we first describe our experimental setup and the routes along which we collect our measurements. We then show the performance of our proposed approach through experiments conducted on our campus.

Our experimental setup consists of a Pioneer 3-AT ground robot, that moves around the workspace to collect wireless signal measurements. We use two USRP N210 software defined radios as transceivers to transmit and receive wireless signals. We operate the radios at 2.4 GHz and mount one of them on the ground robot, thus enabling the robot to collect wireless signal measurements as it moves. Fig 3.10 (left) shows the experiment area where we collect the measurements. As can be seen, all the objects in this area are on one side of the robot. We then consider two cases for the measurement routes, as shown in Fig. 3.10 (middle) and Fig. 3.10 (right), in order to estimate the parameters of the rays. Each route is 8m long. We collect measurements at locations 1 cm apart on the measurement routes. We then form 1 m long arrays on each route for ray parameter estimation. Note that both route options of Fig. 3.10 (middle) and (right) work similar to the enclosure case since all objects are on one side.

We next show our experimental results. Consider the scenario in Fig. 3.10 (middle). The robot first collects data on the measurement routes, and we use our proposed framework to estimate the parameters of the rays that pass through that area. We then predict the channel variations along a route in the prediction region shown in the figure.

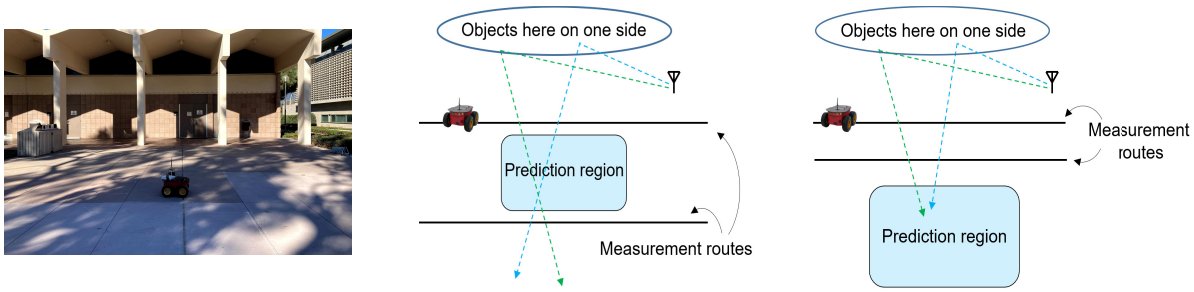

Figure 3.10: (left) Experiment area with the Pioneer 3-AT robot for measuring the signal magnitude and subsequently predicting it at unvisited locations. (middle) An illustration of the setup with the measurement routes around the prediction region where the robot aims to predict the channel and its variations. (right) An illustration of the setup with the measurement routes located on one side of the prediction region.

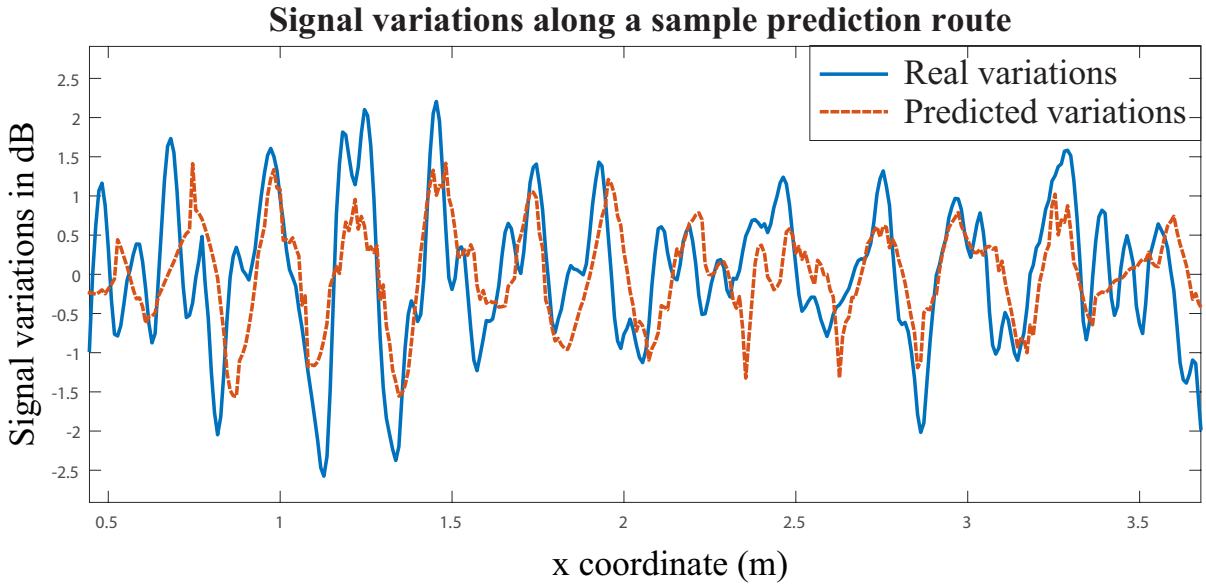

Figure 3.11: Predicted signal variations along a sample route in the prediction region of Fig. 3.10 (middle). As can be seen, the predicted variations match the true variations closely, thereby accurately predicted the fine multipath variations in the area.

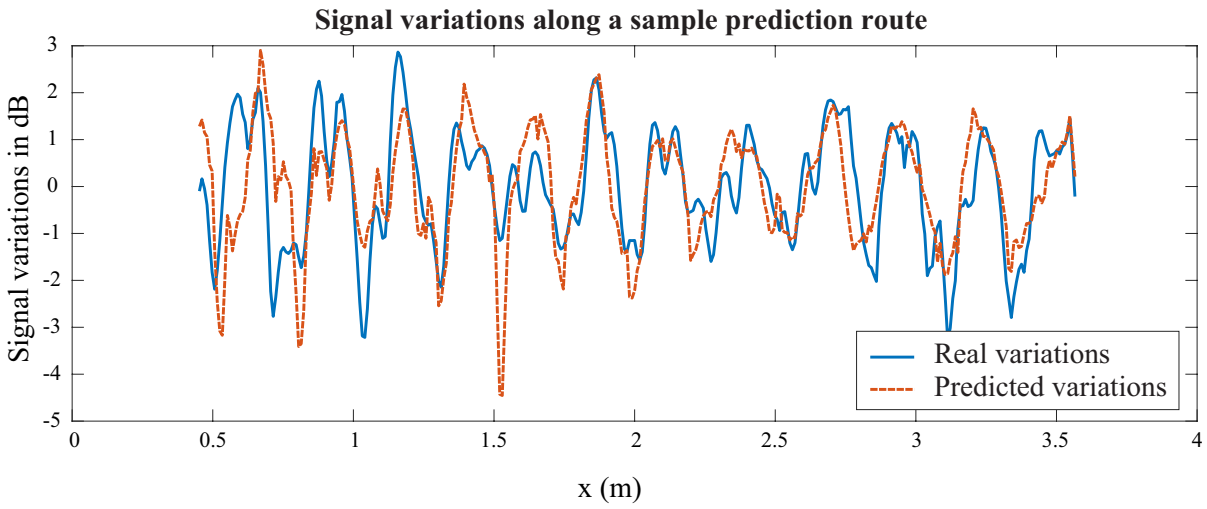

Figure 3.12: Predicted signal variations along a sample route in the prediction region of Fig. 3.10 (right). As can be seen, the predicted variations match the true variations closely, thereby accurately predicted the fine multipath variations in the area.

Note that, we are specifically showing the variations in the channel around the mean, in order to focus on the prediction of multipath and reflections in the area on the channel, which is typically challenging. In order to compare the prediction to the ground truth, the robot collects ground truth channel measurements on the prediction route. Fig. 3.11 shows the comparison between the ground truth channel variations and the predicted variations using our proposed framework. As can be seen, the prediction matches the ground-truth well, and we are successfully able to predict the small-scale variations that arise due to multipath.

We next consider the scenario in Fig. 3.10 (right), with both the measurement routes on one side of the prediction region. Fig. 3.12 shows the comparison between the ground truth channel variations and the predicted variations using our proposed framework, on one route in the prediction region. As can be seen, the prediction matches the ground-truth in this case as well.

In summary, in this section, we have proposed a new channel prediction framework

that predicts the fundamental parameters of the rays at unvisited locations in the area, and subsequently predicts the channel and all its variations at unvisited locations with good accuracy.

Chapter 4

Multi-Person Passive Tracking

In the previous chapter, we showed how we can estimate the angles-of-arrival (AoA) of various paths arriving at a receiver antenna array using only the signal magnitude, without the need for signal phase measurements. This then opens up new possibilities for other AoA-based problems, including localization and tracking. Using the magnitude of the signal in order to passively track a moving person is a problem of considerable interest. In this chapter, we describe our proposed framework for achieving passive tracking of multiple people walking simultaneously in an area, using only the magnitude of WiFi signals measured on devices located on one side of the area.

The rest of this chapter is organized as follows. In Sec. 4.1, we describe our proposed magnitude-based two-dimensional framework for the estimation of AoA parameters. In Sec. 4.2, we show how to track multiple moving targets using a particle filter with a JPDAF. We experimentally validate our proposed framework for tracking multiple targets in Sec. 4.3.

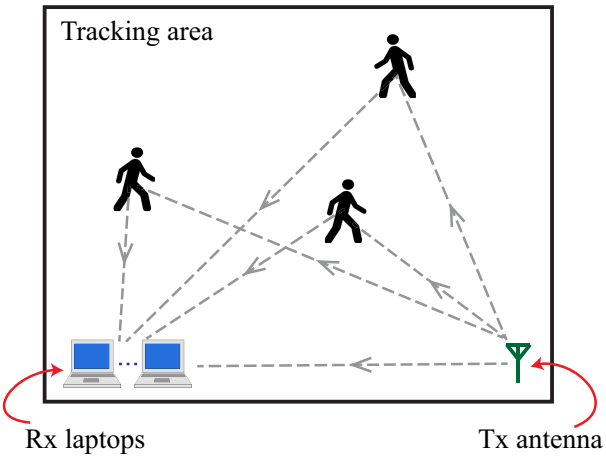

Figure 4.1: An illustration of our passive multi-person tracking setup. N people are walking in an area. A WiFi link consisting of one Tx antenna and one small Rx array (for instance, from a couple of laptops) is located on one side of this area. We are then interested in estimating the tracks of the N people walking in the area using only the magnitude of the received WiFi signal measurements.

4.1 Proposed 2D Framework for Multi-Person Tracking

Consider N people walking in an area, as shown in Fig. 4.1. A WiFi transmitter (Tx) and a small WiFi receiver (Rx) array (for instance, from a couple of laptops) are located on one side of the area. The WiFi signals in the area are scattered and reflected off of the people and the objects present in the area. When these signals reach the receiver, they implicitly contain information about the people and objects that they interact with, on their path from the transmitter to the receiver. More specifically, as we shall see, these signals can be used to infer the location and the track of the people walking in the area. In this section, we show how to model this interaction of WiFi signals with the people and the environment, in order to obtain valuable information on their whereabouts. We next describe the information that can be extracted from the magnitude of WiFi signals in such a scenario. As mentioned earlier, the advantage of using such a magnitude-based approach is that any number of antennas from different receivers can be added

to the array to extend its length if the scenario warrants it, without any need for phase synchronization or phase correction.

4.1.1 Review of 1D Signal Analysis

In this section, we provide a brief primer on the various target parameters that can be extracted from a one-dimensional signal measured using the framework shown in Fig. 4.1. More specifically, we first discuss the AoA information that can be extracted using only the magnitude of the signal measured at a receiver antenna array. Then, we discuss the virtual array parameters created by a person's motion, which can be extracted from the magnitude measurements at a single receiver antenna over time. We henceforth refer to these two dimensions of measurements as the *Rx array angle-of-arrival parameters* and *Motion-induced array parameters*.

Rx Array Angle-of-Arrival Parameters

Consider the receiver array shown in Fig. 4.2. The baseband received signal (or equivalently, the baseband channel gain) at the Rx array at one time instant due to the WiFi signal transmissions in the area can be written as a function of the distance d along the array as follows [43]:

$$c(d) = \alpha_0 e^{j\mu_0} e^{-j\frac{2\pi}{\lambda} d\cos\phi_0} + \sum_{n=1}^{N} \alpha_n e^{j\mu_n} e^{-j\frac{2\pi}{\lambda} d\cos\phi_n} + \eta(d), \tag{4.1}$$

where α_n is the amplitude (or equivalently the gain) of the received signal path from the n^{th} target at the first antenna, μ_n is the phase at the first antenna, ϕ_n is the angle-of-arrival corresponding to the n^{th} path, α_0 and ϕ_0 are the amplitude and angle-of-arrival corresponding to the direct signal path from the transmitter to the receiver array, N is the number of targets in the area, λ is the signal wavelength, and $\eta(d)$ is the receiver

noise. The Fourier transform of $|c(d)|^2$ for the case of passive targets ($\alpha_0 >> \alpha_n$) can be derived as,

$$\begin{aligned} C(f_d) &= A\delta(f_d) + \sum_{n=1}^{N} \alpha_0\alpha_n e^{j(\mu_0-\mu_n)}\delta\left(f_d - \frac{\psi_n^A}{\lambda}\right) \\ &\quad + \sum_{n=1}^{N} \alpha_0\alpha_n e^{-j(\mu_0-\mu_n)}\delta\left(f_d + \frac{\psi_n^A}{\lambda}\right) + \zeta_d(f_d), \end{aligned} \tag{4.2}$$

where f_d is the spatial frequency, $\delta(.)$ is the Dirac delta function, $A = \sum_{n=0}^{N} \alpha_n^2$, $\psi_n^A = \cos\phi_0 - \cos\phi_n$, and $\zeta_d(f_d)$ is the frequency domain modeling error term. As can be seen, there are peaks in the spectrum $C(f_d)$ at frequencies (normalized with respect to $1/\lambda$) corresponding to $\pm\psi_n^A$. Therefore, given a path with angle-of-arrival ϕ_n, we see two peaks in the spectrum corresponding to the two frequencies $\pm(\cos\phi_0 - \cos\phi_n)$. We then have an ambiguity in the AoA of that path, due to the ambiguity in the sign of ψ_n^A.

In the context of tracking multiple targets, the estimation of the AoAs of the targets from Eq. 4.2 localizes the targets to a small extent. However, the previously-mentioned ambiguity in the sign of ψ_n^A hinders our ability to accurately estimate these angles for each target. Furthermore, the resolution and the number of angles that can be estimated is limited by the length of the receiver antenna array, which we assume to be small. This is a crucial aspect that we address in this chapter, since there could be a relatively large number of signal paths arriving at the receiver due to reflections off of multiple targets as well as static objects in the area.

Motion-Induced Array Parameters

Next consider the scenario of measuring the time series of the received signal at a single antenna of the array shown in Fig. 4.2. As the targets move in the area, they

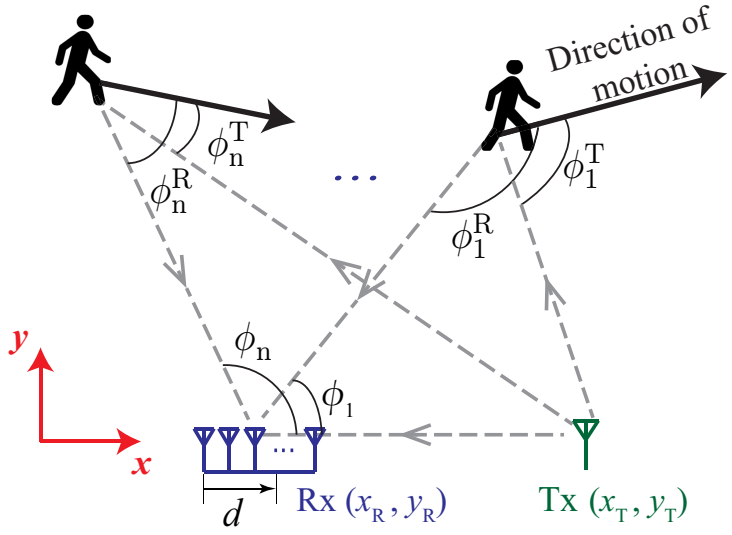

Figure 4.2: Signal model for the multi-target tracking problem. One temporal snapshot of the measurements at the small receiver array can estimate the array-based angles-of-arrival of the targets, and measurements over time at one antenna of the array can estimate the motion-induced array parameters of a moving target, using only the magnitude of the received signals.

create equivalent virtual antenna arrays when the signal receptions at the antenna are considered over time. The temporal received signal in such a case can be written as,

$$c(t) = \alpha_0 e^{j\mu_0} + \sum_{n=1}^{N} \alpha_n e^{j\mu_n} e^{-j\frac{2\pi}{\lambda}\psi_n^M t} + \eta(t), \tag{4.3}$$

where α_n is the amplitude of the path and μ_n is the phase of the path arriving from the n^{th} moving target at time $t = 0$, $\psi_n^M = v_n(\cos\phi_n^R + \cos\phi_n^T)$ is the motion-induced array parameter that arises from the virtual antenna array created by the motion of the n^{th} target, ϕ_n^R and ϕ_n^T are angles with respect to the direction of motion as shown in Fig. 4.2, v_n is the speed of the n^{th} target, and $\eta(t)$ is the receiver noise. Consequently, the magnitude of the signal can be used to estimate the motion-induced array parameter ψ_n^M, which contains information about the location of the corresponding target. The spectrum

of $|c(t)|^2$ generated with respect to the variable t can then be written as follows:

$$C(f_t) = A\delta(f_t) + \sum_{n=1}^{N} \alpha_0 \alpha_n e^{j(\mu_0 - \mu_n)} \delta(f_t - \frac{\psi_n^M}{\lambda}) + \sum_{n=1}^{N} \alpha_0 \alpha_n e^{-j(\mu_0 - \mu_n)} \delta(f_t + \frac{\psi_n^M}{\lambda}) + \zeta_t(f_t), \tag{4.4}$$

where f_t is the frequency variable, and $\zeta_t(f_t)$ is the modeling error term in the spectrum. In the spectrum in Eq. 4.4, we see peaks at locations $\pm\psi_n^M$, thereby exhibiting ambiguity regarding the sign of ψ_n^M for the n^{th} target. Furthermore, the value ψ_n^M itself does not localize the n^{th} target, since different locations, headings and speeds of the target can result in the same value of ψ_n^M. However, it is a function of the targets' motion parameters, which is still informative and can be utilized to track the moving targets over time [70].

In summary, both the Rx array angle-of-arrival parameters (ψ^A) and motion-induced array parameters (ψ^M) measure different quantities related to the targets' locations and headings, but are ambiguous in the sign of the respective measurements as well as the locations they correspond to, in the area of interest. We next propose a framework to jointly estimate both quantities, and show that this joint estimation additionally eliminates the ambiguity in the signs of the individual measurements. Sec. 4.2 then shows how to resolve the residual location ambiguity and fully track the targets.

4.1.2 Multi-Dimensional Signal Analysis for Target Tracking

So far, we have seen that the Rx array angle-of-arrival (ψ^A) and motion-induced array parameters (ψ^M) contain different kinds of information about the targets in the area. In this section, we propose to estimate these parameters jointly, by using the magnitude-based framework to generate a joint spectrum. Consider the multi-dimensional received signal $c(t, d)$, which is a function of time t and distance d along the array, written as

follows:

$$c(t,d) = \alpha_0 e^{j\mu_0} e^{-j\frac{2\pi}{\lambda}d\cos\phi_0} + \sum_{n=1}^{N} \alpha_n e^{j\mu_n} e^{-j\frac{2\pi}{\lambda}\psi_n^M t} e^{-j\frac{2\pi}{\lambda}d\cos\phi_n} + \eta(t,d), \tag{4.5}$$

where $\eta(t,d)$ is the receiver noise. The two parameters ψ^A and ψ^M then appear jointly in the two-dimensional spectrum generated from $|c(t,d)|^2$. More specifically, the 2D spectrum of $|c(t,d)|^2$ can be written as

$$\begin{aligned} C(f_t, f_d) =& A\delta(f_t) + \sum_{n=1}^{N} \alpha_0\alpha_n e^{j(\mu_0-\mu_n)} \delta(f_t - \frac{\psi_n^M}{\lambda}, f_d - \frac{\psi_n^A}{\lambda}) \\ &+ \sum_{n=1}^{N} \alpha_0\alpha_n e^{-j(\mu_0-\mu_n)} \delta(f_t + \frac{\psi_n^M}{\lambda}, f_d + \frac{\psi_n^A}{\lambda}) + \zeta_{t,d}(f_t, f_d), \end{aligned} \tag{4.6}$$

where $\delta(.,.)$ is the 2D Dirac delta function, and $\zeta_{t,d}(f_t, f_d)$ represents the modeling error term in the 2D spectrum. The locations of the peaks in this 2D spectrum then give the corresponding pairs of ψ^A and ψ^M values for each of the moving targets. By using a joint estimation framework, the chance of two targets resulting in the same peak considerably decreases. For instance, two targets could have the same ψ^A values, but they could be different in their ψ^M values, or vice versa. Such scenarios are now well separated in the 2D spectrum.

Note that in the joint spectrum in Eq. 4.6, we still obtain two peaks corresponding to each target in the area. For instance, the n^{th} target generates peaks in the spectrum at (ψ_n^M, ψ_n^A) and $(-\psi_n^M, -\psi_n^A)$. However, by choosing the location of the transmitter appropriately, we can eliminate this ambiguity. To this end, we propose to place the transmitter at one extreme of the angle-of-arrival space of the receiver array ($\phi_0 = 0°$ or $\phi_0 = 180°$). Without loss of generality, suppose that we place the transmitter such that $\phi_0 = 0°$, as shown in Fig. 4.2. Then, $\psi_n^A = 1 - \cos\phi_n$, which is a quantity that lies in the

interval $[0, 2]$. This implies that $-\psi_n^A$ lies in $[-2, 0]$. Since these two intervals are disjoint, we can restrict the search space of ψ^A in the spectrum to the $[0, 2]$ interval. Then, the n^{th} target generates only one peak in the limited spectrum at (ψ_n^M, ψ_n^A), thereby eliminating the ambiguity in the sign of both the ψ parameters. We henceforth use this configuration in all the discussions in this chapter. A similar analysis can be derived for the case when the transmitter is located such that $\phi_0 = 180°$. Thus, our proposed joint framework eliminates the ambiguity in the peaks and provides a larger search space for multiple targets in the spectrum. Fig. 4.3 shows an example of a 2D spectrum with 3 peaks corresponding to 3 targets in the region $-2 \leq \psi^M \leq 2$, and $0 \leq \psi^A \leq 2$. The locations of the peaks in the (ψ^M, ψ^A) space are $(1.2, 1.4), (1.2, 0.6)$, and $(-1.2, 0.6)$. In the 1D analysis for ψ^M, all the peaks would not be resolvable since they have the same absolute value of 1.2. On the other hand, in the 1D analysis for the ψ^A dimension, two of the peaks would not be resolvable due to having the same value of 0.6. However, as can be seen in Fig. 4.3, all three peaks are resolvable in the joint 2D spectrum.

So far, we have shown how the peaks in the joint spectrum in Eq. 4.6 contain information about the targets in the area. While this joint spectrum can easily be obtained by using a 2D Fourier Transform on $|c(t, d)|^2$, in practice, we would need a long antenna array to get a reasonable resolution in the f_d dimension in the 2D spectrum. Thus, we next discuss how we can efficiently estimate the required 2D spectrum, using MUSIC, even with a small Rx antenna array, and subsequently use that information to track moving targets in the area.

Remark 8 *Note that in equations 4.5 and 4.6, the static multipath does not affect the locations of the peaks of the moving targets in the spectrum. All the signal paths corresponding to the static multipath get lumped at $\psi^M = 0$ in the spectrum. Thus, by removing the temporal mean of $|c(t, d)|^2$, we can eliminate the effect of the static multipath.*

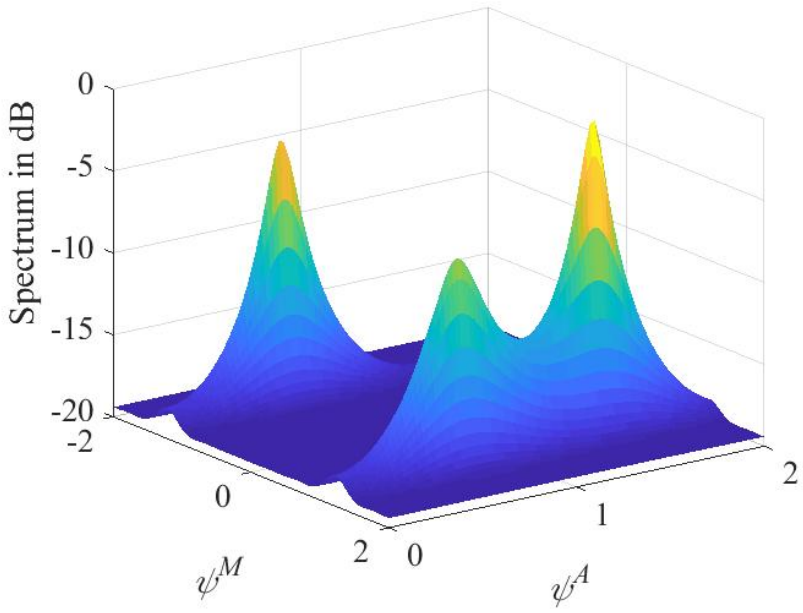

Figure 4.3: A sample 2D spectrum with 3 peaks corresponding to 3 targets in an area. The locations of the peaks in the (ψ^M, ψ^A) space are $(1.2, 1.4), (1.2, 0.6)$, and $(-1.2, 0.6)$. The peaks are resolvable only in the joint 2D spectrum, but not in the individual dimensions.

4.1.3 Multi-Dimensional Parameter Estimation - 2D MUSIC

In this section, we describe our framework to estimate the 2D spectrum from the raw spatio-temporal magnitude-squared measurements $|c(t, d)|^2$. We can then estimate the positions of the spectrum peaks, which constitute a set of (ψ^M, ψ^A) pairs that carry information about the locations and tracks of the N moving targets. Then, in Sec. 4.2, we show how this set of pairs can subsequently be used to track the N moving targets in the area.

Spectral content estimation of time or space signals is a well-explored problem in the literature, and several methods have been proposed to this end. Examples of these methods include, but are not limited to, Fourier Transform [20], MUltiple SIgnal Classification (MUSIC) [21], and Estimation of Signal Parameters via Rotational Invariance Techniques (ESPRIT) [22]. In this chapter, we propose to use 2D MUSIC spectral estimation for

the problem of Sec. 4.1.2, due to its simplicity and high-resolution capability. Another advantage of using MUSIC for the joint estimation of parameters is that the resolvability of paths in each dimension depends on the length of the arrays in both dimensions [71]. For instance, while a longer time window better resolves paths in the dimension of time, it can also help resolve paths in the dimension of space, i.e. paths that have the same ψ^M but different ψ^A. This is particularly crucial in the context of multi-target tracking, since we need to clearly distinguish the peaks in the spectrum, whereas for the case of single target tracking, one would only be concerned with the location of the single-largest peak. In our framework of multi-person tracking, we are then interested in the joint estimation of parameters (ψ^M, ψ^A) from the multi-dimensional signal model shown in equations 4.5 and 4.6. We next show how we can utilize 2D MUSIC for a magnitude-based signal model in order to estimate the spectrum and the corresponding peaks.

Consider the scenario where a receiver array contains M_A antennas with inter-antenna spacing of d_{ant}. The antennas of the array sample the received signal at a rate of $1/T_s$ samples/sec for a duration T_{win}. The number of samples in space and time are thus M_A and $M_T = \lfloor T_{\text{win}}/T_s \rfloor$, respectively. Denote by $\mathbf{C}$ the $M_A \times M_T$ matrix of magnitude-squared measurements in the spatio-temporal window:

$$\mathbf{C} = \begin{bmatrix} |c_{1,1}|^2 & |c_{1,2}|^2 & \dots & |c_{1,M_T}|^2 \\ |c_{2,1}|^2 & \ddots & & \vdots \\ \vdots & & \ddots & \vdots \\ |c_{M_A,1}|^2 & \dots & \dots & |c_{M_A,M_T}|^2 \end{bmatrix}, \tag{4.7}$$

where $c_{i,j} = c\left((i-1)d_{\text{ant}}, (j-1)T_s\right)$ is the measured 2D received signal described in Eq. 4.5.

In order to estimate the 2D spectral content of the measurements in $\mathbf{C}$, we define

the steering vector $s(\psi^M, \psi^A)$ as shown in Eq. 4.8. Then, it is straightforward to show that the vectorized form of $\mathbf{C}$ can be written in terms of the steering vectors of the paths arriving at the Rx array as follows:

$$\vec{\mathbf{C}} = \mathbf{S}\mathbf{A} + \vec{\eta}, \tag{4.9}$$

where $\vec{(.)}$ denotes the vectorized form of a matrix, $\mathbf{S}$ is an $M_A M_T \times N$ matrix whose n^{th} column is $s(\psi_n^M, \psi_n^A)$, and $A = [\alpha_1, \alpha_2, \ldots, \alpha_N]^\top$. The MUSIC algorithm calculates the eigen-decomposition of the correlation matrix R_c of the measurement vector $\vec{\mathbf{C}}$ [21],

$$R_c = E\{\vec{\mathbf{C}}\vec{\mathbf{C}}^H\} = \mathbf{S}R_A\mathbf{S}^H + R_\eta, \tag{4.10}$$

where $R_A = E\{\mathbf{A}\mathbf{A}^H\}$, $R_\eta = E\{\tilde{\eta}\tilde{\eta}^H\}$, and $E\{.\}$ is the expectation operator. It can be shown that the eigenvectors of R_c are divided into bases of a *signal subspace*, whose dimension is equal to the rank of R_A, and bases of a *noise subspace*, which is orthogonal to all the steering vectors corresponding to the N signal paths arriving at the receiver array. Therefore, we can define a pseudospectrum $P(\psi^M, \psi^A)$ as

$$P(\psi^M, \psi^A) = \frac{1}{s^H(\psi^M, \psi^A) E_N E_N^H s(\psi^M, \psi^A)}, \tag{4.11}$$

$$s\left(\psi^M, \psi^A\right) = \Big[\overbrace{1,\, e^{-\frac{j2\pi}{\lambda}\psi^A d_{\text{ant}}},\, \ldots,\, e^{-\frac{j2\pi}{\lambda}\psi^A (M_A-1) d_{\text{ant}}}}^{\text{array measurements at } t=0},$$
$$\overbrace{e^{-\frac{j2\pi}{\lambda}\psi^M T_s},\, e^{-\frac{j2\pi}{\lambda}(\psi^M T_s + \psi^A d_{\text{ant}})},\, \ldots,\, e^{-\frac{j2\pi}{\lambda}(\psi^M T_s + \psi^A (M_A-1) d_{\text{ant}})}}^{\text{array measurements at } t=T_s}, \ldots,$$
$$\underbrace{e^{-\frac{j2\pi}{\lambda}\psi^M (M_T-1) T_s},\, e^{-\frac{j2\pi}{\lambda}(\psi^M (M_T-1) T_s + \psi^A d_{\text{ant}})},\, \ldots,\, e^{-\frac{j2\pi}{\lambda}(\psi^M (M_T-1) T_s + \psi^A (M_A-1) d_{\text{ant}})}}_{\text{array measurements at } t=(M_T-1)T_s}\Big]^\top \tag{4.8}$$

where E_N is a matrix whose columns constitute the bases for the noise subspace. $P(\psi^M, \psi^A)$ peaks at the locations of $(\psi_n^M, \psi_n^A), n = 1, \ldots, N$, since the steering vectors corresponding to these locations are orthogonal to the noise subspace E_N. Hence, extracting the locations of the peaks of $P(\psi^M, \psi^A)$ provides the required (ψ_n^M, ψ_n^A) pairs needed for tracking the N targets.

A critical assumption in the MUSIC algorithm is that the matrix R_A is full rank, i.e., all the different N signals are uncorrelated. Such an assumption is not valid in many practical scenarios where scattering and multipath propagation are involved. Then, in order to uncorrelate the signals, spatial smoothing is a technique commonly used in the literature [72]. In spatial smoothing, the correlation matrix R_c is calculated by averaging the correlation matrices of different subsets of the antenna array, given that each of the subsets is a set of contiguous antennas. Then, to address the correlation of signals in our 2D framework, we extend spatial smoothing to *spatio-temporal smoothing MUSIC* for our scenario. We divide the matrix $\mathbf{C}$ into overlapping sub-matrices $\mathbf{C}^{\text{sub}}$ of size $M_A^{\text{sub}} \times M_T^{\text{sub}}$ each. The correlation matrix R_c is then calculated as the average of the correlation matrices R_c^{sub} of the sub-matrices $\mathbf{C}^{\text{sub}}$. Similar spatio-frequential smoothing techniques have been proposed for the JADE MUSIC problem in the literature [73].

After computing the pseudospectrum $P(\psi^M, \psi^A)$, we next find the locations of the peaks of the pseudospectrum as

$$\mathbf{\Psi} = \left\{ \psi_j = (\psi_j^M, \psi_j^A), j = 1, \ldots, J \right\},$$

where J is the number of detected peaks in the pseudospectrum. As we shall see next, this information is then used to estimate the tracks of the N targets.

4.2 Multiple Target Tracking

In this section, we show how we can use the extracted information from the 2D spectrum to track multiple targets. In order to extract the information about the targets' locations and headings at time t, we apply the aforementioned 2D spatio-temporal smoothing MUSIC algorithm on the data $|c(t,d)|^2$ in a time window of duration T_{win} starting at time t, to extract the set of peaks $\mathbf{\Psi}_t$ at time t. We first list the problems that arise when relying directly on $\mathbf{\Psi}_t$ (with cardinality J_t) for tracking the N targets. Then, we present our solutions to overcome these problems and reconstruct the targets' tracks using $\mathbf{\Psi}_t$.

Two main problems arise when using $\mathbf{\Psi}_t$ for tracking:

- **Ambiguity:** As previously mentioned, while the 2D joint parameter estimation resolves a few ambiguities that exist when estimating each parameter individually, the pair of (ψ^M, ψ^A) does not give sufficient information about the location of the target that resulted in a particular measurement. For instance, Fig. 4.4 shows an example of two different valid solutions to a target's location and heading for a measurement of $\psi^M = 0.187$ and $\psi^A = 0.707$, thus showing the ambiguity prevalent in each (ψ^M, ψ^A) measurement.

- **Association:** At each time instant, we extract a set of J_t measurements from the 2D spectrum. However, we lack the knowledge of the subset of these J_t measurements that are actual detections from the moving targets, and the complimentary subset of false alarms. Furthermore, for the subset of actual detections, we would need an association profile of which detections correspond to which targets. Such an issue does not arise and is thus not addressed in a single target tracking framework. Thus, the methods proposed for single-target tracking cannot be directly utilized for multi-target tracking in this chapter.

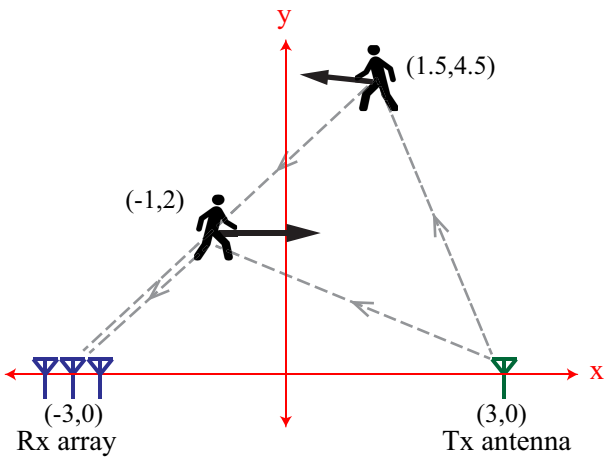

Figure 4.4: Example of ambiguity resulting from the measurement of $\psi = (0.187, 0.707)$. Two targets result in the same measurement: one at location (-1,2) with heading of 0°, the other at location (1.5,4.5) with heading of 173°. Both targets have a speed of 1 m/s.

In order to overcome these problems, we exploit the fact that the targets are moving and model the measurements associated with the targets' motion as a nonlinear dynamical system [70]. We further utilize a Particle Filter (PF) with a Joint Probabilistic Data Association Filter (JPDAF) to solve this dynamical system and obtain an estimate for the track of each target, as we shall see next.

Consider the scenario where a Tx is located at (x_T, y_T) and a Rx array is centered at (x_R, y_R) such that its array axis is parallel to the x-axis, as shown in Fig. 4.2. We define the state of the n^{th} target at time t as a 4-dimensional vector $\mathbf{x}_t^n$ that carries information about the target's location, heading, and speed. More specifically, $\mathbf{x}_t^n = \big[x_n(t), y_n(t), \theta_n(t), v_n(t)\big]^\top$, where $x_n(t), y_n(t)$ define the location of the n^{th} target at time t, $\theta_n(t)$ is its direction of motion, measured with respect to the x-axis, and $v_n(t)$ is its speed. Furthermore, we define a measurement process $\psi_n(t)$ as the pair $(\psi_n^M(t), \psi_n^A(t))$, which

can be related to the target's state as follows:

$$\begin{aligned}\psi_n^M(t) = v_n(t) &\left(\frac{(x_R - x_n(t))\cos(\theta_n(t)) + (y_R - y_n(t))\sin(\theta_n(t))}{\sqrt{(x_R - x_n(t))^2 + (y_R - y_n(t))^2}}\right) \\ + v_n(t) &\left(\frac{(x_T - x_n(t))\cos(\theta_n(t)) + (y_T - y_n(t))\sin(\theta_n(t))}{\sqrt{(x_T - x_n(t))^2 + (y_T - y_n(t))^2}}\right) \\ + \eta_M(t),&\end{aligned} \tag{4.12}$$

and

$$\psi_n^A(t) = 1 - \left(\frac{x_n(t) - x_R}{\sqrt{(x_R - x_n(t))^2 + (y_R - y_n(t))^2}}\right) + \eta_A(t), \tag{4.13}$$

where η_M and η_A are measurement noise processes with variances $\sigma^2_{\eta_M}$ and $\sigma^2_{\eta_A}$, respectively. On the other hand, we assume a simple motion dynamics model for the targets, in which a target maintains the same direction of motion with probability P_c, and occasionally changes that direction with probability $1 - P_c$. More specifically, we assume the state of the n^{th} target evolves with time according to the model $\mathbf{x}^n_{t+1} = g_n(\mathbf{x}^n_t)$ as follows:

$$\begin{aligned} x_n(t+1) &= x_n(t) + v_n(t)\ \cos(\theta_n(t)) + \eta_{x_n}(t+1), \\ y_n(t+1) &= y_n(t) + v_n(t)\ \sin(\theta_n(t)) + \eta_{y_n}(t+1), \\ \theta_n(t+1) &= \eta_{\theta_n}(t+1) + \begin{cases} \theta_n(t) & \text{w.p. } P_c \\ \sim \mathcal{U}(0, 2\pi) & \text{w.p. } 1 - P_c \end{cases}, \\ v_n(t+1) &= v_n(t) + \eta_{v_n}(t+1), \end{aligned} \tag{4.14}$$

where $\eta_{x_n}, \eta_{y_n}, \eta_{\theta_n}$, and η_{v_n} are all dynamics noise processes with variances $\sigma^2_{\eta_{x_n}}, \sigma^2_{\eta_{y_n}}, \sigma^2_{\eta_{\theta_n}}$, and $\sigma^2_{\eta_{v_n}}$, respectively, and $\mathcal{U}(0, 2\pi)$ is the uniform distribution in the interval $[0, 2\pi)$.

For the estimation of the state of the n^{th} target $\mathbf{x}^n_t$ at time t, we propose to compute the filtering Probability Density Function (PDF) $p(\mathbf{x}^n_t | \mathbf{\Psi}_{1:t})$ of the n^{th} target's state at

time t given all the measurements up to time t. Then, we use the mean of this PDF as the estimate of the target's state $\hat{\mathbf{x}}_t^n = E\{\mathbf{x}_t^n | \mathbf{\Psi}_{1:t}\}$. To this end, we propose to use a Particle Filter (PF) for the computation of the filtering PDF of the n^{th} target [74]. The underlying principle of PFs is that they approximate any probability distribution using samples (or particles) drawn from that distribution. Such a representation is favorable in many scenarios, especially when nonlinear random variable transformations are involved. The steps of the PFs used in our problem are summarized in Algorithm 2. The PF for the n^{th} target starts by drawing a total of I samples/particles $\mathbf{x}_1^{[i,n]}, i = 1, \ldots, I$ from an initial distribution $\chi_1^n(\mathbf{x}_1^n)$, which can depend on any prior information we have about the initial state of the n^{th} target. Then, these particles are given *importance weights* $w_1^{[i,n]}$ which represent how well they fit the current set of measurements $\mathbf{\Psi_1}$ (step 4 in Algorithm 2). However, the aforementioned association problem hinders the completion of this step, since the PF lacks the knowledge of which of the measurements in $\mathbf{\Psi_1}$ was generated by the n^{th} target. To overcome this, we propose to utilize a Joint Probabilistic Data Association Filter (JPDAF) to calculate the importance weights [75]. We will discuss the details of the JPDAF later in this section. After the importance weights are calculated, a *resampling* step (step 9) is performed in order to neglect the low-weight particles and retain particles that have a high probability of producing the current measurement set. The resampled particles then evolve according to the motion model in Eq. 4.14 and the whole process is repeated for consecutive time instants. More details on PFs can be found in [74].

The JPDAF, on the other hand, deals with the problem of associating measurements to targets. Consider the set of measurements $\mathbf{\Psi}_t = \{\psi_j, j = 1, \ldots, J_t\}$ measured at time t. Some of these measurements can be false alarms that are not associated with any target, arising due to the modeling errors. We denote the probability of such false alarms as P_{FA}. Furthermore, some target measurements can be missing from the set $\mathbf{\Psi}_t$,

for instance, due to blockage by other targets. We denote the probability of a target miss as $1 - P_D$, where P_D is the detection probability. The underlying principle of the JPDAF is then to calculate the probabilities of all possible *association profiles* given the current set of measurements and particles [75]. An association profile ω matches each target to one of the J_t measurements. In other words, an association profile ω is a set of N pairs (k, l) where $l = 1, 2, \ldots, N$, $k \in \{0, 1, \ldots, J_t\}$, and a pair (k, l) represents assigning the measurement ψ_k to the l^{th} target.[1] Afterwards, the probability of the n^{th} target generating the measurement ψ_j can be computed by summing the probabilities of all the association profiles which assign the measurement ψ_j to the n^{th} target. We denote the set of all such association profiles by Ω_{jn}, i.e., $\Omega_{jn} = \{\omega; (j, n) \in \omega\}$. The details of the JPDAF calculation of the importance weights are shown in Algorithm 3.

Remark 9 *Note that in the case of tracking one person, we still utilize the JPDAF in the calculation of the particle weights in the PF. In such a case, the main function of the JPDAF is to distinguish false alarm measurements from the actual measurement corresponding to the target's motion.*

4.3 Experimental Results

In this section, we present the experimental results of our proposed magnitude-based framework for multi-person tracking, using WiFi CSI magnitude measurements from one side of the area. We first discuss our experimental setup and the practical considerations that arise in these experiments. We then show the performance of our tracking framework through extensive experiments (40 in total) carried out in six different environments, with

[1]Note that the pair $(k = 0, l)$ represents the case of no measurement associated to the l^{th} target, which can happen with probability $(1 - P_D)$, where P_D is the detection probability.

Algorithm 2 Particle Filter for Motion Tracking

Input: Total tracking time T, Number of particles I, Number of moving people N, Measurements $\mathbf{\Psi}_{1:T}$

Output: Estimate of the target states $\hat{\mathbf{x}}_{1:T}^n, n = 1, 2, \ldots, N$

Initialize $t = 1$
for $1 \leq n \leq N$ **do**
  Sample $\mathbf{x}_1^{[i,n]} \sim \chi_1^n(\mathbf{x}_1^n)$ for $i = 1, 2, \ldots, I$
end for
Compute the importance weights $\tilde{w}_1^{[i,n]}$ using the JPDAF in Algorithm 3, and normalize $w_1^{[i,n]} = \frac{\tilde{w}_1^{[i,n]}}{\sum_{i=1}^I \tilde{\mathbf{w}}_1^{[i,n]}}$
Estimate the initial state of the n^{th} target as $\hat{\mathbf{x}}_1^n = E\{\mathbf{x}_1^n | \mathbf{\Psi}_1\} = \sum_{i=1}^I w_1^{[i,n]} \mathbf{x}_1^{[i,n]}$
for $2 \leq t \leq T$ **do**
  for $1 \leq n \leq N$ **do**
    Sample $\tilde{\mathbf{x}}_{t-1}^{[i,n]}$, for $i = 1, \ldots, I$, from the distribution defined by $p(\tilde{\mathbf{x}}_{t-1}^n = \mathbf{x}_{t-1}^{[i,n]}) = w_{t-1}^{[i,n]}$
    Sample $\mathbf{x}_t^{[i,n]} \sim g_n(\tilde{\mathbf{x}}_{t-1}^{[i,n]})$
  end for
  Compute the importance weights $\tilde{w}_t^{[i,n]}$ using the JPDAF in Algorithm 3, and normalize $w_t^{[i,n]} = \frac{\tilde{w}_t^{[i,n]}}{\sum_{i=1}^I \tilde{\mathbf{w}}_t^{[i,n]}}$
  Estimate the state of the n^{th} target as $\hat{\mathbf{x}}_t^n = \sum_{i=1}^I w_t^{[i,n]} \mathbf{x}_t^{[i,n]}$
end for

Algorithm 3 Joint Probabilistic Data Association Filter for Particle Weight Calculation

Input: All current particles $\mathbf{x}^{[i,n]}$, current measurement set $\mathbf{\Psi}$, P_D, P_{FA}
Output: The particles' importance weights $\tilde{w}^{[i,n]}$

1: Calculate the number of current measurements $J = |\mathbf{\Psi}|$
2: Calculate $\gamma_j^{[i,n]} = p(\psi_j|\mathbf{x}^{[i,n]})$, which denotes the probability of the measurement ψ_j being generated by the n^{th} target having a state $\mathbf{x}^{[i,n]}$, according to Eq. 4.12 and Eq. 4.13
3: Generate all possible association profiles ω, where $\omega = \{(k,l); k \in \{0,1,\ldots,J\}, l = \{1,\ldots,N\}\}$, and (k,l) is a pair assigning the measurement ψ_k to the l^{th} target
4: Calculate the probability of each association profile as

$$p(\omega|\mathbf{\Psi}) = P_{FA}^{J-|\omega|} P_D^{|\omega|-|\omega_o|} (1-P_D)^{|\omega_o|} \prod_{\substack{(k,l)\in\omega \\ k\neq 0}} \frac{1}{I} \sum_{i=1}^{I} p(\psi_k|\mathbf{x}^{[i,l]}) \tag{4.15}$$

where ω_o is a subset of ω with targets not being assigned to any of the measurements, i.e., $\omega_o = \{(k,l); (k,l) \in \omega, k = 0\}$
5: Calculate the probability that a measurement ψ_j is caused by the n^{th} target β_{jn} by summing over all association profiles making such an assignment,

$$\beta_{jn} = \sum_{\omega\in\Omega_{jn}} p(\omega|\mathbf{\Psi}) \tag{4.16}$$

6: Calculate the importance weights

$$\tilde{w}^{[i,n]} = \frac{1}{\sum_{j=0}^{J} \beta_{jn}} \left(\beta_{0n} + \sum_{j=1}^{J} \beta_{jn} p(\psi_j|\mathbf{x}^{[i,n]}) \right) \tag{4.17}$$

various levels of clutter. Finally, we discuss the impact of several experimental parameters on the results, and compare with the state-of-the-art tracking algorithms.

4.3.1 Experimental Setup

For the data collection process, we use laptops with Intel 5300 WiFi NICs for both transmission and reception. For the Tx, a tripod-mounted antenna is connected to one port of an Intel card that broadcasts WiFi packets on channel 36 in the 5 GHz band. We then use the WiFi cards of three laptops as receivers, with each WiFi card providing two antenna ports. In other words, we use WiFi NICs of three laptops and connect two WiFi ports of each laptop to two antennas mounted on a tripod, as shown in Fig. 4.5.[2] The 3 Rx WiFi NICs log the packets transmitted on the WiFi channel. We then process the measured data offline using Csitool [66] to extract the CSI measurements and track the moving subjects. As previously mentioned, since we rely only on the magnitude of the CSI measurements, the Rx NICs do not need any phase synchronization. Thus, our proposed framework is also flexible to facilitate further addition of antennas to the array as needed, without any additional calibrations. We next discuss some practical considerations that arise in our experiments.

- **Spatio-temporal sampling rates:** As shown in Sec. 4.1, the reflected signal from the n^{th} person results in a peak in the 2D spectrum at $(\psi_n^M, \psi_n^A) = \big(v_n(\cos\phi_n^R + \cos\phi_n^T), 1 - \cos\phi_n\big)$. Hence, the maximum frequency content for f_t and f_d are $\frac{2v_{\max}}{\lambda}$ and $2/\lambda$ respectively, where $v_{\max}$ is the maximum possible human walking speed. Then, according to the Nyquist sampling theorem, the sampling rates for the 2D received signal in time and

[2]Note that while each Intel 5300 NIC has 3 antenna ports available, we observed that the signal on port 3, which is located between port 1 and 2 on the NIC, is sometimes corrupted due to crosstalk (as is reported by other users [76]). Hence, we use only ports 1 and 2 on each WiFi Rx. In the future, if one could obtain clean measurements on all the three ports, then one would only need 2 Rx laptops with Intel 5300 NICs to achieve the results of this chapter.

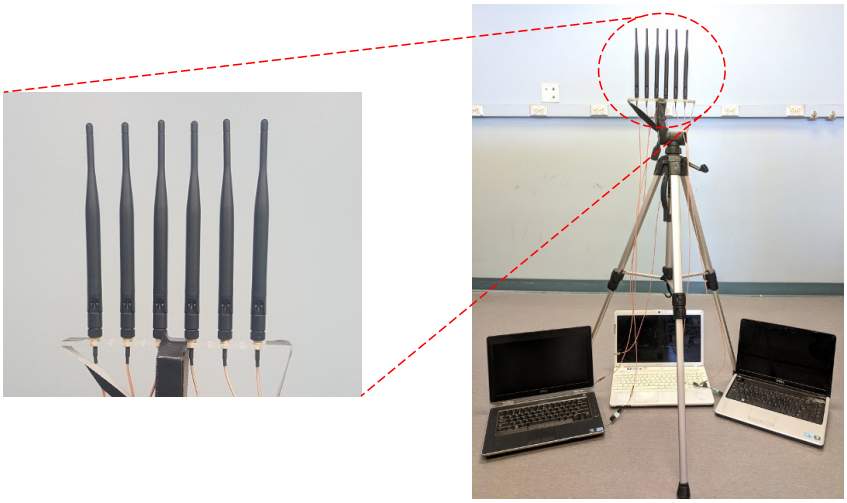

Figure 4.5: Receiver setup: WiFi cards of 3 laptops are used, resulting in 6 total antennas that we space $\lambda/2$ apart on a tripod as shown.

space should be greater than $\frac{4v_{\max}}{\lambda}$ and $4/\lambda$ respectively.

In the temporal dimension, we set the sampling rate to 1000 packets/sec, which is much higher than the required sampling rate of 139 packets/sec (assuming a $v_{\max}$ of 2 m/s). However, for the spatial dimension, fixing the antennas $\lambda/4$ meters (1.45 cm) apart is difficult due to the relatively large physical dimensions of the antennas. Hence, we place the antennas $\lambda/2$ apart, which leads to aliasing in the f_d dimension of the spectrum. In order to overcome such aliasing effect, we propose to place the Rx array in a corner of the tracking area, so that the ϕ_ns for all the targets are less than 90°. Hence, the maximum possible value of f_d in this case is $1/\lambda$, and such a $\lambda/2$-spaced array configuration does not suffer from aliasing problems.

- **Data clean-up process:** Raw CSI measurements on commodity WiFi cards can suffer from noise due to the internal state transitions in the Tx and Rx WiFi NICs [77]. To reduce the noise in the raw CSI measurements, we utilize two denoising schemes.

  1. Principal Component Analysis (PCA): The Intel 5300 NIC reports CSI measurements on 30 different subcarriers. It has been shown in [77] that the changes in

CSI due to human movements on different subcarriers are correlated. Hence, the reflected signal can be separated from noise by performing PCA on the data from the 30 subcarriers.

2. Wavelet denoising: Discrete Wavelet Transform (DWT)-based noise suppression techniques have been shown to outperform traditional denoising schemes such as band-pass filters [78]. Hence, we apply wavelet denoising on the PCA-denoised signal in order to suppress residual noise.

- **2D MUSIC parameters:** We choose the array parameters of the 2D MUSIC algorithm described in Sec. 4.1 as follows: $T_{\text{win}} = 0.5s$, $T_{\text{win}}^{\text{sub}} = 0.25s$, $M_A = 6$, and $M_A^{\text{sub}} = 5$. Note that a small T_{win} implies that people can take any track in our framework and are not limited to walk on straight lines. In order to detect peaks in the pseudospectrum, we define a peak as a point in the pseudospectrum whose value is greater than its neighbors, and greater than an empirically predefined threshold $p_{\text{th}} = 0.6 \times P_{\text{min, dB}}$, where $P_{\text{min, dB}}$ is the minimum value in the normalized pseudospectrum in dB (with the maximum value being 0 dB in the normalized pseudospectrum).

- **Particle filter parameters:** In order to set the parameters of the PF, we collect a few prior measurements (not in the same area of the experiment) and estimate the values for the noise variances and probabilities of detection and false alarms. These parameters are then used in all the different experiments in different areas. The parameters are then set as follows: $\sigma_{\eta_M} = 0.1$, $\sigma_{\eta_A} = 0.07$, $\sigma_{\eta_{x_n}} = \sigma_{\eta_{y_n}} = 1$ cm, $\sigma_{\eta_{\theta_n}} = 1^\circ$, $\sigma_{\eta_{v_n}} = 2.5 \times 10^{-3}$, $P_c = 0.9$, $P_D = 0.85$, $P_{FA} = 0.25$ for outdoor areas, $P_{FA} = 0.35$ for indoor areas, and $I = 5000$. Note that the probability of false alarm is higher in indoor environments due to the stronger multipath.

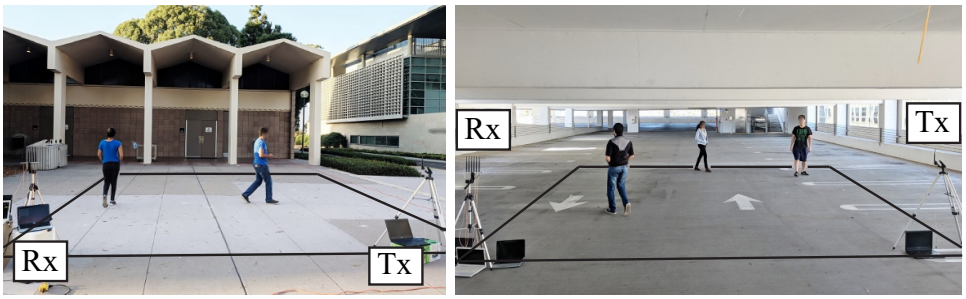

Figure 4.6: Tracking experimental setup in outdoor areas in (a) an open area and (b) a closed parking lot. The boundaries of the workspace are marked with a solid black line.

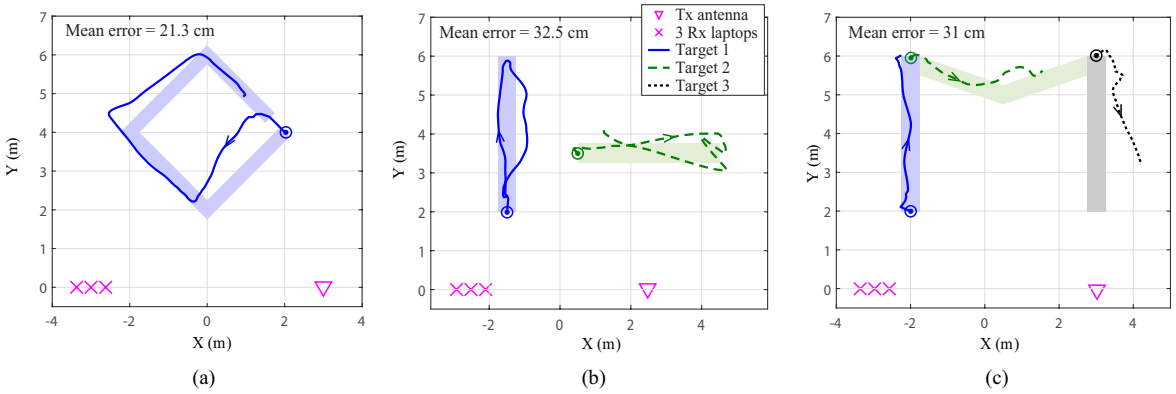

Figure 4.7: Sample multi-person tracking results in the outdoor areas shown in Fig. 4.6 – (a) One person walking along a diamond-shaped route in the area of Fig. 4.6b, (b) two persons walking back and forth on perpendicular straight lines in the area of Fig. 4.6a, and (c) three persons walking on different parts of an M-shaped route in the area of Fig. 4.6b. The light background patches represent the actual tracks, while the $\odot$ symbols represent their starting points.

4.3.2 Tracking Results

In this section, we show how our proposed framework can track multiple moving people in an area, based on only the WiFi CSI magnitude measurements of 3 laptops that are located on one side of the area. We carry out tracking experiments in six different environments, with up to three people walking simultaneously in the area. We categorize the areas into outdoor and indoor scenarios. Fig. 4.6 shows the outdoor areas, where Fig. 4.6 (a) is an open area with minimal clutter, and Fig. 4.6 (b) is a parking lot which has considerable multipath due to the walls and the low ceiling beams. The top row of Fig. 4.8 then shows some of the indoor areas, which are more challenging than the outdoor areas due to higher extent of clutter (e.g. furniture, walls) and the resulting multipath. In all experiments, we ask the subjects to walk on predefined tracks defined by floor markers in a 7 m $\times$ 7 m area, and time-stamp their motion at the markers in order to obtain the ground-truth locations of the subjects. Furthermore, since we cannot know the exact point of reflection on the person's body at which the signal bounces off at each time instant, we approximate a person as a cylindrical object of radius 25 cm. We then calculate the tracking error, at any time instant, as the minimum distance between the estimated location and the surface of that cylinder. Such a method of error calculation has previously been adopted in similar contexts in the literature [70, 39].

Outdoor Tracking: In this section, we show our tracking results for the outdoor areas shown in Fig. 4.6. The first location, shown in Fig. 4.6 (a), is a relatively open area with little to no clutter, resulting in minimal multipath. On the other hand, the second location, shown in Fig. 4.6 (b), is a parking structure where the walls and ceiling beams generate considerable multipath. In both cases, the Tx antenna and the 3 Rx laptops are fixed to the corners on one side of the 7 m $\times$ 7 m area of interest, as shown in Fig. 4.6. Overall, we ran 17 experiments in these 2 areas of Fig. 4.6, with 1, 2, and 3 people on

several different days, walking in different paths. In all the experiments, we initialize the PF with particles that are uniformly distributed in a 3 m $\times$ 3 m square around the locations where the targets start their motion. Fig. 4.7 then shows a few sample results of our tracking framework for these two areas. It can be seen that our proposed framework estimates the track of the people with a high accuracy in all the cases. Overall, we achieve a mean tracking error of 38 cm (median of 29 cm) when considering all the 17 experiments.

Indoor Tracking: In this section, we show our tracking results for the indoor areas of conference rooms, a classroom, and a lounge area, shown in the top row of Fig. 4.8. In all the locations, the walls, ceiling, and furniture constitute clutter which makes the effect of multipath more significant. While we can remove the effect of the static multipath by subtracting the temporal mean of the received signal as described in Remark 8, higher order reflections involving both a moving target and a static object, although weaker, still affect the received signal, and consequently the 2D spectrum. This results in a higher number of false alarms as mentioned in Sec. 4.3.1.

Similar to the outdoor areas, we fix the Tx antenna and the 3 Rx laptops to the corners on one side of the area of interest. We also initialize the PF with particles that are uniformly distributed in a 3 m $\times$ 3 m square around the locations where the targets start their path. Overall, we ran 23 experiments in 4 different areas (the three areas shown in Fig. 4.8 and one additional conference room) with 1, 2, and 3 people on several different days, walking in different paths. The bottom row of Fig. 4.8 then shows a few sample tracking results for these locations. It can be seen that our proposed magnitude-based framework achieves a good accuracy of tracking multiple people in indoor environments as well, with an overall mean tracking error of 55 cm (median of 39 cm) across all the 23 different experiments. It should be noted that we do not utilize any information about the clutter (e.g., the furniture) in the track estimation framework. If the information

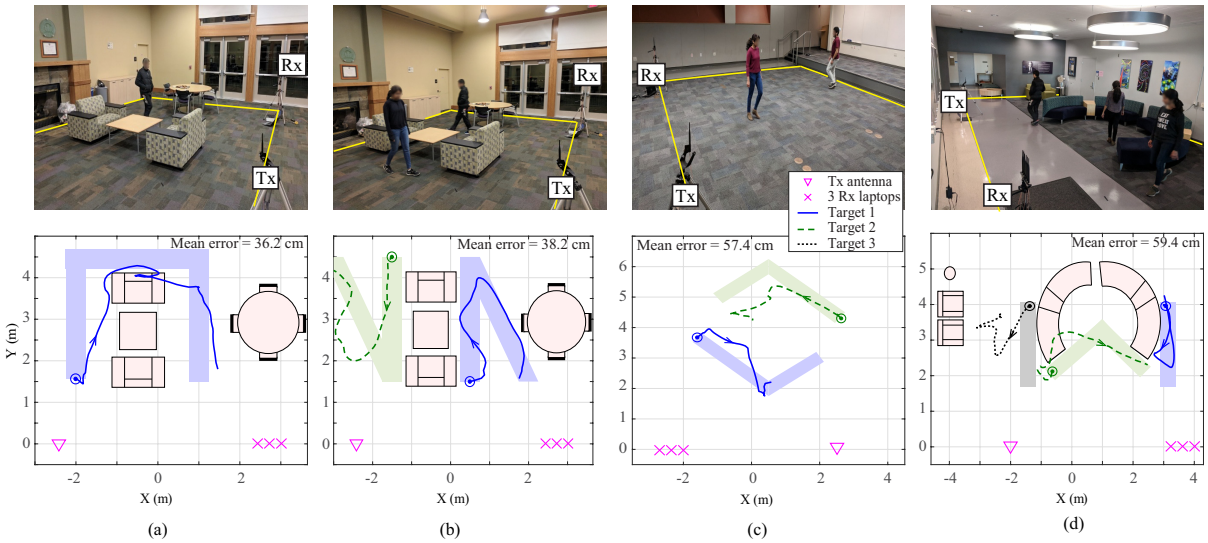

Figure 4.8: (Bottom) Sample multi-person tracking results in (top) corresponding indoor areas with various degrees of clutter – (a) One person walking along a U-shaped route in an area including tables, chairs, and futons, (b) two persons walking along two V-shaped routes in the same area, (c) two persons walking along two check-mark-shaped routes in a classroom, and (d) three persons walking on different lines in an area containing multiple chairs, sofas, and light fixtures, where the targets 1 and 3 walk in a back-and-forth fashion along the marked route. The yellow lines in the area pictures represent the tracking area boundary. The light background patches on the figures represent the actual tracks, while the $\odot$ symbols represent their starting points.

about the locations of the furniture was known apriori, it can be used, for example, to prohibit any particles in the PF from appearing on their locations, thereby improving the track estimation accuracy.

4.3.3 Discussion

In this section, we investigate the impact of some of the experimental parameters on the performance of our proposed tracking framework, and compare the performance of our proposed framework with the state-of-the-art.

Effect of environment: As previously mentioned, indoor environments are more challenging than outdoor ones because of the stronger multipath resulting from the clut-

Paper	Num. of targets	Magnitude only	Number of devices used	One side of area	Tracking error
Widar2.0 [79]	1	✗	2 WiFi NICs	✓	75 cm
IndoTrack [39]	1	✗	3 WiFi NICs	✗	35 cm
DynMusic [40]	1	✗	4 WiFi NICs	✗	36–62 cm
[70]	1	✓	4 WiFi NICs	✗	31 cm
WiTrack2.0 [38]	4	✗	1 FMCW radar	✓	10–17 cm
[37]	2	✗	1 UWB radar	✓	0.6 cm*
[36]	4	✓	32 ZigBee nodes	✗	26–45 cm
[80]	3	✓	24 ZigBee nodes	✗	31–91 cm
SCPL [81]	4	✓	22 CC1100 nodes†	✗	108 cm
Our approach	**3**	✓	**4 WiFi NICs**	✓	**47 cm**

* when compared to a colocated LiDAR system

† radio transcievers operating in the 909.1 MHz unlicensed band

Table 4.1: Comparison with the state-of-the-art in target tracking using RF signals.

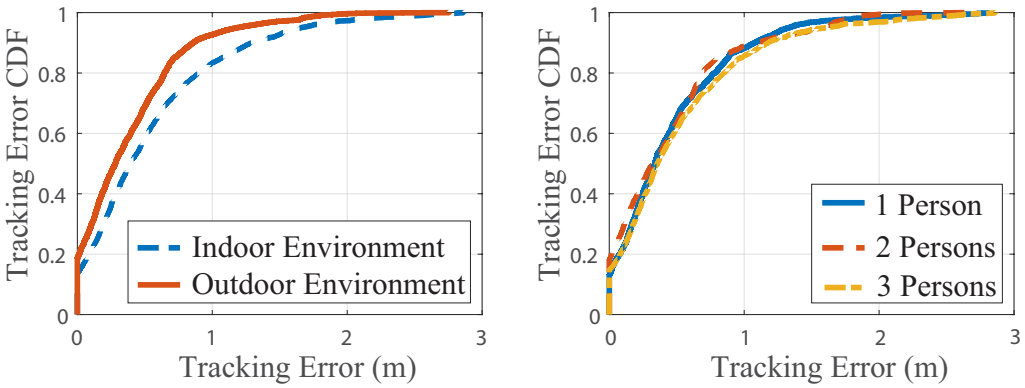

Figure 4.9: Tracking error analysis over 40 different experiments in 6 different areas (five area pictures shown in this chapter and one additional indoor area not shown) and various tracking routes. (a) CDF of tracking errors in outdoor vs indoor environments from tracking 1, 2, and 3 people walking on different tracks, on different days. Performance is better in outdoor environments due to less multipath, as expected. (b) CDF of tracking errors for different number of people. Comparable performance is seen for all cases of 1, 2, or 3 people.

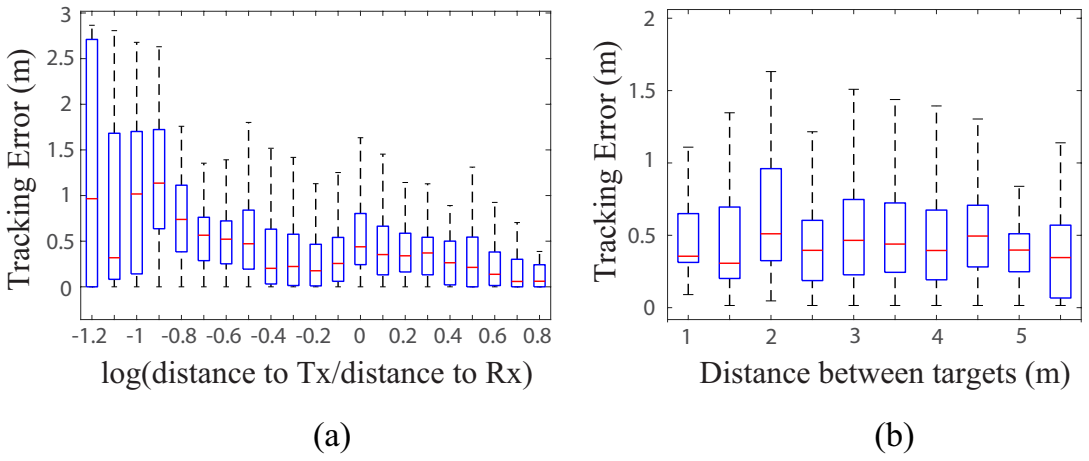

Figure 4.10: Tracking error analysis over 40 different experiments in 6 different areas (five area pictures shown in this chapter and one additional indoor area not shown) and various tracking routes. (a) Box plot of the distribution of point-wise tracking error over all the experiments as a function of the logarithm of the ratio between the distance of the target to the Tx and its distance to Rx. Targets closer to Rx tend to have lower errors. (b) Box plot of the distribution of point-wise tracking error as a function of the inter-target distance showing little to no effect.

ter. The noisier spectrum and higher false alarm probability affect the performance of the tracking framework and increase the tracking error. To quantify this effect, Fig. 4.9 (a) shows the Cumulative Distribution Function (CDF) of the tracking error for both indoor and outdoor environments. As can be seen, the performance in indoor environments is slightly worse compared to outdoor ones, as expected. More specifically, the indoor environments have an overall mean tracking error of 55 cm, in comparison to 38 cm for outdoor areas.

Effect of the number of people: We also test the performance of our tracking framework by varying the number of people being tracked. Fig. 4.9 (b) shows the CDF curves of the tracking error for different number of people. It can be seen that the performance is comparable in all the cases of tracking 1 to 3 people. While tracking multiple people, there is a higher chance that a measurement corresponding to one of the persons disappears momentarily, if that person is blocked by other people. However, the

JPDAF (with an appropriate P_D setting) accounts for that missing detection and keeps track of the blocked target, thereby preserving the accuracy of the framework even in the presence of blocking effects.

Effect of the closeness to Tx or Rx: Fig. 4.10 (a) shows the box-plot distribution of the point-wise tracking error of our framework over all the tracks in all the 40 experiments, as a function of the logarithm of the ratio between the distance of the target to the Tx and its distance to the Rx. Negative values to the left side of the figure correspond to targets that are closer to the Tx than the Rx, while positive values to the right correspond to targets that are closer to the Rx. It can be seen that the error tends to be lower when the target is closer to the Rx, since the reflections off of the target's body are more likely to reach the Rx array. On the other hand, targets farther away from the Rx would be scattering in different directions and the reflections are less likely to reach the Rx array. Hence, if the antenna dimensions of the Rx permit placing them $\lambda/4$ apart, it is recommended to place the Rx array in the midpoint of the link side of the tracking area (see Sec. 4.3.1).

Effect of the distance between targets: Fig. 4.10 (b) shows the box-plot distribution of the point-wise tracking error of our framework as a function the distance between the targets in all the multi-target tracking experiments. It can be seen that such a distance has little to no effect on the tracking performance of our framework. This is primarily because a small distance between two targets does not imply that they are indistinguishable in the measurement domain (ψ_M, ψ_A), since two close targets with different moving directions have different ψ_Ms.

Comparison to the state-of-the-art: Table 4.1 shows the tracking accuracy of the state-of-the-art as well as our framework. It can be seen that our framework achieves a decimeter-level tracking accuracy that is comparable to the state-of-the-art, for both single and multiple target tracking, but without requiring any extra bandwidth or sev-

eral transceivers that were previously required for multiple target tracking, or phase measurements that were previously required for single target tracking.

Chapter 5

Conclusions

In this dissertation, we showed how we can use off-the-shelf devices and their corresponding received signal magnitude measurements to achieve various RF sensing tasks. We also showed the possibilities created at the intersection of RF sensing and robotics, and how we can utilize the mobitiy of unmanned vehicles to sense various attributes of our environment. More specifically, we first showed how we can achieve 3D through-wall imaging of completely unknown areas using UAVs and WiFi RSSI measurements. In the second part, we proposed and validated our new approach to the angle-of-arrival estimation problem using only signal magnitude measurements at an antenna array. We discussed the various ambiguities that arise in such a formulation and showed ways to address them. We then extended the magnitude-based AoA framework to achieve channel prediction at unvisited locations by predicting the makeup of the corresponding rays. Finally, we discussed our proposed approach to enable multi-target tracking using WiFi magnitude measurements, without the need for the targets to carry any device.

We next summarize our results in each of these areas.

5.1 3D Through-Wall Imaging

In Chapter 2, we have considered the problem of 3D through-wall imaging with UAVs, using only WiFi RSSI measurements, and proposed a new framework for reconstructing the 3D image of an unknown area. We have utilized an LOS-based measurement model for the received signal power, and proposed an approach based on sparse signal processing, loopy belief propagation, and Markov random field modeling for solving the 3D imaging problem. Furthermore, we have shown an efficient aerial route design approach for autonomous antenna positioning and wireless measurement collection with UAVs. We then described our developed extensive experimental testbed for 3D imaging with UAVs and WiFi RSSI. Finally, we showed our experimental results for high-quality 3D through-wall imaging of two unknown areas, based on only a small number of WiFi RSSI measurements (3.84% and 3.6%).

5.2 Magnitude-Based AoA Estimation and Channel Prediction

In Chapter 3, we have considered the problem of estimating the angle of arrival (AoA) of all signal paths arriving at a receiver array using only the received signal magnitude measurements. We have proposed a computationally-efficient framework, based on the auto-correlation of the magnitude measurements, to solve the AoA estimation problem. We then discussed the ambiguities arising in a magnitude-only AoA estimation problem and proposed a method to eliminate the ambiguity. We have experimentally validated our AoA estimation framework in closed and open areas, and showed a mean absolute error of 2.56° for angular localization of active and passive objects.

We then extended the magnitude-based AoA estimation framework to the problem

of channel prediction. Here, we proposed a new robotic framework that estimates the fundamental parameters of the rays in an area, in order to predict the makeup of the rays and subsequently predict the channel quality and channel variations at unvisited locations. We then experimentally validated our proposed approach through experiments conducted using ground robots.

5.3 Multi-Person Passive Tracking

In Chapter 4, we have considered the problem of passively tracking multiple persons using only WiFi magnitude measurements on a small number of WiFi receivers, located on one side of the tracking area. We have proposed a framework based on the joint estimation of multi-dimensional parameters of the received WiFi signal. More specifically, our framework jointly estimates the angles-of-arrival from the targets to the receiver array, as well as the parameters of the arrays induced by the targets' motion. Furthermore, we have utilized Particle Filters and Joint Probabilistic Data Association Filter (JPDAF) in order to associate the estimated parameters to the targets in the area, and consequently reconstruct the tracks of these targets. We have experimentally validated our framework through extensive experiments (total of 40) in six different environments (indoor and outdoor). Our experimental results show high tracking accuracy with a mean tracking error of only 38 cm in outdoor areas/closed parking lots, and 55 cm in indoor areas.

Appendices

Appendix A

A.1 Magnitude Auto-correlation

Let $c_I(d)$ and $c_Q(d)$ be the real and imaginary parts of $c(d)$. The auto-correlation function of $c_I(d)$ can be written as

$$A_I(\xi) = E\{c_I(d)c_I(d+\xi)\} = \sum_{n=1}^{N} \frac{\overline{\alpha_n^2}}{2} \cos\left(2\pi \frac{\xi}{\lambda}\psi_n\right) + \frac{1}{2}\sigma_\eta^2 \delta(\xi),$$

where $\psi_n = \cos(\phi_n)$, σ_η^2 is the variance of noise, and $\delta(.)$ is the Dirac delta function. In a similar fashion, the cross-correlation between $c_I(d)$ and $c_Q(d)$ can be written as

$$A_{I,Q}(\xi) = E\{c_I(d)c_Q(d+\xi)\} = \sum_{n=1}^{N} \frac{\overline{\alpha_n^2}}{2} \sin\left(2\pi \frac{\xi}{\lambda}\psi_n\right).$$

Define $\kappa^2(\xi) = \frac{1}{P^2}\left(A_I^2(\xi) + A_{I,Q}^2(\xi)\right)$, where P is the total received power, then [43]

$$\begin{aligned} A_{\text{corr}}(\xi) &= \frac{\pi P}{2}\left(1 + \frac{\kappa^2(\xi)}{4} + \frac{\kappa^4(\xi)}{64} + \dots\right) \approx \frac{\pi P}{2}\left(1 + \frac{\kappa^2(\xi)}{4}\right) \\ &= \frac{\pi}{2}P + \frac{\pi}{8P}\left(A_I(\xi) + jA_{I,Q}(\xi)\right)\left(A_I(\xi) - jA_{I,Q}(\xi)\right) \\ &= C_A + C_{\sigma_\eta}\delta(\xi) \\ &\quad + \frac{\pi}{16P}\sum_{n=1}^{N}\sum_{m>n}\overline{\alpha_n^2\alpha_m^2}cos\left(2\pi\frac{\xi}{\lambda}(\psi_n - \psi_m)\right). \end{aligned}$$

Material Reuse

The material discussed in the chapters of this dissertation has been published in the following publications:

- Chitra R. Karanam and Yasamin Mostofi. 2017. 3D through-wall imaging with unmanned aerial vehicles using wifi. In Proceedings of the 16th ACM/IEEE International Conference on Information Processing in Sensor Networks (IPSN '17). Association for Computing Machinery, New York, NY, USA, 131–142. [82] DOI: https://doi.org/10.1145/3055031.3055084

- ©IEEE. Reprinted, with permission, from Chitra R. Karanam, Belal Korany, and Yasamin Mostofi. 2018. Magnitude-based angle-of-arrival estimation, localization, and target tracking. In Proceedings of the 17th ACM/IEEE International Conference on Information Processing in Sensor Networks (IPSN '18). IEEE Press, 254–265. [70] DOI: https://doi.org/10.1109/IPSN.2018.00053

- Chitra R. Karanam, Belal Korany, and Yasamin Mostofi. 2019. Tracking from one side: multi-person passive tracking with WiFi magnitude measurements. In Proceedings of the 18th International Conference on Information Processing in Sensor Networks (IPSN '19). Association for Computing Machinery, New York, NY, USA, 181–192. [83] DOI: https://doi.org/10.1145/3302506.3310399

Bibliography

[1] Y. Mostofi, *Cooperative Wireless-Based Obstacle/Object Mapping and See-Through Capabilities in Robotic Networks*, *IEEE Transactions on Mobile Computing* **12** (2013), no. 5 817–829.

[2] M. Dehmollaian and K. Sarabandi, *Refocusing through building walls using synthetic aperture radar*, *IEEE Transactions on Geoscience and Remote Sensing* **46** (2008), no. 6 1589–1599.

[3] S. Depatla, L. Buckland, and Y. Mostofi, *X-ray vision with only WiFi power measurements using rytov wave models*, *IEEE Trans. on Vehicular Technology* **64** (2015), no. 4 1376–1387.

[4] J. Wilson and N. Patwari, *Radio tomographic imaging with wireless networks*, *IEEE Transactions on Mobile Computing* **9** (2010), no. 5 621–632.

[5] Y. Mostofi, *Compressive Cooperative Sensing and Mapping in Mobile Networks*, *IEEE Transactions on Mobile Computing* **10** (December, 2011) 1770–1785.

[6] W. Chew and Y. Wang, *Reconstruction of two-dimensional permittivity distribution using the distorted born iterative method*, *IEEE Transactions on Medical Imaging* **9** (1990), no. 2 218–225.

[7] A. Devaney, *Inversion formula for inverse scattering within the born approximation*, *Optics Letters* **7** (1982), no. 3 111–112.

[8] Q. Liu, Z. Zhang, T. Wang, J. Bryan, G. Ybarra, L. Nolte, and W. Joines, *Active microwave imaging. i. 2-D forward and inverse scattering methods*, *IEEE Transactions on Microwave Theory and Techniques* **50** (2002), no. 1 123–133.

[9] F. Ahmad, Y. Zhang, and M. Amin, *Three-dimensional wideband beamforming for imaging through a single wall*, *IEEE Geoscience and Remote Sensing Letters* **5** (2008), no. 2 176–179.

[10] A. Beeri and R. Daisy, *High-resolution through-wall imaging*, in *Defense and Security Symposium*, pp. 62010J–62010J, International Society for Optics and Photonics, 2006.

[11] Y. Wang and A. Fathy, *Three-dimensional through wall imaging using an UWB SAR*, in *2010 IEEE Antennas and Propagation Society International Symposium*, pp. 1–4, IEEE, 2010.

[12] F. Adib, C. Hsu, H. Mao, D. Katabi, and F. Durand, *Capturing the human figure through a wall*, *ACM Transactions on Graphics* **34** (2015), no. 6 219.

[13] W. Zhang, A. Hoorfar, and L. Li, *Through-the-wall target localization with time reversal music method*, *Progress In Electromagnetics Research* **106** (2010) 75–89.

[14] Y. Mostofi and P. Sen, *Compressive Cooperative Mapping in Mobile Networks*, in *Proceedings of the 28th American Control Conference (ACC)*, (St. Louis, MO), pp. 3397–3404, June, 2009.

[15] Y. Mostofi and A. Gonzalez-Ruiz, *Compressive cooperative obstacle mapping in mobile networks*, (San Jose, CA), pp. 947–953, nov., 2010.

[16] K. Held, E. Kops, B. Krause, W. Wells, R. Kikinis, and H. Muller-Gartner, *Markov random field segmentation of brain MR images*, *IEEE Transactions on Medical Imaging* **16** (1997), no. 6 878–886.

[17] Y. Rachlin, J. Dolan, and P. Khosla, *Efficient mapping through exploitation of spatial dependencies*, in *Intelligent Robots and Systems, 2005.(IROS 2005). 2005 IEEE/RSJ International Conference on*, pp. 3117–3122, IEEE, 2005.

[18] P. Felzenszwalb and D. Huttenlocher, *Efficient belief propagation for early vision*, *International journal of computer vision* **70** (2006), no. 1 41–54.

[19] P. Kohli and P. Torr, *Efficiently solving dynamic markov random fields using graph cuts*, in *Tenth IEEE International Conference on Computer Vision*, vol. 2, pp. 922–929, IEEE, 2005.

[20] B. D. Van Veen and K. M. Buckley, *Beamforming: A versatile approach to spatial filtering*, *IEEE Acoustics, Speach, and Signal Processing (ASSP) magazine* **5** (1988), no. 2 4–24.

[21] R. Schmidt, *Multiple emitter location and signal parameter estimation*, *IEEE Transactions on Antennas & Propagation* **34** (1986) 276–280.

[22] R. Roy and T. Kailath, *Esprit-estimation of signal parameters via rotational invariance techniques*, *IEEE Transactions on Acoustics, Speech, and Signal Processing* **37** (1989), no. 7 984–995.

[23] Y. Zhuo, H. Zhu, and H. Xue, *Identifying a new non-linear csi phase measurement error with commodity wifi devices*, in *IEEE 22nd International Conf. on Parallel and Distributed Systems (ICPADS)*, 2016.

[24] J. P. Lie, T. Blu, and C. M. S. See, *Single antenna power measurements based direction finding*, *IEEE Trans. on Signal Processing* **58** (2010), no. 11 5682–5692.

[25] R. Pöhlmann, S. Zhang, T. Jost, and A. Dammann, *Power-based direction-of-arrival estimation using a single multi-mode antenna*, *arXiv preprint arXiv:1706.09690* (2017).

[26] H. Kim, A. M. Haimovich, and Y. C. Eldar, *Non-coherent direction of arrival estimation from magnitude-only measurements*, *IEEE Signal Processing Letters* **22** (2015), no. 7 925–929.

[27] X. Shen, R. Fan, Q. Wan, and W. Yang, *An angle difference of directions arrival algorithm with channel inconsistency*, *International J. of Electronics* **100** (2013), no. 3 312–318.

[28] M. Malmirchegini and Y. Mostofi, *On the spatial predictability of communication channels*, *IEEE Transactions on Wireless Communications* **11** (2012), no. 3 964–978.

[29] A. Khafaji, R. Saadane, J. El Abbadi, and M. Belkasmi, *Ray tracing technique based 60 ghz band propagation modelling and influence of people shadowing*, *International Journal of Electrical, Computer, and Systems Engineering* **2** (2008), no. 2 102–108.

[30] T. Wei, A. Zhou, and X. Zhang, *Facilitating robust 60 ghz network deployment by sensing ambient reflectors*, in *14th {USENIX} Symposium on Networked Systems Design and Implementation ({NSDI} 17)*, pp. 213–226, 2017.

[31] A. Zhou, S. Xu, S. Wang, J. Huang, S. Yang, T. Wei, X. Zhang, and H. Ma, *Robotic millimeter-wave wireless networks*, *IEEE/ACM Transactions on Networking* (2020).

[32] E. F. Knott, J. F. Schaeffer, and M. T. Tulley, *Radar cross section*. SciTech Publishing, 2004.

[33] S. Shi, S. Sigg, L. Chen, and Y. Ji, *Accurate location tracking from csi-based passive device-free probabilistic fingerprinting*, *IEEE Trans. on Vehicular Technology* (2018).

[34] J. Zhang, W. Xiao, S. Zhang, and S. Huang, *Device-free localization via an extreme learning machine with parameterized geometrical feature extraction*, *Sensors Journal* **17** (2017), no. 4 879.

[35] K. Wu, J. Xiao, Y. Yi, D. Chen, X. Luo, and L. M. Ni, *Csi-based indoor localization*, *IEEE Trans. on Parallel and Distributed Systems* **24** (2013), no. 7 1300–1309.

[36] M. Bocca, O. Kaltiokallio, N. Patwari, and S. Venkatasubramanian, *Multiple target tracking with rf sensor networks*, *IEEE Transactions on Mobile Computing* **13** (2014), no. 8 1787–1800.

[37] S. Chang, R. Sharan, M. Wolf, N. Mitsumoto, and J. W. Burdick, *Uwb radar-based human target tracking*, in *IEEE Radar Conference*, pp. 1–6, IEEE, 2009.

[38] F. Adib, Z. Kabelac, and D. Katabi, *Multi-person localization via rf body reflections.*, in *USENIX NSDI*, pp. 279–292, 2015.

[39] X. Li, D. Zhang, Q. Lv, J. Xiong, S. Li, Y. Zhang, and H. Mei, *Indotrack: Device-free indoor human tracking with commodity Wi-Fi*, *Proceedings of the ACM on Interactive, Mobile, Wearable and Ubiquitous Technologies* **1** (2017), no. 3 72.

[40] X. Li, S. Li, D. Zhang, J. Xiong, Y. Wang, and H. Mei, *Dynamic-music: accurate device-free indoor localization*, in *Proceedings of the ACM International Joint Conference on Pervasive and Ubiquitous Computing*, pp. 196–207, ACM, 2016.

[41] J. Gjengset, J. Xiong, G. McPhillips, and K. Jamieson, *Phaser: Enabling phased array signal processing on commodity wifi access points*, in *Proceedings of the 20th annual International Conference on Mobile Computing and Networking*, pp. 153–164, ACM, 2014.

[42] W. Chew, *Waves and fields in inhomogeneous media*, vol. 522. IEEE press New York, 1995.

[43] W. Jakes and D. Cox, *Microwave mobile communications*. Wiley-IEEE Press, 1994.

[44] Y. Mostofi, A. Gonzalez-Ruiz, A. Gaffarkhah, and D. Li, *Characterization and modeling of wireless channels for networked robotic and control systems-a comprehensive overview*, in *2009 IEEE/RSJ International Conference on Intelligent Robots and Systems*, IEEE, 2009.

[45] R. Chandra, A. Gaikwad, D. Singh, and M. Nigam, *An approach to remove the clutter and detect the target for ultra-wideband through-wall imaging*, *Journal of Geophysics and Engineering* **5** (2008), no. 4 412.

[46] E. Candès, J. Romberg, and T. Tao, *Robust uncertainty principles: Exact signal reconstruction from highly incomplete frequency information*, *IEEE Transactions on information theory* **52** (2006), no. 2 489–509.

[47] D. Donoho, *Compressed sensing*, *IEEE Transactions on information theory* **52** (2006), no. 4 1289–1306.

[48] C. Feng, W. S. A. Au, S. Valaee, and Z. Tan, *Received-signal-strength-based indoor positioning using compressive sensing*, *IEEE Transactions on Mobile Computing* **11** (2012), no. 12 1983–1993.

[49] Q. Huang, L. Qu, B. Wu, and G. Fang, *UWB through-wall imaging based on compressive sensing*, *IEEE Transactions on Geoscience and Remote Sensing* **48** (2010), no. 3 1408–1415.

[50] T. Jensen, J. Jørgensen, P. Hansen, and S. Jensen, *Implementation of an optimal first-order method for strongly convex total variation regularization*, *BIT Numerical Mathematics* **52** (2012), no. 2 329–356.

[51] A. Blake, P. Kohli, and C. Rother, *Markov random fields for vision and image processing*. Mit Press, 2011.

[52] J. Besag, *Spatial interaction and the statistical analysis of lattice systems*, *Journal of the Royal Statistical Society. Series B (Methodological)* (1974) 192–236.

[53] D. Koller and N. Friedman, *Probabilistic graphical models: principles and techniques*. MIT press, 2009.

[54] Y. Weiss, *Belief propagation and revision in networks with loops*, .

[55] S. Shimony, *Finding MAPs for belief networks is np-hard*, *Artificial Intelligence* **68** (1994), no. 2 399–410.

[56] Z. Yin and R. Collins, *Belief propagation in a 3D spatio-temporal MRF for moving object detection*, in *2007 IEEE Conference on Computer Vision and Pattern Recognition*, pp. 1–8, IEEE, 2007.

[57] J. Yedidia, W. Freeman, Y. Weiss, *et. al.*, *Generalized belief propagation*, in *NIPS*, vol. 13, pp. 689–695, 2000.

[58] A. Gonzalez-Ruiz and Y. Mostofi, *Cooperative robotic structure mapping using wireless measurements - a comparison of random and coordinated sampling patterns*, *IEEE Sensors Journal* **13** (2013), no. 7 2571–2580.

[59] 3DR, *3d robotics*, 2015. Online.

[60] Google, *Google project tango*, 2015. Online.

[61] G. Loianno, G. Cross, C. Qu, Y. Mulgaonkar, J. Hesch, and V. Kumar, *Flying smartphones: Automated flight enabled by consumer electronics*, *IEEE Robotics & Automation Magazine* **22** (2015), no. 2 24–32.

[62] O. Inc., *Rostango repository*, 2015. Online.

[63] Google, *Tango android application repo*, 2015. Online.

[64] P. Lemke, S. Skiena, and W. Smith, *Reconstructing sets from interpoint distances*, in *Discrete and Computational Geometry*, pp. 597–631. Springer, 2003.

[65] T. Ping, W. Pian, L. Ye, Y. ZHANG, and M. Hong, *Study of 2d doa estimation for uniform circular array in wireless location system*, *International Journal of Computer Network and Information Security* **2** (2010), no. 2 54.

[66] D. Halperin, W. Hu, A. Sheth, and D. Wetherall, *Tool release: Gathering 802.11n traces with channel state information*, *ACM SIGCOMM CCR* **41** (Jan., 2011) 53.

[67] M. R. Inc., *Pioneer 3-at*, 2010.

[68] U. N210, *Ettus research*, 2015.

[69] A. Goldsmith, *Wireless communications*. Cambridge university press, 2005.

[70] C. R. Karanam, B. Korany, and Y. Mostofi, *Magnitude-based angle-of-arrival estimation, localization, and target tracking*, in *Proceedings of the 17th ACM/IEEE International Conference on Information Processing in Sensor Networks*, pp. 254–265, 2018.

[71] M. C. Vanderveen, A. J. Van der Veen, and A. Paulraj, *Estimation of multipath parameters in wireless communications*, *IEEE Transactions on Signal Processing* **46** (1998), no. 3 682–690.

[72] Q. Chen and R. Liu, *On the explanation of spatial smoothing in music algorithm for coherent sources*, in *International Conference on Information Science and Technology*, pp. 699–702, 2011.

[73] A. Bazzi, D. Slock, and L. Meilhac, *On spatio-frequential smoothing for joint angles and times of arrival estimation of multipaths*, in *IEEE International Conference on Acoustics, Speech and Signal Processing (ICASSP)*, pp. 3311–3315, IEEE, 2016.

[74] T. B. Schön, *Nonlinear system identification using particle filters*, *Encyclopedia of Systems and Control* (2015) 882–890.

[75] D. Schulz, W. Burgard, D. Fox, and A. B. Cremers, *People tracking with mobile robots using sample-based joint probabilistic data association filters*, *The International Journal of Robotics Research* **22** (2003), no. 2 99–116.

[76] Github, *linux-80211n-csitool-supplementary*, 2015.

[77] W. Wang, A. X. Liu, M. Shahzad, K. Ling, and S. Lu, *Understanding and modeling of wifi signal based human activity recognition*, in *Proceedings of the International Conference on Mobile Computing and Networking*, pp. 65–76, ACM, 2015.

[78] T. Z. Chowdhury, *Using Wi-Fi channel state information (CSI) for human activity recognition and fall detection*. PhD thesis, University of British Columbia, 2018.

[79] K. Qian, C. Wu, Y. Zhang, G. Zhang, Z. Yang, and Y. Liu, *Widar2.0: Passive human tracking with a single wi-fi link*, *Proceedings of ACM MobiSys* (2018).

[80] S. Nannuru, Y. Li, Y. Zeng, M. Coates, and B. Yang, *Radio-frequency tomography for passive indoor multitarget tracking*, *IEEE Transactions on Mobile Computing* **12** (2013), no. 12 2322–2333.

[81] C. Xu, B. Firner, R. S. Moore, Y. Zhang, W. Trappe, R. Howard, F. Zhang, and N. An, *Scpl: indoor device-free multi-subject counting and localization using radio signal strength*, in *Proceedings of the 12th international conference on Information processing in sensor networks*, pp. 79–90, ACM, 2013.

[82] C. R. Karanam and Y. Mostofi, *3d through-wall imaging with unmanned aerial vehicles using wifi*, in *Proceedings of the 16th ACM/IEEE International Conference on Information Processing in Sensor Networks (IPSN)*, pp. 131–142, ACM, 2017.

[83] C. R. Karanam, B. Korany, and Y. Mostofi, *Tracking from one side: multi-person passive tracking with wifi magnitude measurements*, in *Proceedings of the 18th International Conference on Information Processing in Sensor Networks*, pp. 181–192, 2019.